EPIGENETIC REPROGRAMMING OF MYELOID-DERIVED SUPPRESSOR CELLS SENSITIZES BREAST AND PANCREATIC CANCERS TO IMMUNE CHECKPOINT INHIBITION

By
Brian J. Christmas

A dissertation submitted to Johns Hopkins University in conformity with the requirements for the degree of Doctor of Philosophy

Baltimore, Maryland
March 2019

A B S T R A C T

Immune checkpoint inhibition (ICI) has revolutionized treatment in cancers that are naturally immunogenic by enabling infiltration of T cells into the tumor microenvironment (TME) and promoting cytotoxic signaling pathways. Tumors possessing complex immunosuppressive TME's such as breast and pancreatic cancers present unique therapeutic obstacles as response rates to ICI remain low. Such tumors often recruit myeloid-derived suppressor cells (MDSCs) whose functioning prohibits both T-cell activation and infiltration.

We show that combining the histone deacetylase inhibitor entinostat (ENT) with the ICIs, anti-PD-1 and anti-CTLA-4, significantly improve survival in murine models of breast and pancreatic cancer. We show this improved survival is correlated with decreased granulocytic-MDSC (G-MDSC) immunosuppressive capabilities of intratumoral G-MDSCs in both models via flow cytometry and *ex vivo* functional assays. Additionally, we show that combination therapy increases the infiltration of activated cytotoxic T cells in the TME in both models. We also perform genetic profiling on both isolated intratumoral G-MDSCs as well as whole TIL and found significant changes in immune-related pathways. Specifically, intratumoral G-MDSCs from treated animals showed changes in various signaling pathways that converge at STAT3, a known transcription factor that drives MDSC function. We confirmed a decrease in STAT3 phosphorylation in treated G-MDSCs, which suggested ENT may be reprogramming MDSC function via STAT3. We next validated the MDSC-like cell line J774M for future mechanistic studies aimed to detail changes in STAT3 binding activity. We found J774M cells phenotypically and functionally resemble intratumoral MDSCs via flow cytometry in addition to arginase production and T cell proliferation assays. We also show ENT

inhibits these immunosuppressive qualities of the J774M line, which is correlated with a decrease in STAT3 phosphorylation. Taken together, these data show that ENT is able to sensitize non-immunogenic breast and pancreatic cancers to ICI therapy by reprogramming intratumoral MDSCs potentially via changes in STAT3 activity. Additionally, the validation of the J774M line demonstrates it is a reasonable model for MDSC suppression and ENT-induced MDSC dysfunction.

Thesis Advisor:

Dr. Elizabeth M. Jaffee, M.D. (Designated Reader)

Thesis Committee:

Dr. Alan D. Friedman, M.D.

Dr. Lei Zheng, M.D.

Dr. Nilofer A. Azad, M.D. (Designated Reader)

A C K N O W L E D G E M E N T S

I would like to express my deepest thanks to my mentor, Liz. She was patient when I was learning, thoughtful when she was teaching, and proud when we succeeded. Without her, this project and moment would have been impossible. I would also like to thank Dr. Alan Friedman, Dr. Lei Zheng, and Dr. Nilo Azad for their guidance throughout my thesis work. Evanthia and Christine, this project would have never succeeded without your hard work and brilliant ideas. Thank you for being my lab family.

Without my parents, graduate school would have never been in my future. From an early age they instilled the importance of education and a love of learning that has never faded. Along with the desire learn, my parents also imparted a sense of humor essential for a career where the only way to succeed is to fail *ad nauseam.* Mom and Dad, thank you for your unconditional love and support.

To my friends: You are my chosen family. Helen, you remade in your terrifying image, and I cannot thank you enough. Blake, I never would have made it through the worst times of graduate school without your undying friendship. Laura, I will always be your Midwestern housewife. Nina, thank you for sharing your scientific brilliance as well as your ill-fated misadventures. Drunk Nina, you are a nightmare. Because of all you, I will remember a time of failed experiments and self-doubt as a fond haze of bar trivia, cheap liquor, and drag queens.

Mike, your love and companionship mean the world to me. You constantly push me to experience new things, travel to new places, and explore new facets of myself. Words cannot describe how grateful I am to have someone so kind, funny, and thoughtful in my life. Whether it be by listening to presentations, illustrating figures for manuscripts,

or pouring wine while I curse the entire mouse species, none of my successes would have been possible without your love and support. As this chapter of my life closes, I may not know what the future holds; however, I do know that it will be *fabulous* with you by my side. Thank you for being my best friend and father to my cat.

T A B L E O F C O N T E N T S

L I S T O F T A B L E S

CHAPTER ONE: Entinostat sensitizes tumors to checkpoint inhibition by reprogramming MDSCs

L I S T O F F I G U R E S

CHAPTER ONE: Entinostat sensitizes tumors to checkpoint inhibition by reprogramming MDSCs

CHAPTER TWO: Validating the J774M cell line to determine the role of STAT3 in entinostat-induced MDSC reprogramming

INTRODUCTION

ICIs induce immune responses to tumors by releasing the brakes on effector T cells that naturally infiltrate the TME. As a result, non-immunogenic cancers with low intrinsic T cell infiltration, such as breast and pancreas cancers, often have low response rates to ICI therapy (1–9). The natural resistance of breast and pancreatic tumors to single agent ICI therapy is in part due to a lack of infiltrating T cells as well as to expression of various immunosuppressive signals on suppressive immune cells and the tumor that limit T cell infiltration and activation by these therapies. The monocyte component of both breast and pancreatic TMEs play a major role in the suppression of tumor-specific responses, as these tumors are often infiltrated by several immunosuppressive monocytic cell types, including M2-like TAMs and MDSCs (10), and these in turn inhibit infiltration and activity of $CD8^+$ T cells with the potential to kill tumors (11–13).

Two subtypes of MDSCs, granulocytic (G-MDSCs) and monocytic-MDSCs (M-MDSCs), collectively inhibit T cell functionality by depleting L-arginine through arginase-1 (Arg-1) expression, and by inducing nitric oxide synthase (iNOS) expression, PD-L1 expression, TGF-β production, and regulatory T cells (T_{regs}) (14–20). While typically less abundant in the TME, M-MDSCs are considered to be significantly more immunosuppressive than G-MDSCs (21). As with many myeloid sub-types, M-MDSCs are a fluid population that can quickly differentiate into immunosuppressive TAMs within the TME (22). Despite being less immunosuppressive than M-MDSCs, G-MDSCs are the predominant MDSC subtype in most tumors and primarily inhibit T cell function by producing both reactive oxidative species and NO, which results in the down-regulation of T cell receptors (TCRs) on the surface of effector T cells and subsequent inhibition of TCR signaling (21,23). STAT3 acts as a major driver of many of these

immunosuppressive functions of MDSCs in addition to inducing MDSC proliferation (21,24). Studies highlighting the importance of STAT3 in MDSC biology have that STAT3 activity is essential for MDSC induction (25,26) and ablation of STAT3 activity renders MDSCs dysfunctional (27,28). High numbers of tumor infiltrating myeloid cells have been correlated with early or local metastatic relapse (29). Previous studies have also shown changes in both circulating and tumor infiltrating G-MDSCs in response to ICIs as a potential mechanism inhibiting anti-tumor responses (21,29,30). Thus, strategic reprogramming of these myeloid responses may overcome the immunosuppressive microenvironment and lead to enhanced response to immune therapy through improved T cell infiltration and function.

Recent studies using epigenetic modulatory drugs have shown promise in decreasing the infiltration and inhibitory capabilities of immunosuppressive cells. The histone deacteylase inhibitor (HDACi) entinostat (ENT) has been shown to decrease the number of inhibitory T_{regs} within the TME when combined with IL-2 therapy or a survivin-based vaccine. This reduction in T_{regs} correlated with reduced tumor burden (31). HDACi's were also shown to ablate the immunosuppressive ability of MDSCs when combined with ICIs in *in vivo* models of lung and renal cell cancer (30). As further evidence, Kim and colleagues also showed similar results in highly aggressive triple negative breast and colon cancer models, where co-treatment with ENT and ICIs resulted in eradication of metastases and decreased MDSCs in circulation and within tumors (29). Finally, Tomita et al. reported decreased circulating G-MDSCs and M-MDSCs in clinical samples of breast cancer patients treated with ENT alone (32). Taken together, these data suggest that ENT can alter suppressive myeloid populations in multiple tumor types and collaborate with immunotherapies to slow tumor growth and progression.

Our work explored the impact of HDACi's on the $HER2^+$ breast and PDAC TME in immunocompetent murine models. Combination therapy of ENT with anti-PD-1 or anti-CTLA-4 significantly improves survival as compared to either agent alone or combined ICIs. To our surprise, the class I HDACi ENT increased infiltration of G-MDSCs into the tumor but interestingly, changed the polarity of their immunosuppressive ability to a non-functional phenotype. Flow cytometry and gene expression profiling of treated tumors demonstrated changes in expression of functional molecules and pathways involved in proliferation and motility. These observations suggest ENT decreased the immunosuppressive nature of infiltrating MDSCs and allowed for ICIs to increase the infiltration and cytotoxicity of T cells by altering STAT3 activity in MDSCs. We pursued this hypothesis in the MDSC-like cell line J774M and showed J774M cells treated with ENT were unable to produce Arg-1 and suppress T cell proliferation, which correlated with a decrease in STAT3 phosphorylation. Taken together, these data further support that ENT reprograms MDSCs by altering STAT3 activity.

CHAPTER ONE: Entinostat sensitizes tumors to checkpoint inhibition by reprogramming MDSCs

Summary

Efficacy of ICI therapy is often ineffective in-immunogenic tumors, such as breast and pancreatic cancers. We attempted to sensitize non-immunogenic breast and pancreatic tumors to ICI using epigenetic modulation to target MDSC trafficking and function in order to foster a less immunosuppressive TME. We showed that combining a histone deacetylase inhibitor, ENT, with anti–PD-1, anti–CTLA-4, or both, significantly improved tumor-free survival in both the HER2/neu transgenic breast cancer and the Panc02 metastatic pancreatic cancer mouse models. Using flow cytometry, gene expression profiling, and *ex vivo* functional assays, we characterized populations of tumor-infiltrating lymphocytes (TILs) and MDSCs, as well as their functional capabilities. We showed that addition of ENT to checkpoint inhibition led to significantly decreased suppression by granulocytic-MDSCs in the TME of both tumor types. We also demonstrated an increase in activated granzyme-B–producing $CD8^+$ T effector cells in mice treated with combination therapy. Gene expression profiling of both MDSCs and TILs identified significant changes in immune-related pathways. In summary, addition of ENT to ICI significantly altered infiltration and function of innate immune cells, allowing for a more robust adaptive immune response. These findings provide a rationale for combination therapy in patients with immune-resistant tumors, including breast and pancreatic cancers.

Introduction

Immunotherapy has changed the standard of care for some patients with advanced cancers and has great promise to prevent recurrence and prolong survival due to the long-term memory capabilities of the adaptive immune system. Although the presence of tumor-infiltrating lymphocytes (TILs) and evidence of immune activation have been associated with improved outcomes in $HER2^+$ and triple-negative breast cancers (TNBC) (33,34), only modest response rates have been observed with use of single-agent immune checkpoint inhibitors (ICIs) (1–7,35). Preclinical studies have focused on understanding these therapies in TNBC models (29) but have yet to thoroughly examine other subtypes of breast cancer. It has also been previously reported that antibodies blocking programmed cell death protein-1 (anti–PD-1) can significantly improve the activity of anti-HER2 therapies, but we have yet to understand if there is any added benefit of other ICIs (36). Similarly, single-agent ICIs have been shown to be ineffective in the clinical setting in metastatic pancreatic ductal adenocarcinomas (PDAC) (8,9). However, efficacy has been seen using combinatorial approaches in preclinical models. It has been shown that priming the tumor with a vaccine sensitizes PDAC to anti–PD-1 therapy by inducing the infiltration of cytotoxic $CD8^+$ T cells (15). In PDAC patients, a similar vaccine was reported to induce TILs (37). Improved efficacy of both anti–PD-1 and anti–CTLA-4 was achieved in murine models of PDAC by reprogramming immunosuppressive tumor-associated macrophages (TAMs) (16). Taken together, these studies indicate the possibility to sensitize traditionally non-immunogenic tumors to ICI therapy if TILs can be recruited and induced and/or immunosuppressive factors reduced within the tumor microenvironment (TME).

The natural resistance of breast and pancreatic tumors to single-agent ICI therapy is due to a lack of infiltrating T cells and an abundance of suppressive immune cells such as MDSCs. Specifically, granulocytic (G-MDSCs) and monocytic MDSCs (M-MDSCs) collectively inhibit T-cell function by depleting L-arginine through arginase-1 (Arg-1) expression and by inducing PD-L1 expression and the recruitment of regulatory T cells (T_{regs}) (14,15,19,20). High numbers of tumor-infiltrating myeloid cells correlates with early or local metastatic relapse (29). Previous studies have also shown changes in both circulating and tumor-infiltrating G-MDSCs in response to ICIs as a potential mechanism inhibiting antitumor responses (21,29,30). Thus, targeting and strategic reprogramming of these myeloid responses may overcome the immunosuppressive microenvironment and lead to an enhanced response to immune therapy through improved T-cell infiltration and function.

Studies using epigenetic modulatory drugs have shown promise in decreasing the infiltration and inhibitory capabilities of immunosuppressive cells. ENT ablates MDSC-mediated immunosuppressive activity when combined with ICIs in *in vivo* models of lung and renal cell cancer (30). Tomita et al. reported decreased circulating G-MDSCs and M-MDSCs in clinical samples of breast cancer patients treated with ENT in combination with an aromatase inhibitor compared to placebo combined with aromatase inhibitor (32). Taken together, these data suggest that ENT can alter suppressive myeloid populations in multiple tumor types and synergize with immunotherapies to slow tumor growth and progression.

Our work explored the impact of ENT on the $HER2^+$ breast and PDAC TMEs in immunocompetent mice. Combination therapy of ENT with anti–PD-1 or anti–CTLA-4 significantly improved survival compared to either agent alone or combined ICIs. ENT

increased tumor infiltration by G-MDSCs and changed the polarity of their immunosuppressive ability to a nonfunctional phenotype. Flow cytometry and gene expression profiling of treated tumors demonstrated altered expression of functional molecules and specific genetic pathways involved in proliferation and motility. Our observations suggest that G-MDSCs can exhibit multiple phenotypes and support that a possible mechanism by which ENT allows ICIs to augment the infiltration and cytotoxicity of cancer-killing T cells is through the ablation of the immunosuppressive function of these infiltrating myeloid cells.

Materials and Methods

Mice and cell lines

All animal studies were approved by Institutional Review Board of Johns Hopkins University. Animals were kept in pathogen-free conditions and were treated in accordance with institutional and American Association of Laboratory Animal Committee policies. The neu-N mice were originally from W. Muller McMaster University, Hamilton, Ontario, Canada. Colonies were renewed yearly from Jackson labs and bred in house by brother/sister mating. For studies of metastatic pancreatic cancer, we used male C57BL/6J (The Jackson Laboratories, stock #000664) mice. The T cell receptor (TCR) transgenic mice are specific for the immunodominant HER2/neu epitope $neu_{420-429}$ and were made in house at the JHU Transgenic Core Laboratory as previously described (38). These mice were bred in house by brother/sister mating, and each animal was assessed for expression of the desired neu-specifc Vβ region via staining with the H-$2D^q$ rat HER2/$neu_{420-429}$ PDSLRDLSVF tetramer (NIH Tetramer Core Facility).

All cell lines were regularly tested for Mycoplasma every three months in accordance to laboratory policy. NT2.5 cells were derived from spontaneous mammary tumors growing in female neu-N mice. *In vitro* cell lines were established and authenticated as previously described (39,40). Culture conditions for NT2.5 cells were as follows: 37°C, 5% CO_2 in RPMI 1640 (Gibco, cat. 11875-093) supplemented with 20% fetal bovine serum (Gemini, cat. 100-106), 1.2% HEPES buffer (Gibco, cat. 15630-080), 1% L-glutamine (Gibco, cat. 25030-081), 1% MEM non-essential amino acids (Gibco, cat. 11140-050), 0.5% penicillin streptomycin (Gibco, cat. 15140-122), 1% sodium pyruvate (Sigma, cat. S8636), 0.2% insulin (NovoLog, cat. U-100), 0.02% gentamicin (Sigma, cat. G1397). Panc02 is a murine pancreatic tumor cell line with ductal morphology derived from a

methylcholanthrene-treated C57B1/6 mouse and authenticated as previously described (41,42). Culture conditions for Panc02 cells were as follows: 37°C, 10% CO_2 in DMEM (Gibco, cat. 11965-084) supplemented with 10% fetal bovine serum (Gemini, cat. 100-106), 1% L-glutamine (Gibco, cat. 25030-081), 0.5% penicillin streptomycin (Gibco, cat. 15140-122). The $T2D^q$ cells are a fibroblast cell line established via transfection with murine $H\text{-}2D^q$ as previously described (43). Culture conditions for $T2D^q$ cells are as follows: 37°C, 5% CO_2 in RPMI supplemented with 10% fetal bovine serum (Gibco, cat. 100-106), 1% L-glutamine (Gibco, cat. 25030-081), 1% sodium pyruvate (Gibco, cat. 11965-084), 1% MEM non-essential amino acids (Gibco, cat. 11140-050), 0.5% penicillin streptomycin (Gibco, cat. 15140-122), 0.0007% Hygromycin B (Roche, cat. 10843555001). $T2D^q$ cells were cultured from frozen stocks and passaged three times before use.

Neu-N in vivo studies

The neu-N model is a syngeneic model whereby NT2.5 cells that were derived from a spontaneous mammary tumor are implanted via injection of 5×10^4 cells into the mammary fat pad of 7-8 week old female neu-N mice (39). NT2.5 cells were cultured from frozen stocks and passaged twice before injection. Tumors were allowed to seed for 3 days prior to initiating treatment with various drug combinations as described below. Untreated mice developed palpable tumors within 1 week.

PDAC hemi-splenectomy in vivo studies

To study metastatic PDAC, we used a hemi-splenectomy model using 7-8 week old syngeneic male C57BL/6J. This involved giving an intrasplenic injection of $2x10^6$ of the

pancreatic adenocarcinoma cell line (Panc02), as previously described (44–46). Panc02 cells were cultured from frozen stocks and passaged twice before injection. Metastases were allowed to establish for 7 days prior to starting treatment with various drug combinations as described below.

Rationale for mouse model selection

We selected the Panc02 hemi-splenectomy model in order to recapitulate late stage, metastatic disease, as this is most commonly how patients present. It should be noted that the Panc02 cell line was derived from a chemically induced tumor and contains a high mutational burden. Other groups circumvent this issue by using the genetically engineered KPC PDAC model, which results in pancreatic tumors that are more genetically and pathologically similar human PDAC (45,47,48). While the KPC model more accurately recapitulates primary disease in humans, these animals take a minimum 16 weeks to develop locally invasive PDAC and develop salivary tumors before metastases occur. These tumors grow large and often prohibit maintenance of mice long enough to study natural metastases (45). We recognize the shortcomings of using the Panc02 cell line, which is why we paired the findings in this model with those in an extremely tolerant and non-immunogenic breast cancer model (46). Future work with the KPC model could yield informative data to further translate the outcomes from preclinical models to human disease.

Drug dosing and selection

The ENT dosing solution (5 mg/kg) was made by suspending solid ENT (generously provided by Syndax Pharmaceuticals) in 0.5% methylcellulose via sonication and given

by oral gavage daily for three weeks as described in Fig. 1a. To imitate oral gavage in control groups, 0.5% methylcellulose was given to vehicle mice as well as mice receiving only antibody therapy during the three weeks of ENT dosing. Mice received anti-PD-1 and/or anti-CTLA-4 twice a week for three weeks as stated in Fig. 1a**.** All studies in neu-N model were performed with and without an anti-HER2 antibody to mimic treatment with and without trastuzumab. Anti-HER2 antibody was given once a week for three weeks as described in Fig. 1a. Following initial three weeks of treatment, as described above, maintenance dosing was continued with antibodies every other week. During maintenance therapy, animals receive two doses of anti-PD-1 and/or anti-CTLA-4 as well as one dose of anti-HER2 every other week as shown in Fig. 1a**.** Dosage of antibodies was as follows: anti–PD-1, 100 μg/mouse via intraperitoneal injection (i.p.); anti–CTLA-4, 100 μg/mouse i.p.; anti-HER2, 100 μg/mouse i.p. Monoclonal antibodies were obtained from BioXcell [anti–PD-1 (clone RPM1-14), anti–CTLA-4 (clone 9H-10), and anti-HER2 (clone 7.16.4)] and all were diluted to 0.5 mg/mL in PBS. Isotypes were used to treat vehicle mice and were also obtained from BioXcell [anti–PD-1 isotype: rat IgG2a (clone 2A3); anti–CTLA-4 isotype: polyclonal Syrian Hamster IgG; anti-HER2 isotype: mouse IgG2a (clone C1.18.4)]. All isotype antibodies were also diluted to 0.5 mg/mL in PBS. Dosages of each antibody were based off of prior studies (29). For mice receiving dual checkpoint antibody therapy, anti–CTLA-4 was given alone twice prior to addition of anti–PD-1, given that anti–CTLA-4 has been described as a T-cell repertoire–expanding agent, whereas anti–PD-1 has been determined to expand antigen-experienced T cells and help prevent the exhaustion of activated T cells (49).

For preliminary experiments using the demethylating agent SGI-110 (Astex) and the histone deacetylase inhibitor ACY-1215 (Acetylon), the PDAC hemi-splenectomy

described above was used. Murine GVAX was prepared by irradiating a 1:1 mixture of Panc02 and the GMCSF-secreting bystander line B78H1 as previously described (42,50). A low dose of cyclophosphamide (100 mg/kg) was given four days post-surgery and GVAX was administered five days post-surgery sub-cutaneously into three limbs of the mice. SGI-110 was administered subcutaneously into the flank of the animal at 24.4 mg/kg once a week over the course of three weeks while ACY-1215 was administered i.p. at 50 mg/kg daily. Following dosing of ACY-1215 and GVAX, survival was monitored until 120 days post-surgery.

Rationale for use of entinostat

It has previously been shown that inhibition of class I HDACs targeted by ENT improves TLR signaling and cytokine production in myeloid cells (51) as well as cytokine signaling in T cells (52). Therefore, we hypothesized that use of ENT acted on these cell types to help sensitive non-immunogenic tumors to ICIs. While we showed that ENT did indeed improve efficacy of ICIs in the neu-N and PDAC models, the mechanism appeared to be largely dependent on inhibiting the ability of MDSCs to produce immunosuppressive factors, specifically arginase-1. Although a specific class I HDAC has not been identified as a regulator of Arg-1, a few studies illustrate a potential mechanism for the regulation of *Arg1* transcription involving HDAC2. It has previously been shown that a complex of Tet2 and HDAC2 is required for regulating the transcription of various inflammatory genes in macrophages, such as *Il6* and *Tnfα*, and this regulation can be abrogated with HDAC2 siRNA as well as entinostat *in vitro* (53). Additionally, Pan et al. showed that myeloid-specific knockout of Tet2 resulted in decreased Arg-1 expression in TAMs as well as decreased ability to suppress T cell

proliferation (54). Taken together, these studies suggest Arg-1 could be regulated in a similar way as IL-6, where Tet2 recruits HDAC2 to the arginase-1 promoter to regulate gene transcription.

Rationale for addition of ICIs to ENT was also provided by two promising ongoing clinical trials that combine nivolumab, ipilumumab and ENT (NCT02453620, NCT03250273). However, mechanisms of action of these drug combinations remain elusive and thus, these preclinical studies were designed to inform rational design of clinical correlates for these trials and elucidate mechanisms behind potential anti-tumor responses.

Survival and tumor growth assays

Following injection of either Panc02 or NT2.5 cells, mice were treated for three weeks as depicted in Fig. 1a, and then received maintenance therapy until succumbing to disease or requiring sacrifice due to tumor burden (up to 2 cm^3). In the neu-N model, mice were examined for palpable tumors starting one-week post tumor cell challenge, and subsequently measured by calipers (± 0.01 mm) twice weekly. Survival experiments were continued until mice were euthanized according to protocol due to tumor burden (neu-N model) or the development of ascites (PDAC model).

Tumor dissociation

To obtain single-cell suspensions from breast tumors, tumors were harvested, weighed, diced, and then dissociated using a tumor dissociation kit (Miltenyi Biotec, cat. 130-096-730) and the OctoDissociator (Miltenyi Biotec) per the manufacturer's instructions. The 37C_m_TDK_2 program was used to dissociate tumors per the

manufacturer's instructions. Samples were filtered using a 40 μm cell strainer and red blood cells were lysed using ACK lysis buffer (Quality Biological, cat. 118-156-721). The resulting single-cell suspensions were used for subsequent isolation of specific immune cell types or flow cytometry as described below. Blood from neu-N mice was obtained via retro-orbital bleeds as per protocol. Red blood cells were lysed using ACK lysis buffer (Quality Biological, cat. 118-156-721). Isolated cells were analyzed via flow cytometry. To obtain single-cell suspensions of livers containing metastases in the PDAC model, livers were harvested and processed by mashing the liver through 100 μm and 40 μm cell strainers as previously described (50). Red blood cells were lysed using ACK lysis buffer (Quality Biological, cat. 118-156-721) and liver pellets were resuspended in 40% Percoll (GE Healthcare Life Sciences, cat. 17-0891-01) and underlayed with 80% Percoll. The immune cell layer was then removed and analyzed via flow cytometry.

Immune cell isolation

G-MDSCs were isolated from single-cell suspensions from tumors following tumor dissociation using Miltenyi Biotec's Myeloid-Derived Suppressor Cell Isolation Kit (cat. 130-094-538) according to the manufacturer's protocol. $Ly6G^+$ cells were positively selected to isolate G-MDSCs from $Ly6G^-$ M-MDSCs and were passed through LS columns (Miltenyi Biotec, cat. 130-042-401) twice to increase purity. Eluted G-MDSCs were then used for downstream assays described below. $CD8^+$ neu-specific T cells were negatively isolated from spleens of the TCR transgenic mice described above by mashing spleens through 100 μm cell strainers. Red blood cells were lysed using ACK lysis buffer (Quality Biological, cat. 118-156-721), and $CD8^+$ T cells were isolated from spleen pellets using the EasySep Mouse $CD8^+$ Isolation Kit (StemCell, cat. 19853) per the

manufacturer's instructions. $CD8^+$ T cells were then used for the *ex vivo* suppression assay described below.

Flow cytometry

Isolated single-cell suspensions were washed and then incubated for 30 minutes with Live/Dead Near-IR (ThermoFisher, cat. L10119) according to the manufacturer's protocol, followed by a 30-minute incubation with the appropriate flow cytometry antibodies (Supplementary Table 1). For samples being analyzed for cytokine expression, single-cell suspensions obtained from tumor dissociations were plated at 37°C with anti-CD3/CD28 beads (ThermoFisher, cat. 11453D) overnight at a bead-to-cell ratio of 1:1 per the manufacturer's instructions for T cell activation. A protein transport inhibitor cocktail (eBioscience, cat. 00-4980-03) was introduced at 1x concentration during the last 4-6 hours of stimulation. The samples were harvested after 16 hours. For samples being stained for intracellular markers, cells were fixed and permeabilized (Transcription Factor Fixation/Permeabilization kit, eBioscience, cat. 00-5523-00) and then incubated with the appropriate antibodies for 30 minutes. Samples were run on a CytoFLEX or Gallios (Beckman Coulter) cytometer and analyzed using FlowJo (FlowJo LLC) or Kaluza (Beckman Coulter).

Flow cytometry gating strategies

G- and M-MDSCs were identified by gating out debris from bulk tumor based on forward scatter and side scatter. Single cells were then gated by forward scatter-area and forward scatter-height. Dead cells were then gated out of the bulk tumor cell population. T cells and mature macrophages were gated out by selecting the CD3 and F4/80 double negative

population, respectively. $CD11b^+$ cells were then gated, and G- and M-MDSCs were differentiated using Ly6G vs. Ly6C. G-MDSCs were defined as $Ly6G^+$ $Ly6C^{lo}$, and M-MDSCs were defined as $Ly6G^-$ $Ly6C^+$. See Supplementary Fig. S1a. Of note, we found that staining with CD45 in combination with more specific markers, such as CD3 and CD11b, did not further exclude non-immune cell types from the final gated populations as compared to single staining with CD3 or CD11b. For example, there were very few cells that were positive for CD3 or CD11b and negative for CD45. Given these findings, we did not use CD45 in our final FACS panels. See Supplementary Fig. S1b. In order to characterize the $CD8^+$ T cells**,** debris was gated out of bulk tumor based on forward scatter and side scatter. Dead cells were then gated out of the bulk tumor population and lymphocytes were subsequently selected as $CD3^+$ and then gated by CD4 vs. CD8. To determine the activation state of $CD8^+$ T cells, $CD8^+$ cells were then gated by CD44 vs. CD62L as well as CD8 vs. granzyme-B. The exhaustion state of $CD8^+$ T cells was determined by gating $CD8^+$ cells by PD-1 vs. Lag3. In order to characterize the $CD4^+$ T cells**,** debris was gated out of bulk tumor based on forward scatter and side scatter. Dead cells were then gated out of the bulk tumor population and lymphocytes were subsequently selected as $CD3^+$ and then selected as $CD4^+$. See Supplementary Fig. S2a.

Ex vivo suppression assay

Isolated G-MDSCs were co-cultured with peptide-specific stimulated T cells and quantified for T-cell proliferation. G-MDSCs were isolated from tumors following tumor dissociation as described above. Eluted G-MDSCs were co-cultured with $1x10^5$ CSFE-labeled $CD8^+$ neu-specific T cells isolated from untreated neu-specific TCR-transgenic mice (38) at varying ratios (1:1 – 1:8 MDSC:T cells). Prior to plating, T-$2D^q$ antigen

presenting cells (APCs) were pulsed with either R-neu$_{420-429}$ or control peptide (NP) 0.4 μg peptide for 4 hours; both purchased from the Johns Hopkins University Synthesis and Sequencing facility at greater than 95% purity. The APCs were simultaneously added to the co-cultured $CD8^+$ T cells and MDSCs at a ratio of 2:1 APCs:T cells, and plates were incubated at 37°C for a total of 48 hours. Cells were then harvested, stained with Live/Dead NIR (ThermoFisher, cat. L10119) as well as CD8 and Thy1.2 and analyzed via flow cytometric analysis as described above. Dilutions of initial CFSE were indications of T cell divisions, where fewer divisions indicated greater suppressive G-MDSC activity. All antibodies used are listed in Supplementary Table 1.

Due to the small number of infiltrating M-MDSCs, we were unable to isolate sufficient numbers of these cells to perform a suppression assay. We attempted using flow cytometry as an alternative method of assessing M-MDSCs. However, the sorted M-MDSCs had poor viability, which had confounding effects on this assay.

Arginase assay

Arginase activity was measured colorimetrically *ex vivo* using Abcam's Arginase Activity Assay Kit (cat. ab180877). G-MDSCs were isolated from tumors and processed as described above and plated per manufacturer's instructions. In short, cells were lysed with kit's lysis buffer at $1x10^6$/1mL, and plated in varying dilutions (30k or 60k cells per well) in duplicate in a flat-bottom, low-retention plate carefully to avoid bubble formation. Target samples were incubated for 20 minutes at 37°C with H_2O_2 substrate solution, while background wells were incubated with additional buffer. Standards were prepared per kit instructions, and the enzymatic reaction mixture was prepared and added to all wells. Raw absorbance values were immediately obtained over a 30-minute period

using a plate reader (Molecular Devices SpectraMax M3) at OD=570nm at 37°C. Arginase Activity Units were then calculated from raw absorbance values. ΔOD (ΔOD= (OD2-ODbg2)-(OD1-ODbg1)) was used to obtain the nmol of H_2O_2 generated by arginase, collected from a standard curve of known H_2O_2 concentrations. Arginase activity is calculated as (B/ΔT*V)*D in units/mL, where B is amount of H_2O_2 from standard curve (nmol), V is the sample volume added into reaction well (μL), D is sample dilution factor. One unit of Arginase activity refers to the amount of arginase that will generate 1.0 nmol of H_2O_2 per minute at pH 8 at 37°C.

Gene expression profiling

RNA was extracted from whole tumors or G-MDSCs isolated from tumors using the Qiagen RNeasy extraction kit (cat. 74104). Using a NanoDrop ND-1000, RNA quality and quantity were determined (samples with A260/280 < 1.8 were excluded). Gene expression was measured on the NanoString nCounter Analysis System (NanoString Technologies). The NanoString PanCancer Immune CodeSet (cat. XT-CSO-MIP1-12) was used to perform the nCounter Gene Expression Assay for whole tumor samples, whereas the Mouse Myeloid Innate Immunity CodeSet (cat. XT-CSO-MII2-12) was used to perform nCounter Gene Expression Assay for isolated G-MDSCs. Quantification of target mRNA in each sample was performed by detection within the nCounter Digital Analyzer. The data obtained from the PanCancer Immune CodeSet were deposited on the public database GEO under the accession number GSE121031. The data obtained from the Mouse Myeloid Innate Immunity CodeSet were deposited on the public database GEO under the accession number GSE121030.

Gene expression analysis

Data from the NanoString nCounter system was normalized to the internal positive controls and housekeeping genes using the recommended settings in the nSolver software normalization module (NanoString Technologies). Normalized data was exported and differential expression analysis was performed using a linear model method with the limma package (55) for the R programming language. To identify pathways which were differentially expressed in each treatment, the gage package (56) was used to test for differentially expressed KEGG pathways. Pathways of interest were visualized using the pathview package (57).

QC plots for NanoString cell typing

The QC plots show the correlation between genes included in the assay that are used to call specific cell types. nSolver uses expression data from *Lag3*, *Cd244*, *Eomes*, and *Ptger4* to call the "Exhausted CD8" set and expression data from *Cd6*, *Cd3d*, *Cd3e*, *Sh2d1a*, *Trat1*, and *Cd3g* to call the "T-cell" set. These plots report how well the expression of the genes within each cell type set correlate with each other. In our data from the PanCancer Immune panel, the algorithm to call cell types uses *Cd3g* and *Cd3d* for "T cells" and *Lag3* for "Exhausted CD8" cells. Due to the inherent variability between animals, more than the recommended 4 biological replicates are likely necessary to prevent the nSolver algorithm from discarding genes used to make cell type calls. See Supplementary Fig. S2b, S2c.

Quantative-PCR

Reverse transcription of mRNA and subsequent qPCR was performed on RNA isolates to validate expression level changes seen in NanoString analysis. RNA extracted from isolated G-MDSCs and whole tumor (Qiagen RNeasy kit, cat. 74104) were normalized to 10 ng/μL, and 1 μg of total RNA was used for reverse transcription. The SuperScript VILO cDNA Synthesis Kit (Invitrogen #11754050) was used following the manufacturer's instructions. qPCR of subsequent cDNA was performed using gene specific proprietary primer and probe constructs for selected genes obtained from TaqMan (ThermoFisher, see individual product numbers per gene), and used with TaqMan Universal Master Mix II, no UNG (Applied Biosystems #4440040) following manufacturer's instructions. qPCR was performed on the StepOnePlus real-time PCR system (Applied Biosystems). To validate the ERBb pathway, *Tgfα* (Mm00446231_m1) and *Egf* (Mm004438696_m1) were checked, for the mTOR pathway, *Tgfα* (Mm00446231_m1) and *Frizzled4* (Mm00433382_m1) were checked, for the VEGF pathway, *Vegfa* (Mm01281449_m1) and *Cox2* (Mm03294838_g1), were checked. For the Leukocyte transendothelial migration pathway, *Pik3cg* (Mm00445038_m1) and *Vcam1* (Mm01320970_m1) were checked, for the osteoclast differentiation pathway, *Infγ (*Mm01168134_m1), and *Il1b* (Mm00434228_m1) were checked. *18s* (Mm04277571_s1) was used as a control and *Stat3* (Mm01219775_m1) and *Arg1* (Mm00475988_m1) were also checked. The 2-step real-time PCR cycling conditions used were 95 °C for 20 s, 40 cycles of 95 °C for 3 s, and then 60 °C for 30 s. Gene expression was quantified from raw data by calculating mean CT values from the three replicates and comparing the ΔCT values of each gene to the 18s reference gene. Fold changes were quantified as 2^ΔΔCT and plotted against corresponding NanoString fold change values.

Western blots

G-MDSCs were isolated from whole tumor of treated animals using Miltenyi Biotec's MDSC Isolation Kit and pooled by treatment group. Samples being used for phospho-STAT3 analysis were subsequently stimulated with IL-6 at 20 ng/µl for 25 minutes. Samples were lysed in RIPA buffer with added 1µM DTT, 1µM PMSF, and 1:100 protease/phosphatase inhibitor cocktail (Cell Signaling #5872S) and quantified by BCA (Pierce, #23225). 125µg of protein was run in 4-12% Bis-Tris gels under denaturing conditions. The LiCor Odyssey developing and imaging system was used, and the following primary antibodies were diluted in Odyssey Blocking Buffer (TBS) + 0.2% Tween® 20 at specified concentrations: Abcam Anti-Interferon gamma rabbit (1:1000), Abcam Anti-VEGFA rabbit (1:1000), Abcam Anti-EGF antibody (1:1000), Cell Signaling TNF-α Rabbit mAb (1:1000), Cell Signaling PI3 Kinase p110γ Rabbit mAb (1:1000), Cell Signaling Stat3 Rabbit mAb (1:2000), Cell Signaling Phospho-Stat3 (Tyr705) Rabbit mAb (1:2000). Membranes were blocked with Odyssey blocking buffer TBS for 1hr and then incubated with primary antibody solution overnight at 4°C with gentle shaking. Membranes were washed with 1X TBS-T and subsequently incubated with the following secondary antibodies: 680RD Donkey anti-Chicken IgG (1:10,000), 800CW Donkey anti-Rabbit IgG (1:10,000) in Odyssey Blocking Buffer (TBS) + 0.2% Tween® 20. Membranes were protected from light during incubation with secondary mixture for one hour at room temperature with gentle shaking. Membranes were subsequently washed with 1X TBS-T and imaged with the Odyssey® imaging system. Images were analyzed using ImageJ.

Statistical analyses

For survival data, results were plotted using a Kaplan-Meier curve and statistical significance was determined via a log-rank test, (n = 10 mice/group). For tumor growth data, statistical significance was determined using a two-way analysis of variance (ANOVA) (n = 10 mice/group). For all flow and arginase data, mice were sacrificed during the third week of treatment. For dot plots, each dot represents one mouse and each bar represents mean ± SEM. (n = 3-5 mice/group). Significance was determined by a one-way ANOVA with Tukey's multiple comparisons test. All experiments were repeated at least 3 times. All statistical analysis listed here were performed using GraphPad Prism v7.00. Statistically significant p values are abbreviated as follows: *$p<0.05$, **$p<0.01$, ***$p<0.001$, ****$p<0.0001$.

Supplementary Table 1

Target	Color	Clone	Vendor, Catalogue #
Arg-1	PE	Polyclonal	R&D Systems, IC586-8P
CD11b	AF700	M1/70	BD Biosciences, 557960
CD28	AF647	37.51	BD Biosciences, 562767
CD3	PE-Dazzle 594	17A2	BioLegend, 100246
	BV510		BioLegend, 100234
	APC		BD Biosciences, 565643
CD4	PE-Dazzle 594	RM4-5	BioLegend, 100536
	AF700		ThermoFisher, 56-0042-82
CD44	PE	IM7	BD Bioscience, 553134
CD62L	APC	MEL-14	BioLegend, 104411
CD8	PE-Cy7	53-6.7	BioLegend, 100722
	Pacific Blue		BioLegend, 100725
	BV510		BD Biosciences, 563068
CTLA-4	PE	UC10-4F10-11	BD Biosciences, 553720
EOMES	AF488	Dan11mag	eBioscience, 53-4875-82
F4/80	PE-Cy7	BM8	BioLegend, 123114
	BV510		BioLegend, 123135
FoxP3	FITC	FJK-16s	ThermoFisher, 11-5773-82
Granzyme B	PE-Cy7	NGZB	ThermoFisher, 25-8898-82
INFg	PerCP-Cy5.5	XMG1.2	ThermoFisher, 45-7311-82
Lag3	PerCP-Cy5.5	C9B7W	BD Biosciences, 564673
Ly6C	PerCP-Cy5.5	HK1.4	BioLegend, 128011
	eFluor450		ThermoFisher, 48-5932-82
Ly6G	FITC	1A8	BD Biosciences, 551460
	BV421		BD Biosciences, 562737
PD-1	APC-R700	29F.1A12	BD Biosciences, 565815
	APC		BioLegend, 135210
	PE-Cy7		BioLegend, 135216
PD-L1	PE-Dazzle 594	10F.9G2	BioLegend, 124324
Tbet	PE-Cy7	4B10	BioLegend, 644824
Thy1.2	APC	53-2.1	BD Bioscience, 553007
TIM3	eFluor450	8B.2C12	ThermoFisher, 48-5871-82

Supplementary Table 1: Antibodies used for flow cytometry. All antibodies were titrated for use with specified flow cytometers.

Supplementary Figure 1: Flow cytometry gating strategy to identify G- and M-MDSCs. (**a**) Debris was excluded form bulk tumor based on forward scatter and side scatter. Single cells were then gated by forward scatter-area and forward scatter-height. Dead cells were then gated out of the single cell bulk tumor population. T cells and mature macrophages were gated out by selecting the CD3 and F4/80 double negative population. $CD11b^{+}$ cells were then gated, and G- and M-MDSCs were identified using Ly6G vs. Ly6C. G-MDSCs were defined as $Ly6G^{+}$ $Ly6C^{lo}$ and M-MDSCs were defined as $Ly6G^{-}$ $Ly6C^{+}$. (**b**) Original flow cytometry T cell and MDSC panels gated out debris from bulk tumor based on forward scatter and side scatter. Dead cells were then gated out of the bulk tumor population. Bulk T cells were gated by selecting the CD45 and CD3 double positive population while bulk myeloid cells were gated by selecting the CD45 and CD11b double positive population. Subsequent gating of specific T cell and MDSC populations were then performed as described in Supplemental Fig. 1a and 2.

Supplementary Figure 1

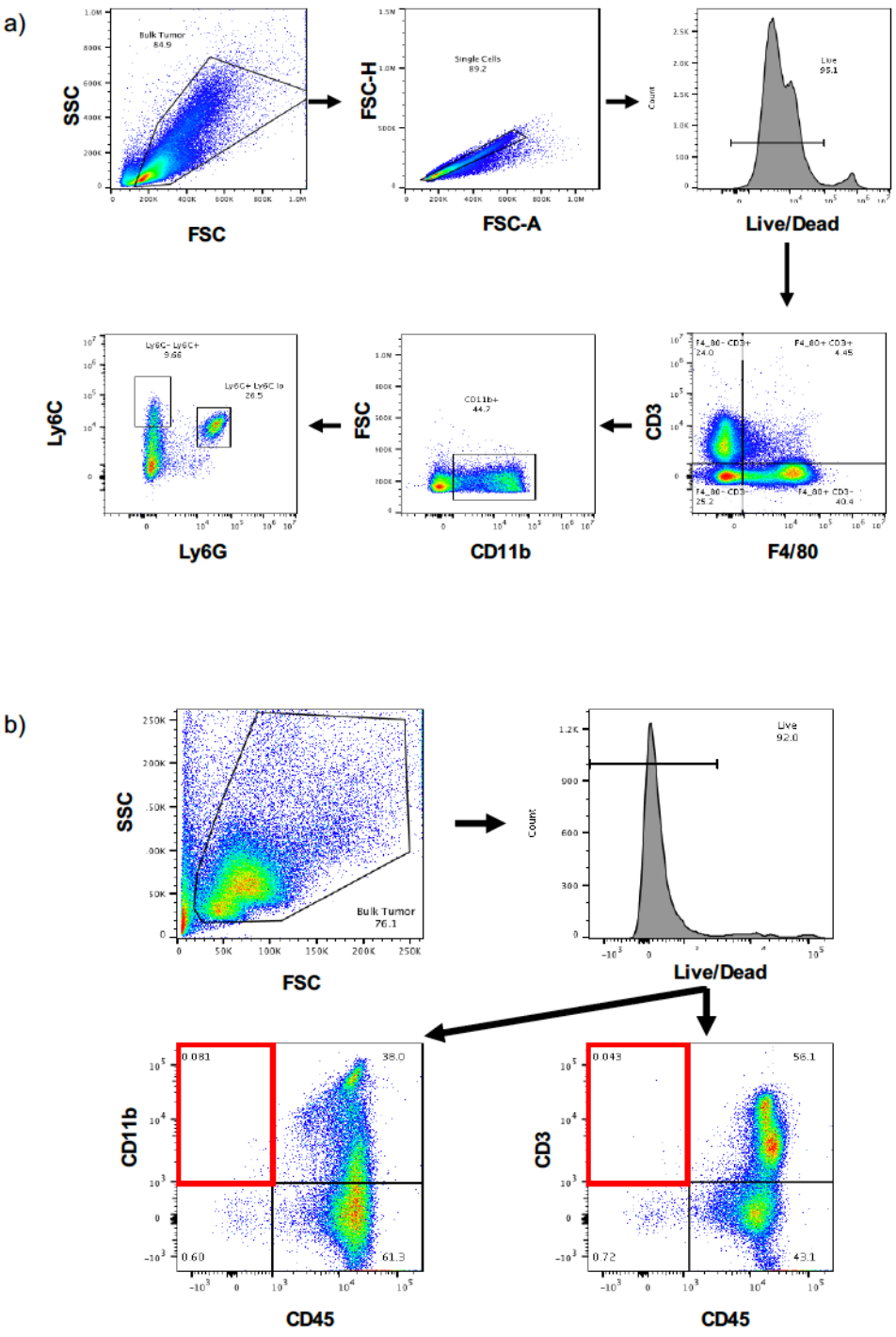

Supplementary Figure 2: Flow cytometry gating strategy to identify $CD8^+$ T cell activation and exhaustion status and QC plots for NanoString cell typing. (**a**) Debris was excluded from bulk tumor based on forward scatter and side scatter. Dead cells were then gated out of the bulk tumor cell population and then gated by CD4 vs. CD8. To determine the activation state of $CD8^+$ T cells, $CD8^+$ cells were then gated by CD44 vs. CD62L as well as CD8 vs. granzyme-B. The exhaustion state of $CD8^+$ T cells was determined by gating $CD8^+$ cells by PD-1 vs. Lag3. The QC plot for the "T-cell" set (**b**) uses expression data from the genes *Cd3g* and *Cd3d* to call this cell type. The QC plot for the "exhausted CD8" (**c**) shows expression data from *Lag3*.

Supplementary Figure 2

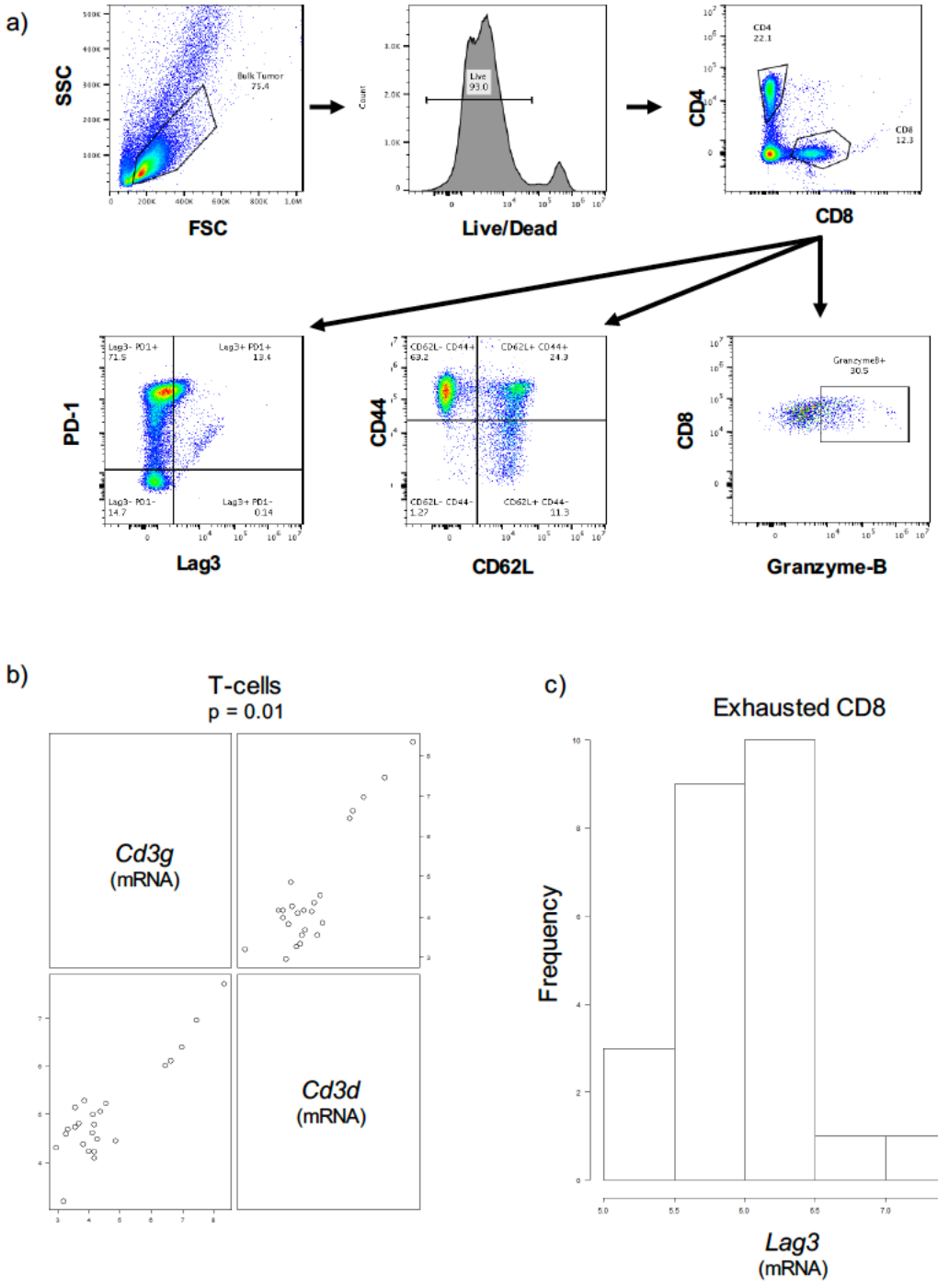

Results

*Baseline expression of immune checkpoints on bulk tumor and immune cell***s**

Previous studies have examined the expression of PD-L1 as a predictor of response and show varied correlation between protein expression and response (6,58,59). Thus, we evaluated changes in expression of PD-1, PD-L1, and CTLA-4 via flow cytometry in bulk tumors, as well as on intratumoral $CD8^+$ T cells, $CD4^+$ T cells, and MDSCs (cell types determined by gating strategies outlined in methods section) to determine if changes in expression following treatment with ENT alone validates a rationale for combining ICIs with ENT. We found no significant changes in expression of these checkpoint molecules on bulk tumor, as well as on intratumoral $CD8^+$ T cells, $CD4^+$ T cells, and MDSCs, with the exception of PD-1 expression on $CD8^+$ T cells, which showed an increase in expression (Supplementary Fig. S3a-d). Thus, we considered that increased expression of checkpoint molecules within the TME may not be predictive of response to ICIs in our models. However, various groups have previously shown synergy between HDAC inhibition and various immunotherapies, including checkpoint inhibition, which does provide rationale for addition of these checkpoint inhibitors to ENT as completed in our study (29–31,51,52). Specifically, previous studies showed that in the 4T1 breast cancer model, 5-azacytidine + ENT decreased infiltration of MDSCs into the tumor and concluded that it was ENT driving this effect (29). We also performed a comparison of the HDACis ENT and ACY-1215 as well as a demethylating agent (SGI-110) in the murine PDAC model. We determined only ENT significantly improved survival over other drugs (Supplementary Fig. S4a). Thus, we chose to move forward using ENT given its efficacy in both tumor models. We substituted anti–PD-1 for GVAX

Supplementary Figure 3: Pre-treatment with ENT does not induce significant changes in expression of PD-1, PDL-1 or CTLA-4. Tumors were isolated from neu-N mice following no treatment (Untreated) vs. mice treated with ENT for 3 weeks (ENT). PD-1, PD-L1, and CTLA-4 expression were evaluated by FACS and cells were gated as follows: debris was gated out using forward and side scatter, live cells were selected following staining with Live/Dead Near IR, and respective positive populations for each checkpoint were quantified. There were no significant changes in expression of PD-1, PDL-1 and CTLA-4 in bulk tumor **(a)**, and on intratumoral CD8 **(b)**, CD4 **(c)** and MDSCs **(d)** following treatment with ENT. For survival data, results were plotted using a Kaplan-Meier curve and statistical significance was determined via a log-rank test, (n = 10 mice/group). For tumor growth data, statistical significance was determined using a two-way ANOVA (n = 10 mice/group). All experiments were repeated at least 3 times. Statistically significant p values are abbreviated as follows: *$p<0.05$, **$p<0.01$, ***$p<0.001$, ****$p<0.0001$.

Supplementary Figure 3

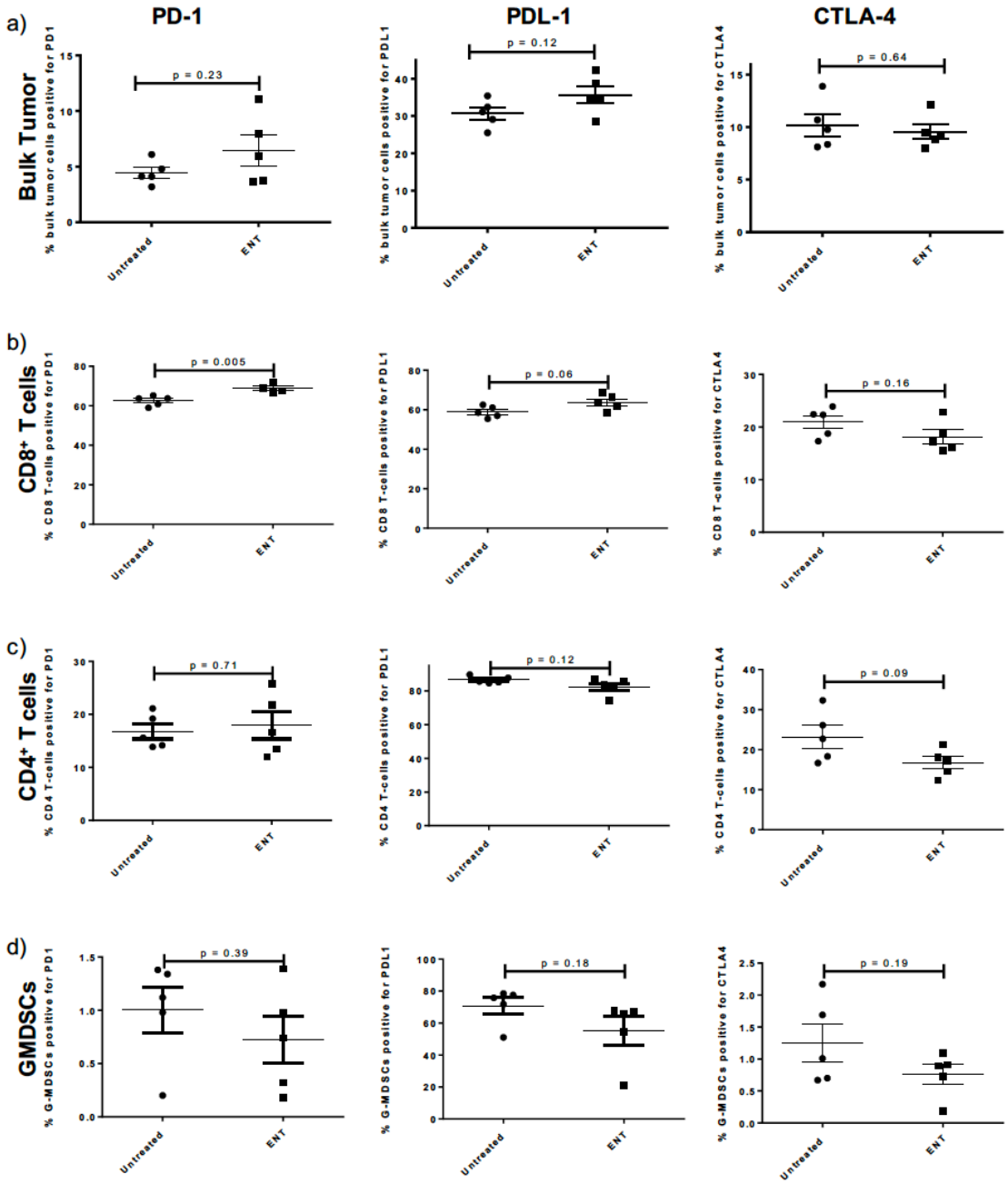

Supplementary Figure 4

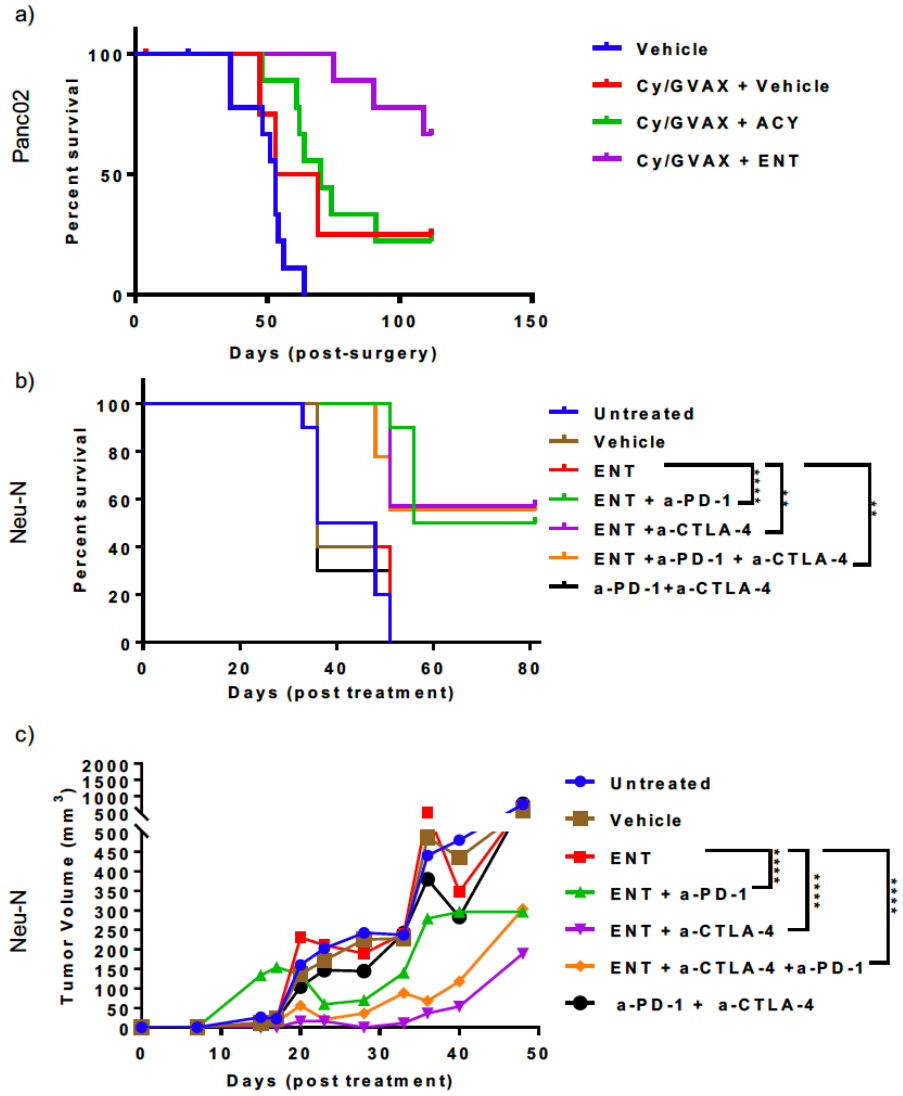

Supplementary Figure 4: ENT improves survival over other HDACi's and addition of ENT to checkpoint inhibition significantly improves survival and slows tumor progression. Initial experiments in the Panc02 model were done in combination with an allogeneic whole tumor cell vaccine that is engineered to secrete G-MCSF (GVAX) (50). Addition of ACY-1215 did not improve survival beyond that of GVAX alone and was inferior to ENT **(a)**. Survival **(b)** and tumor growth **(c)** of neu-N mice receiving ENT and ICIs without anti-HER2. Statistics for tumor growth calculated at day 48.

as our immunotherapy, which yielded the same survival benefit when combined with ENT (Fig. 1b, Supplementary Fig. S4a). Thus, moving forward we used checkpoint inhibitors as our immunotherapy instead of GVAX.

ENT priming sensitizes tumors to checkpoint inhibition and improves survival

We hypothesized that ENT would sensitize naturally immune-resistant tumors, which often fail to recruit T cells into their TME, to ICIs. To test this hypothesis, we evaluated ENT given in combination with anti–PD-1, anti–CTLA-4, or a combination of the three drugs in neu-N/HER2$^+$ breast cancer and Panc02 metastatic PDAC models. A final dosing schedule is shown in Fig. 1a. In the PDAC model, ENT+anti–PD-1, ENT+anti–CTLA-4, ENT+both ICIs, and anti-PD-1+anti-CTLA-4 significantly improved survival over treatment with vehicle or ENT alone (Fig. 1b). In the neu-N model, treatment with anti-HER2 significantly improves survival and inhibits tumor growth (Fig. 1c, 1d), consistent with studies showing efficacy in patients treated with HER-directed therapy (60). Combination ENT+anti–PD-1+anti-HER2, ENT+anti–CTLA-4+anti-HER2, or ENT+anti-HER2+both ICIs significantly improved survival compared to vehicle or ENT alone in the neu-N breast tumor model (Fig. 1c). Combination immunotherapy alone did not improve survival when compared to vehicle or ENT (Fig. 1c). The combination of ENT+both ICIs in the absence of anti-HER2 significantly improved survival (Supplementary Fig. S4b). Future studies will focus on the specific contribution of anti-HER2 to these therapies. However, for the remainder of the experiments presented herein, addition of anti-HER2 served to prove that the results were similarly efficacious (with and without it) to better inform the use of ENT+ICIs in

Figure 1: Addition of entinostat to checkpoint inhibition significantly improves survival and slows tumor progression. (a) Timeline of study design. In the neu-N model, ENT treatment was started 3 days following tumor implantation. For the metastatic pancreatic cancer model, ENT treatment began 7 days after hemisplenectomy and tumor implantation. In both models, ENT was given for 5 consecutive days each week over the course of 3 weeks. ICI antibody dosing was performed biweekly, whereas anti-HER2 was given weekly. For survival studies, mice continued to receive two doses of ICI antibody as well as one dose of anti-HER2 (neu-N model only) every other week after the first three weeks of treatment. Mice did not continue to receive ENT after the first three weeks of treatment. This was considered the maintenance phase of treatment. For all immune infiltrate analyses, mice were sacrificed during the third week of treatment. **(b)** Survival of PDAC mice receiving ENT and ICIs. **(c)** Survival and **(d)** tumor growth of neu-N mice receiving ENT and ICIs with anti-HER2. Statistics for tumor growth were calculated at day 43. For survival data, results were plotted using a Kaplan-Meier curve and statistical significance was determined via a log-rank test, (n = 10 mice/group). For tumor growth data, statistical significance was determined using a two-way ANOVA (n = 10 mice/group). All experiments were repeated at least 3 times. Statistically significant p values are abbreviated as follows: *$p<0.05$, **$p<0.01$, ***$p<0.001$, ****$p<0.0001$.

Figure 1

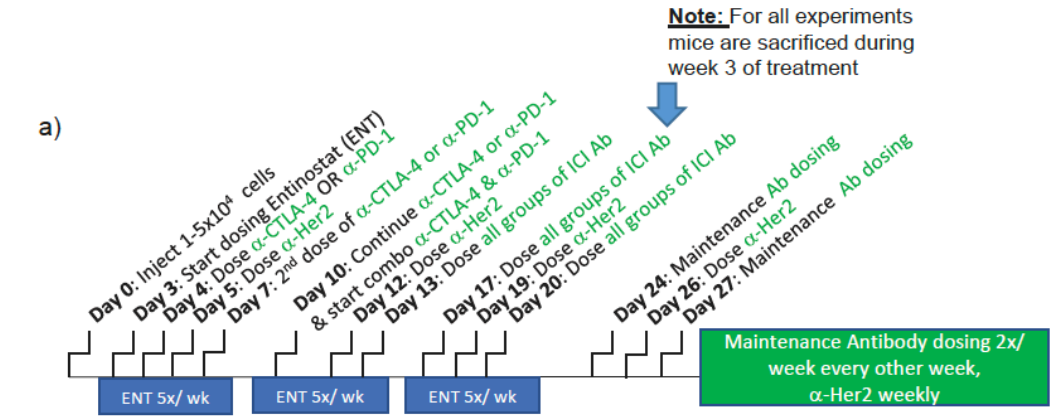

Note: For Panc02 model, treatment with ENT is started Day 7 post surgery

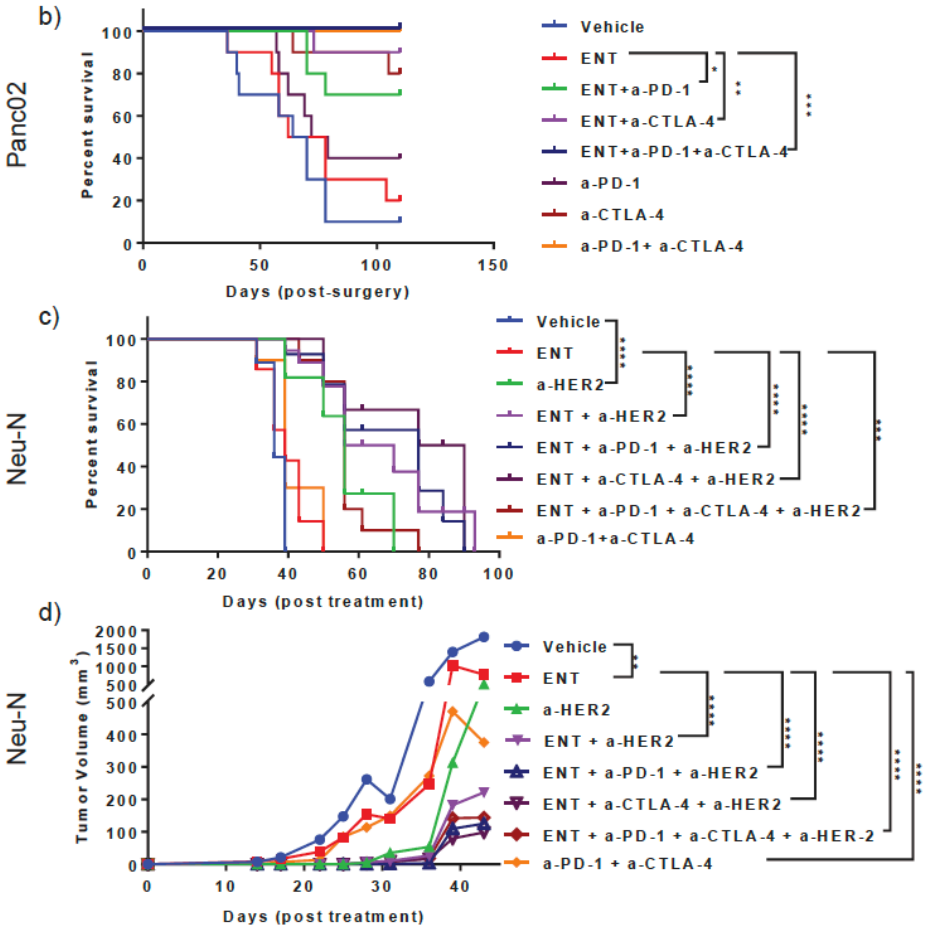

patients receiving ongoing anti-HER2 therapy. Combination therapies with ENT+single ICIs led to a significant decrease in tumor burden in the neu-N model, both with and without anti-HER2 (Fig. 1c, Supplementary Fig. S4c)**.**

Combined therapy shifts the TME from an M-MDSC to a G-MDSC dominated milieu

Given the improved antitumor immune responses observed in the mouse tumors, we next asked if ENT+ICIs were affecting MDSCs, as previous studies demonstrate decreased recruitment of MDSCs into the TME following similar therapies (29). To evaluate changes in MDSC populations, breast tumors and PDAC liver metastases were harvested following a full course of treatment. Immune cells were isolated and were characterized as G- and M-MDSCs via flow cytometry (Fig. 2a, Supplementary Methods Fig. S1a). Analysis showed that treatment with ENT in combination with anti–PD-1 or anti–CTLA-4 shifted the MDSC population to be dominated by the less immunosuppressive G-MDSCs (21) (Fig. 2b, 2c). Single-agent treatment with ENT significantly increased G-MDSCs in PDAC hepatic metastases (Fig. 2c), resembling the increase trends observed in the periphery of tumor-bearing neu-N mice (Supplementary Fig. S5a, S5b). However, the addition of ICIs was required to observe significant G-MDSC induction in the primary breast tumors. The observed increase in G-MDSCs was not the result of a redistribution between the proportions of myeloid cells since treatment of mice with combination therapies significantly increased the absolute number of G-MDSCs adjusted to tumor or liver weight (Supplementary Fig. S5c, S5d). Treatment with

Figure 2: ENT+ICIs significantly increases infiltration of G-MDSCs into the tumor microenvironment. (a) Gating strategy for identification of MDSCs by flow cytometry. G-MDSCs: $CD3^{-}F4/80^{-}CD11b^{+}Ly6G^{+}Ly6C^{lo}$; M-MDSCs: $CD3^{-}F4/80^{-}CD11b^{+}Ly6G^{-}Ly6C^{+}$. **(b)** Changes in G-MDSC infiltration in breast tumors and **(c)** hepatic metastases of PDAC mice. **(d)** Changes in M-MDSC infiltration is in breast tumors of neu-N mice and **(e)** in hepatic metastases of PDAC mice. In all experiments, cells were isolated from breast tumors and livers containing PDAC metastases, respectively. For all flow data, mice were sacrificed during the third week of treatment. Each dot represents one mouse and each bar represents mean ± SEM. (n = 3-5 mice/group). Significance was determined by a one-way ANOVA with Tukey's multiple comparisons test. All experiments were repeated at least 3 times. Statistically significant p values are abbreviated as follows: *p<0.05, **p<0.01, ***p<0.001, ****p<0.0001.

Figure 2

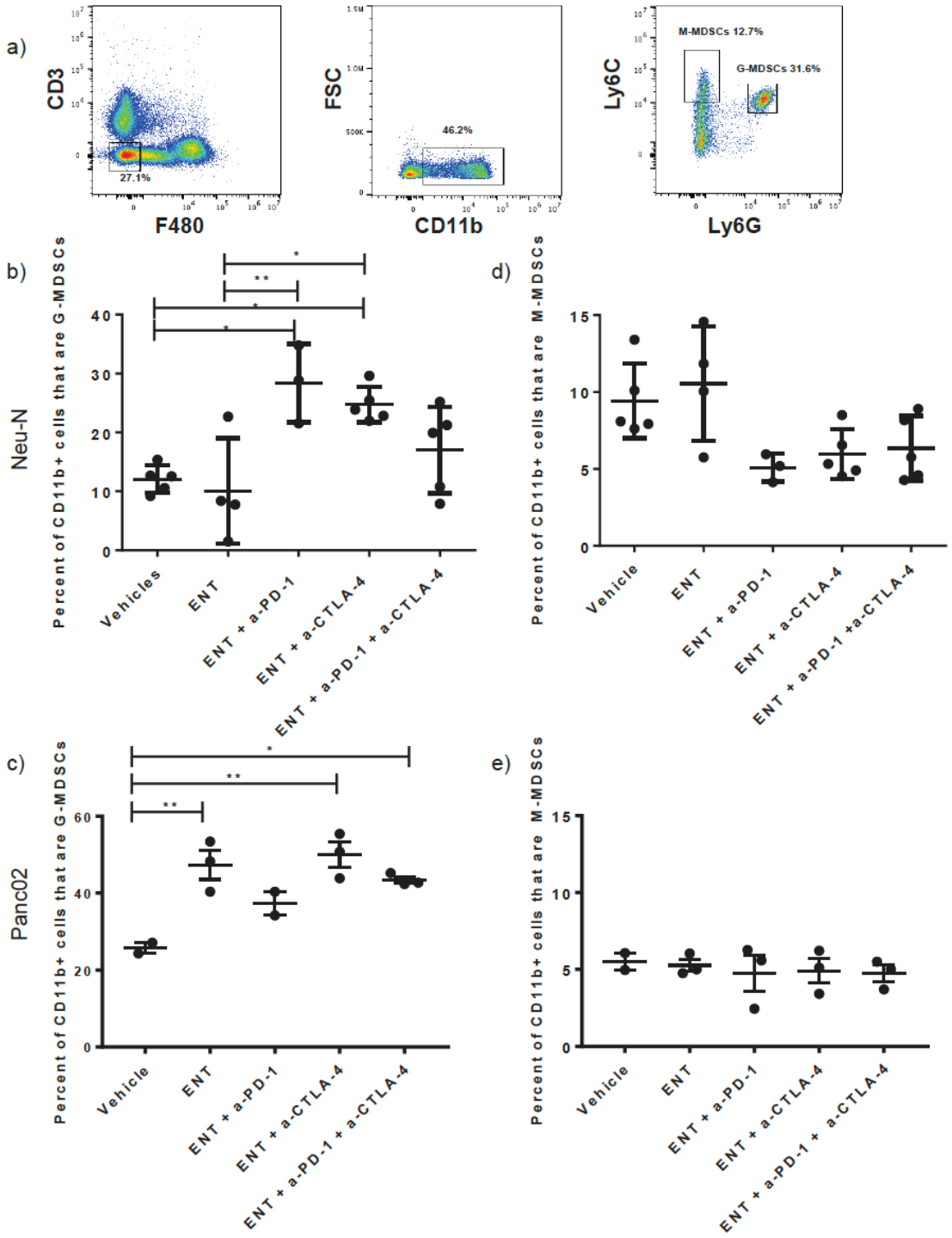
a)
CD3
F480
27.1%
FSC
CD11b
46.2%
Ly6C
Ly6G
M-MDSCs 12.7%
G-MDSCs 31.6%
b)
Neu-N
Percent of CD11b+ cells that are G-MDSCs
Vehicles
ENT
ENT + a-PD-1
ENT + a-CTLA-4
ENT + a-PD-1 + a-CTLA-4
d)
Percent of CD11b+ cells that are M-MDSCs
Vehicle
ENT
ENT + a-PD-1
ENT + a-CTLA-4
ENT + a-PD-1 +a-CTLA-4
c)
Panc02
Percent of CD11b+ cells that are G-MDSCs
Vehicle
ENT
ENT + a-PD-1
ENT + a-CTLA-4
ENT + a-PD-1 + a-CTLA-4
e)
Percent of CD11b+ cells that are M-MDSCs
Vehicle
ENT
ENT + a-PD-1
ENT + a-CTLA-4
ENT + a-PD-1 + a-CTLA-4

Supplementary Figure 5

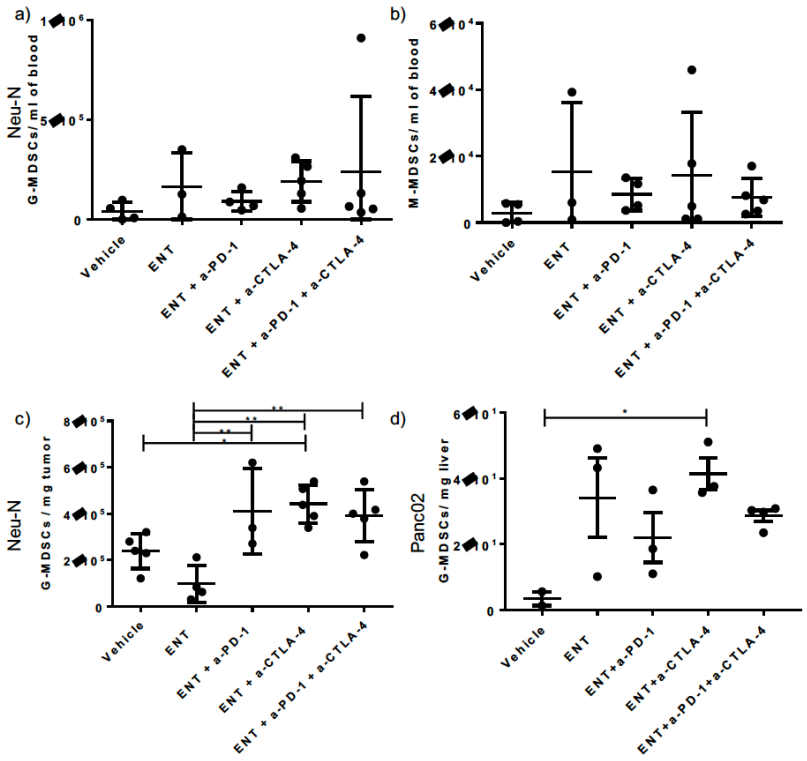

Supplementary Figure 5: Both circulating MDSCs and absolute numbers of G-MDSCs infiltrating neu-N and Panc02 tumors increase with entinostat treatment. Changes in peripheral G-MDSCs **(a)** and M-MDSCs **(b)** isolated from circulating blood of tumor bearing neu-N mice determined via flow cytometry. Cells were isolated from a minimum of 200 µl of circulating blood from neu-N mice. G-MDSCs quantified using flow cytometry from neu-N tumors **(c)** or from hepatic Panc02 metastases **(d)** normalized by weight of tumor or liver. For all flow data, mice were sacrificed during the third week of treatment. Each dot represents one mouse and each bar represents mean±SEM. (n = 3-5 mice/group). Significance was determined by a one-way ANOVA with Tukey's multiple comparisons test. All experiments were repeated at least 3 times. Statistically significant p values are abbreviated as follows: *p<0.05, **p<0.01, ***p<0.001, ****p<0.0001.

ICIs alone did not alter MDSC infiltration into the TME compared to vehicle, and no significant difference in infiltration by M-MDSCs in either model was seen (Fig. 2d, 2e).

ENT alters G-MDSC function, rendering them less immune suppressive

Because we observed increased recruitment of G-MDSCs into tumors of mice in the setting of decreased tumor burden, we evaluated the function of these cells. Traditionally, production of Arg-1 by MDSCs is used as a marker of their immunosuppressive capability (30). Thus, we performed immunosuppression assays and determined Arg-1 production both *ex vivo* and by flow cytometry. Data from immunosuppression assays revealed that the ability of G-MDSCs to suppress T-cell proliferation is inhibited in mice receiving ENT (Fig. 3a). Arg-1 protein expression was evaluated in both G- and M-MDSCs using a colorimetric arginase activity assay in the neu-N model (Fig. 3b, 3c) and by flow cytometry in the neu-N and PDAC models (Supplementary Fig. S6a-d). Results from both assays indicated that G- and M-MDSCs isolated from ENT+ICI-treated mice produced significantly less Arg-1. Taken together, these data suggest that the impaired immunosuppressive function of tumor-infiltrating G-MDSCs is, at least in part, due to decreased Arg-1 production. Evaluation of PD-L1 was also investigated as a measure of MDSC suppressive cell function. We analyzed the surface expression of PD-L1 on intratumoral G-MDSCs by flow cytometry. PD-L1 expression was significantly reduced on G-MDSCs with ENT+ICI treatment (Supplementary Fig. S6e, S6f). This suggested that treatment of G-MDSCs with ENT reduced their ability to inhibit T-cell activity by diminishing availability of the PD-L1/PD-1 T-cell inhibitory pathway.

Figure 3

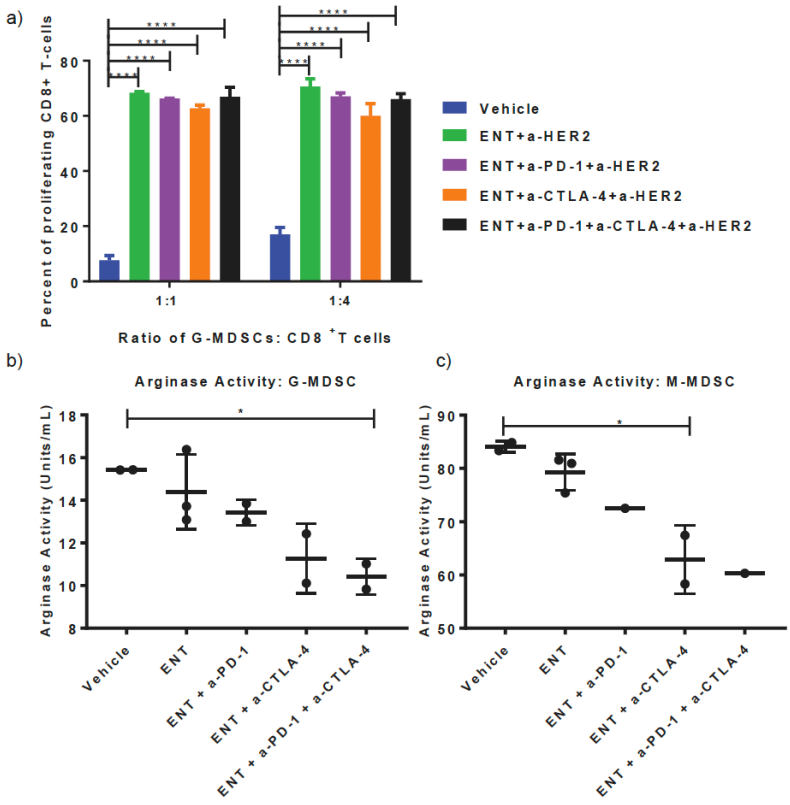

Figure 3: ENT+ICI combination therapy inhibits immunosuppressive functions of MDSCs. **(a)** Ly6G^{+} G-MDSCs isolated from breast tumors of individual animals were co-cultured with naïve neu-specific CD8^{+} T cells and peptide-pulsed APCs. Proliferation was determined by CFSE staining. Each bar is an average of 3-4 mice per treatment group. Error bars indicate mean±SEM. Significance was determined by a one-way ANOVA with Tukey's multiple comparisons test. Changes in arginase activity of **(b)** G-MDSCs and **(c)** M-MDSCs isolated from treated breast tumors determined via colorimetric assay. For arginase data, mice were sacrificed during the third week of treatment. Each dot represents one mouse and each bar represents mean±SEM. (n = 3-5 mice/group). All experiments were repeated at least 3 times. Statistically significant p values are abbreviated as follows: *p<0.05, **p<0.01, ***p<0.001, ****p<0.0001.

Supplementary Figure 6: Entinostat decreased expression of MDSC functional markers by flow cytometry and decreases expression of PD-L1—an alternative functional marker of G-MDSCs. Changes in expression of Arg-1 in G-MDSCs **(a)** and M-MDSCs **(b)** from neu-N tumors as evaluated by flow cytometry. Cells were isolated from breast tumors. Changes in expression of Arg-1 in G-MDSCs **(c)** and M-MDSCs **(d)** from livers containing PDAC metastases as evaluated by flow cytometry. Changes in expression of PD-L1 on G-MDSCs isolated from neu-N tumors **(e)** and from livers containing PDAC metastases **(f)** as evaluated by flow cytometry. For all flow data, mice were sacrificed during the third week of treatment. Each dot represents one mouse and each bar represents mean±SEM. (n = 3-5 mice/group). Significance was determined by a one-way ANOVA with Tukey's multiple comparisons test. All experiments were repeated at least 3 times. Statistically significant p values are abbreviated as follows: *$p<0.05$, **$p<0.01$, ***$p<0.001$, ****$p<0.0001$.

Supplementary Figure 6

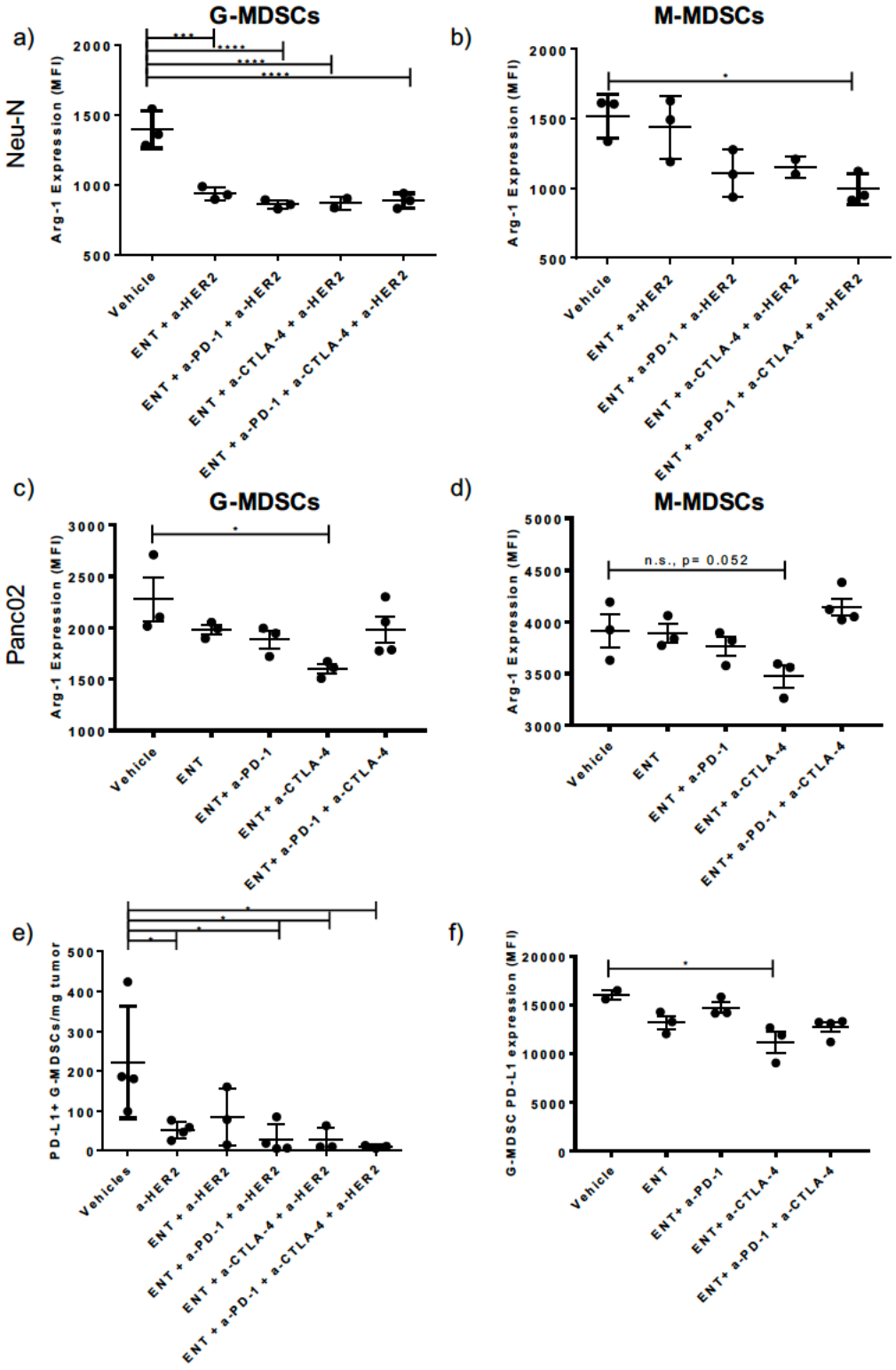

ENT+ICI therapy significantly alters the signaling pathways involved in myeloid function

ENT alters the global acetylation state of cells (61), but its effect on subpopulations of myeloid cells has not been thoroughly studied. To identify possible mechanisms for their impaired function, we utilized NanoString transcript profiling to evaluate broad changes in the transcriptome of isolated G-MDSCs induced by treatment. Treatment with ENT and subsequently anti–CTLA-4 and/or anti–PD-1 significantly altered the expression of many genes important to G-MDSC's function (Fig. 4a). Further evaluation revealed relevant pathways that were significantly up- or downregulated and contained significantly altered genes that drove the differential regulation of these pathways (Fig. 4b, 4c, Supplementary Fig. S7a, S7b). We narrowed our focus to certain pathways and genes that may be more specifically responsible for the observed MDSC phenotypes and only report treatment combinations that showed significant changes across all biological replicates (Fig. 4b, 4c). Our data reveal several observations. First, treatment with ENT alone and ENT+anti–PD-1 decreased expression of genes in both the ErbB and VEGF signaling pathways compared to vehicle-treated mice (Fig. 4b). However, expression was increased in both pathways in mice treated with ENT+anti–CTLA-4 (Fig. 4c). Second, treatment with ENT+anti–PD-1 downregulated the mTOR pathway (Fig. 4b), whereas ENT+anti–CTLA-4 increased overall expression of the pathway (Fig. 4c). Fig. 4d depicts the VEGF pathway, highlighting key genes altered due to treatment with ENT compared to vehicle. Fourth, significant changes due to ENT+ICI treatment in pathways involving adhesion and motility suggested that treatment with ENT+ICI increased G-MDSC trafficking, which may explain the observed increased in infiltration of G-MDSCs (Supplementary Fig. S7a, S7b). Fifth, changes in pathways

Figure 4: HDACi+ICI combined therapy significantly alters the signaling pathway gene expression profiles involved in myeloid function. **(a)** Heatmap of gene expression changes in all-treatment groups compared to vehicle treatment alone. Red indicates upregulation and blue indicates downregulation. **(b)** Tables listing selected significantly downregulated KEGG pathways and **(c)** significantly upregulated KEGG pathways, with the top 5 genes differentially regulated listed in last column. **(d)** Differentially regulated genes in the VEGF signaling pathway in mice treated with ENT vs. vehicle. Expression of genes listed in white boxes were measured but did not show any fold change. Expression of genes in gray boxes were not measured. NanoString gene expression profiling was performed once with at least 4 mice per group. Statistically significant p values are abbreviated as follows: *$p<0.05$, **$p<0.01$, ***$p<0.001$, ****$p<0.0001$.

Figure 4

a) Mouse Myeloid Panel of isolated G-MDSCs

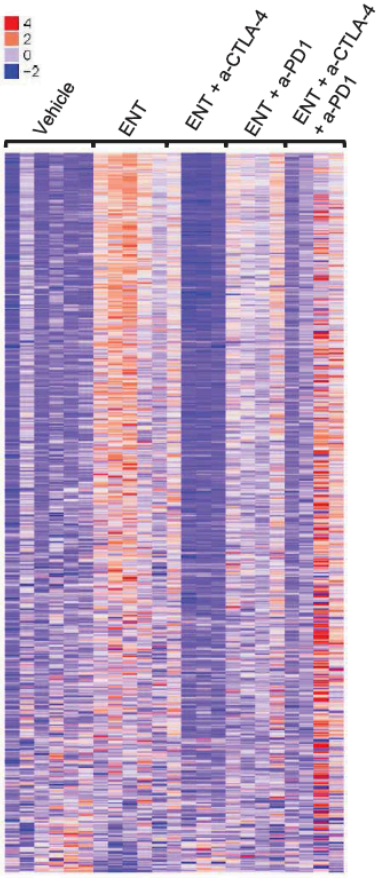

b) Pathways Downregulated

Treatment	KEGG Pathway	P-value	Most differentially expressed genes
Vehicle vs. ENT	ErbB	0.00939	Raf1, Areg, p21, Egf, Hbegf
	VEGF	0.04022	Raf1, Hras, Nfat, Pkc, p38
Vehicle vs. ENT + a-PD-1	ErBB	0.05165	Raf1, Areg, p21, Egf, Hbegf
	VEGF	0.05165	Raf1, Hras, Nfat, Pkc, p38
	mTOR	0.05165	Raf1, Fzd4, Fzd6, Fzd9, Hras

c) Pathways Upregulated

Treatment	KEGG Pathway	P-value	Most differentially expressed genes
ENT vs. ENT + a-CTLA-4	ErbB	0.00083	Raf1, Areg, p21, Egf, Hbegf
	VEGF	0.03325	Raf1, Hras, Nfat, Pkc, p38
	mTOR	0.01336	Raf1, Fzd4, Fzd6, Fzd9, Hras

d)

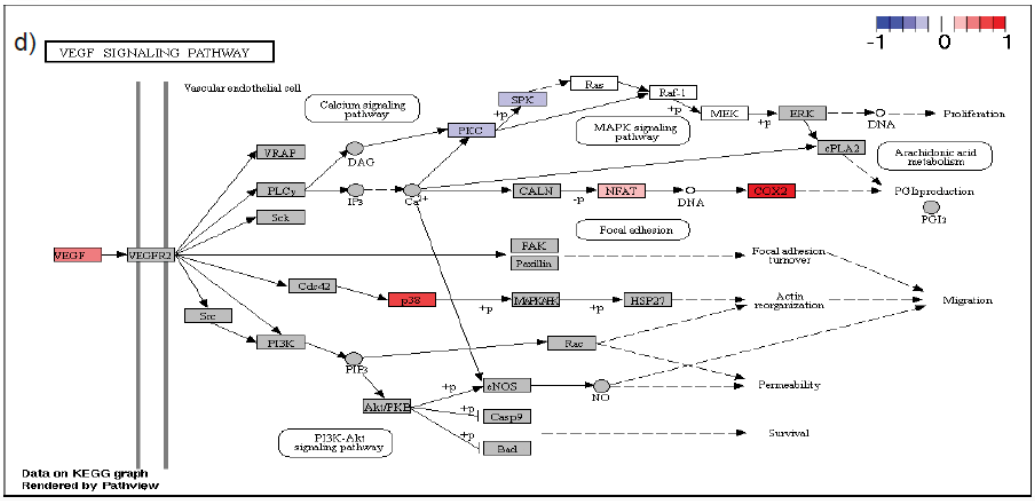

Supplementary Figure 7: HDACi + ICI combined therapy significantly alters patterns of myeloid cell functional markers on gene expression profiling. Table listing all significantly downregulated **(a)** and significantly upregulated **(b)** KEGG pathways, with the top 5 genes differentially regulated listed in last column. Selected genes alternately regulated by given treatment with p-values and fold change **(c)**. The complete list of individual genes significantly up or downregulated was over 100 genes in length and too cumbersome for publication. Please contact corresponding author for inquiries. NanoString gene expression profiling was performed once with at least 4 mice per group. Statistically significant p values are abbreviated as follows: *$p<0.05$, **$p<0.01$, ***$p<0.001$, ****$p<0.0001$.

Supplementary Figure 7

a) Pathways Downregulated

Treatment	KEGG Pathway	P-value	Most differentially expressed genes
Vehicle vs. ENT	Gap Junction	0.0048	Raf1,Egf,Gnai3,Hras,Pdgfa
	GnRH	0.0094	Raf1,Hbegf,Hras,Jun,Prkca
	Axon guidance	0.017	Raf1,Cxcr4,Ephb6,Fyn,Gnai3
	Thyroid hormone signaling	0.0279	Raf1,Actb,Ctnnb1,Hif1a,Hras
	Pluripotency of stem cells	0.0543	Raf1,Ctnnb1,Fgf2,Fgfr1,Fzd4
Vehicle vs. ENT + a-PD-1	GnRH	0.0516	Raf1,Hbegf,Hras,Jun,Prkca
	Pluripotency of stem cells	0.0516	Raf1,Ctnnb1,Fgf2,Fgfr1,Fzd4
	Gap junction	0.0516	Raf1,Egf,Gnai3,Hras,Pdgfa
	Hippo	0.0516	Actb,Birc2,Birc5,Areg,Bmp8a
	Axon guidance	0.0516	Raf1,Cxcr4,Ephb6,Fyn,Gnai3
	Thyroid hormone	0.0516	Raf1,Actb,Ctnnb1,Hif1a,Hras
	Sphingolipid	0.0516	Raf1,AdorA1:E41a3,Bcl2,Bid,S1pr1

b) Pathways Upregulated

Treatment	KEGG Pathway	P-value	Most differentially expressed genes
ENT vs. ENT + a-CTLA-4	Gap junction	0.00069	Raf1,Egf,Gnai3,Hras,Pdgfa
	GnRH	0.00187	Raf1,Hbegf,Hras,Jun,Prkca
	Axon guidance	0.00191	Raf1,Cxcr4,Ephb6,Fyn,Gnai3
	Thyroid hormone	0.00297	Raf1,Actb,Ctnnb1,Hif1a,Hras
	Focal adhesion	0.00327	Raf1,Actb,Birc3,Birc2,Bcl2
	Sphingolipid signaling pathway	0.00486	Raf1,Adora3,Bcl2,Bid,S1pr1
	Hippo signaling pathway	0.00928	Actb,Birc2,Birc5,Areg,Bmp8a
	Pluripotency of stem cells	0.00967	Raf1,Ctnnb1,Fgf2,Fgfr1,Fzd4
	Insulin	0.01303	Raf1,Socs3,Socs1,Fasn,Fbp1
	Adherens junction	0.0205	Actb,Ctnnb1,Cdh1,Fgfr1,Fyn
	Neurotrophin	0.02087	Raf1,Bcl2,Hras,Jun,Nfkb1
	Apoptosis	0.02144	Raf1,Actb,Birc3,Birc2,Birc5
	Prolactin	0.02144	Raf1,Socs3,Socs1,Hras,Irf1
	Melanogenesis	0.02206	Raf1,Ctnnb1,Fzd4,Fzd6,Fzd9
	Tight junction	0.02281	Actb,Cd1d1,Cd1d2,Cldn1,Itgb1
	MAPK	0.03351	Raf1,Angpt1,Angpt2,Csf1,Csf1r
	Wnt	0.03438	Ctnnb1,Fosl1,Fzd4,Fzd6,Fzd9
	Rap1	0.05174	Raf1,Actb,Adora2a,Angpt1,Angpt2
	Ras	0.05174	Raf1,AnA2:D20gpt1,Angpt2,Arf6,Csf1

c)

Treatment	Gene	Fold change	P-value
Vehicle vs. ENT	Arg-1	-0.033	0.967
	Il6	3.216	0.035
	EGF	-0.078	0.924
	Vegfa	0.475	0.093
	Stat3	0.284	0.110
Vehicle vs. ENT + a-PD-1	Vegfa	0.524	0.123
	Egf	0.725	0.477
	Tnf	1.454	0.094
	Stat3	0.084	0.737
ENT vs. ENT + a-CTLA-4	Csf1	-1.671	0.006
	Csf1r	-1.022	0.073
	Vegfa	-0.846	0.011
	Egf	-0.592	0.413
	Tnf	-1.690	0.017
	Stat3	-0.408	0.034

controlling different hormone production, apoptosis, and MAPK signaling were observed (Supplementary Fig. S7a, S7b). Finally, we found over 100 significantly differentially expressed genes independent of the aforementioned pathways. Key genes of interest are listed (Supplementary Fig. S7c). Expression of significantly altered pathways and genes of interest were validated using quantitative-PCR (qPCR) (Supplementary Fig. S8). We also validated these findings by investigating changes in protein expression via western blot. EGF expression was analyzed to represent the ErbB pathway, VEGFA for the VEGF pathway, and TNFα for the mTOR pathway. Protein expression of STAT3, a key gene of interest, was evaluated along with activation of the STAT3 protein via phosphorylation at Tyr705. These data show that although the protein expression changes observed in G-MDSCs isolated from treated mice did not correlate with changes seen at the mRNA level (Supplementary Fig. S9a, S9b, Supplementary Fig. S7c), a decrease in phospho-STAT3 was observed in treated mice (Supplementary Fig. S9a, S9b), indicating a decrease in STAT3 activity. Changes in protein expression of EGF, VEGFA, and TNFα correlated with mRNA expression in groups treated with ENT+anti–CTLA-4 compared to ENT-treated animals (Supplementary Fig. S9c). Changes in protein expression of EGF correlated with mRNA expression in groups treated with ENT compared to vehicle-treated animals (Supplementary Fig. S9d). However, changes in EGF protein expression did not correlate with mRNA expression in the ENT+anti–PD-1 group compared to vehicle-treated animals (Supplementary Fig. S7c, S9e). No correlation between changes in VEGFA protein expression and mRNA expression in either the ENT or ENT+anti–PD-1 groups was seen (Supplementary Fig. S9d, S9e), as well as for TNFα expression in the ENT+anti–PD-1 group (Supplementary Fig. S9e). Future work will

Supplementary Figure 8

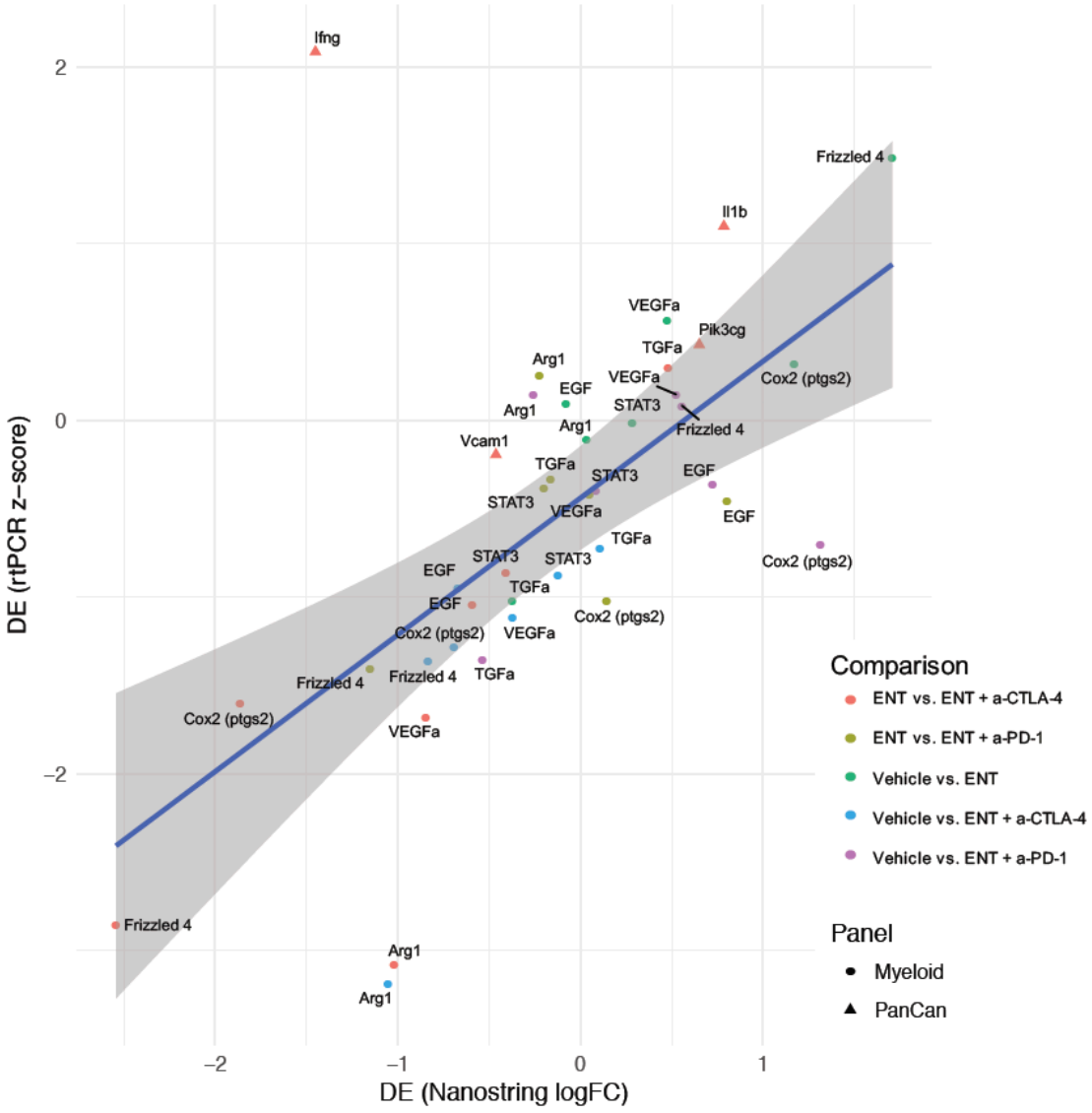

Supplementary Figure 8: qPCR validation of the NanoString platform.

Reverse transcription of mRNA and subsequent qPCR was performed on RNA isolates to validate expression level changes seen in NanoString analysis. RNA was extracted from isolated G-MDSCs and whole tumor. Gene expression was quantified from raw data by calculating mean CT values from the three replicates and comparing the ΔCT values of each gene to the 18s reference gene. Fold changes were quantified as 2^ΔΔCT and plotted against corresponding NanoString fold change values.

Supplementary Figure 9: Changes in protein expression of STAT3, phospho-STAT3 and representative proteins from pathways identified by NanoString. Protein levels of EGF (representative of the ErbB pathway), VEGFA (representative of the VEGF pathway), TNFα (representative of the mTOR pathway), STAT3, and phospho-STAT3 in G-MDSCs isolated from the TME of treated animals were determined via western blot analysis. (**a**) Representative western blots depicting changes in STAT3 and phospho-STAT3 expression in treated animals in the neu-N model (**b**) Quantification of fold changes in STAT3 and phospho-STAT3 expression in treated mice in the neu-N mode normalized to vehicle or ENT as indicated. (**c**) Fold change in expression of EGF, VEGFA, and TNFα in ENT+anti-CTLA-4 treated animalsnbnormalized to ENT (**d**) Fold change in expression of EGF and VEGFA in ENT treated animals normalized to vehicle (**e**) Fold change in expression of EGF, VEGFA, and TNFα in ENT+anti-PD-1 treated animals normalized to vehicle. Each blot represents G-MDSCs isolated from whole tumor of treated neu-N mice. Five animals were pooled per treatment group. All experiments were repeated once.

Supplementary Figure 9

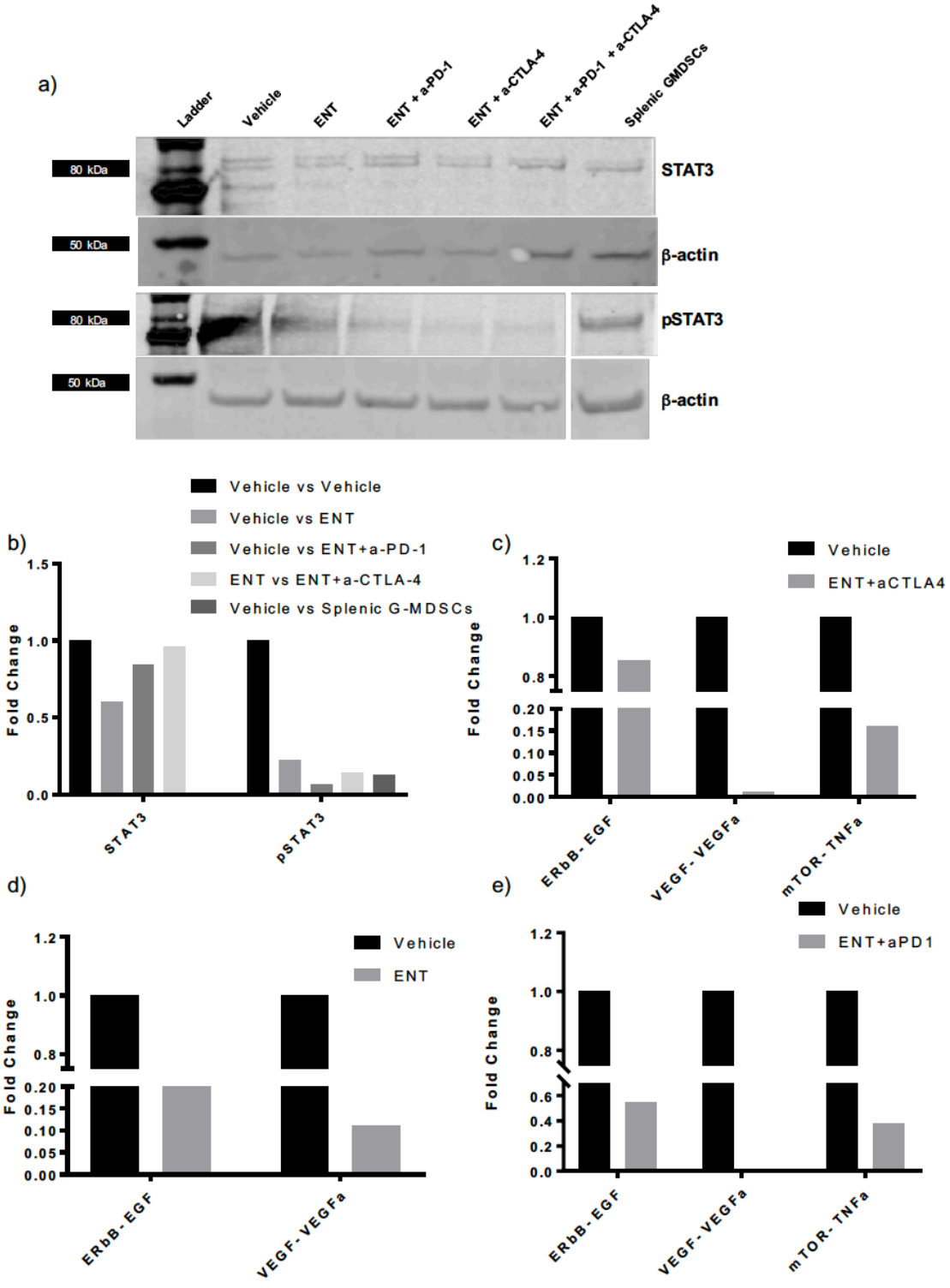

focus on changes in expression of both genes and proteins within these pathways to determine if they play a mechanistic role in altered G-MDSC function.

ENT+ICIs promote infiltration of effector CD8$^+$ T cells independent of T_{reg} infiltration

After determining that ENT+ICIs inhibited the immunosuppressive function of G-MDSCs, we sought to establish whether this change was sufficient to promote infiltration of functioning CD8$^+$ T cells into the TME (51). Cells were isolated from tumors and changes within the T-cell populations were evaluated using flow cytometry. We observed increased infiltration of CD8$^+$ T effector cells and decreased naïve and memory CD8$^+$ T cells when ENT was combined with anti–PD-1, anti–CTLA-4, or both (Fig. 5a, 5b). Evaluation of the proliferative capacity of infiltrating CD8$^+$ T cells within the PDAC TME showed increased proliferation with the addition of ICIs, determined by Ki67 staining (Supplementary Fig. S10a). PDAC mice treated with ENT+anti–CTLA-4 also showed a significant increase in granzyme-B–producing CD8$^+$ T cells. A pattern suggesting an increase in granzyme-B–producing CD8$^+$ T cells was also observed in the anti-HER2+ENT+anti–CTLA-4-treated neu-N mice. The addition of anti–PD-1 reduced this effect in both tumor types (Fig. 5c, 5d). IFNγ production by CD8$^+$ T cells was also measured. However, combination-treated mice only showed a trending increase in both models (Supplementary Fig. S10b, S10c). These data indicate that the combination of ENT with ICIs induced infiltration of effector CD8$^+$ T cells with cytotoxic capabilities. Although the CD8$^+$ T cells appeared to exhibit improved antitumor activity, we wanted to characterize the ability of treatment to promote T-cell activation versus exhaustion. We evaluated the expression of various surface markers in CD8$^+$ T cells from tumors in both

Figure 5: HDACi+ICI combination therapy promotes infiltration of activated cytotoxic CD8$^+$ effector T cells. The proportion of infiltrating CD8$^+$ naïve (CD62L$^+$CD44$^-$), effector (CD62L$^-$CD44$^+$), and memory (CD62L$^+$CD44$^+$) T cells was evaluated. **(a)** The percentage of infiltrating CD8$^+$ effector T cells in breast tumors and **(b)** PDAC hepatic metastases of treated mice. **(c-f)** Cells were isolated from breast tumors and livers containing PDAC metastases, respectively. **(c)** Change in infiltration of CD8$^+$ granzyme-B$^+$ T cells in breast tumors and **(d)** PDAC hepatic metastases of mice receiving combined therapy. **(e)** Exhaustion state of infiltrating CD8$^+$ T cells determined by co-expression of PD-1 and Lag3 in both the neu-N and **(f)** the PDAC model. For all flow data, mice were sacrificed during the third week of treatment. Each dot represents one mouse and each bar represents mean ± SEM. (n = 3-5 mice/group). Significance was determined by a one-way ANOVA with Tukey's multiple comparisons test. All experiments were repeated at least 3 times. Statistically significant p values are abbreviated as follows: *p<0.05, **p<0.01, ***p<0.001, ****p<0.0001.

Figure 5

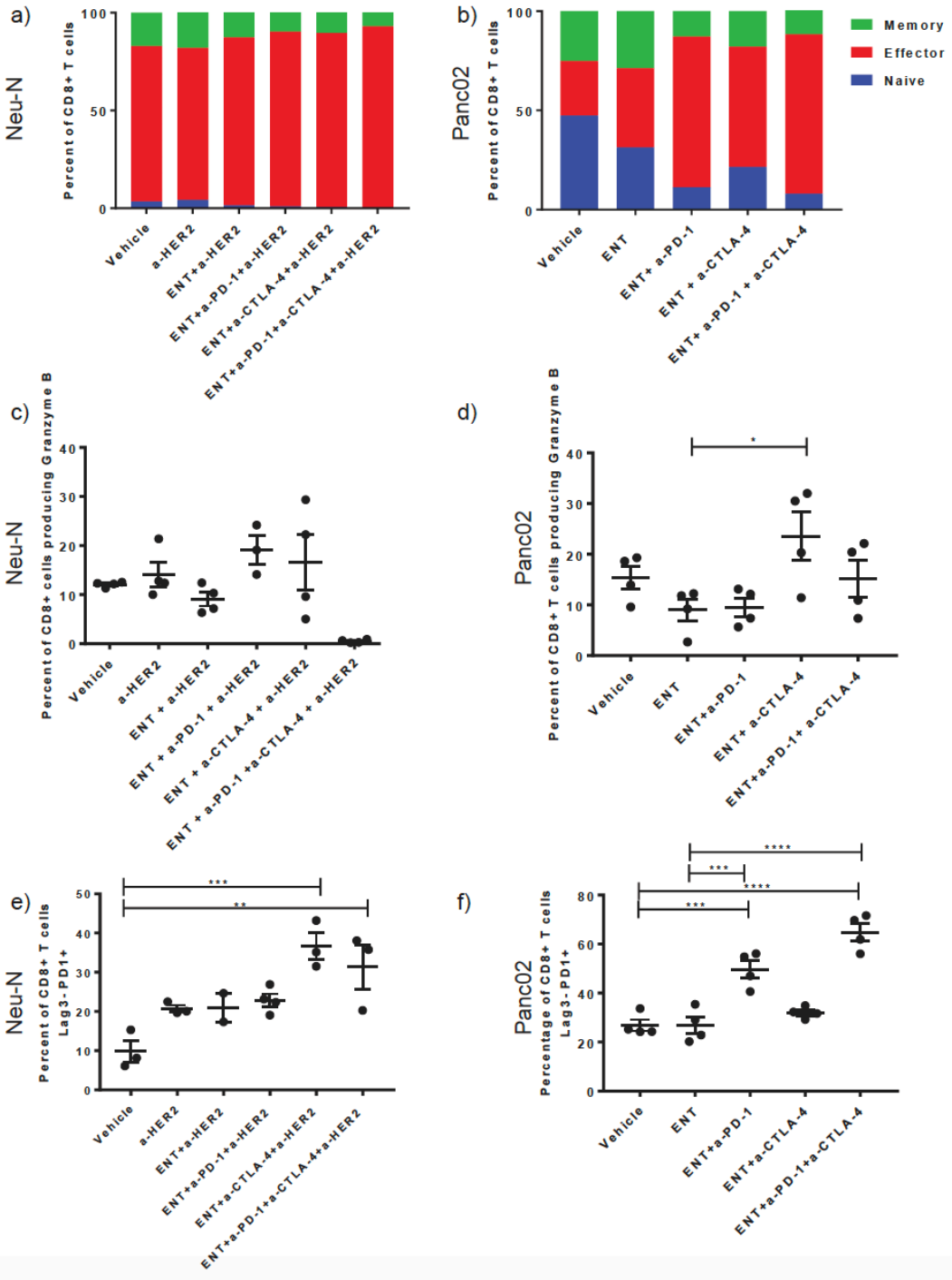
a)
Neu-N
Percent of CD8+ T cells
100
50
0
Vehicle
a-HER2
ENT+a-HER2
ENT+a-PD-1+a-HER2
ENT+a-CTLA-4+a-HER2
ENT+a-PD-1+a-CTLA-4+a-HER2
b)
Panc02
Percent of CD8+ T cells
Memory
Effector
Naive
Vehicle
ENT
ENT+ a-PD-1
ENT + a-CTLA-4
ENT+ a-PD-1 + a-CTLA-4
c)
Neu-N
Percent of CD8+ cells producing Granzyme B
40
30
20
10
0
Vehicle
a-HER2
ENT + a-HER2
ENT + a-PD-1 + a-HER2
ENT + a-CTLA-4 + a-HER2
ENT + a-PD-1 +a-CTLA-4 + a-HER2
d)
Panc02
Percent of CD8+ T cells producing Granzyme B
*
Vehicle
ENT
ENT+a-PD-1
ENT+ a-CTLA-4
ENT+a-PD-1+ a-CTLA-4
e)
Neu-N
Percent of CD8+ T cells Lag3-PD1+
***
**
50
40
30
20
10
0
Vehicle
a-HER2
ENT+a-HER2
ENT+a-PD-1+a-HER2
ENT+a-CTLA-4+a-HER2
ENT+a-PD-1+a-CTLA-4+a-HER2
f)
Panc02
Percentage of CD8+ T cells Lag3-PD1+
****
***
****
***
80
60
40
20
0
Vehicle
ENT
ENT+a-PD-1
ENT+a-CTLA-4
ENT+a-PD-1+a-CTLA-4

Supplementary Figure 10

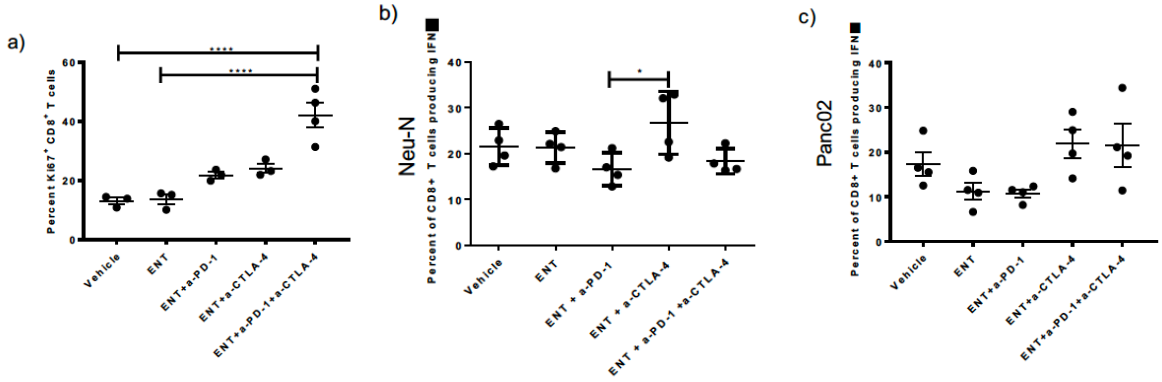

Supplementary Figure 10: Combination therapy induces T cell proliferation within the TME but does not significantly increase IFNg production. Changes in the proliferative capacity of $CD8^+$ T cells within the TME of PDAC metastases, as determined by Ki67 staining (**a**). Changes in IFNg production in $CD8^+$ T cells in either neu-N (**b**) or PDAC (**c**) models. For all flow data, mice were sacrificed during the third week of treatment. Each dot represents one mouse and each bar represents mean±SEM. (n = 3-5 mice/group). Significance was determined by a one-way ANOVA with Tukey's multiple comparisons test. All experiments were repeated at least 3 times. Statistically significant p values are abbreviated as follows: *p<0.05, **p<0.01, ***p<0.001, ****p<0.0001.

models, and first observed significantly increased expression of PD-1 (Supplementary Fig. S11a, S11b). Because PD-1 can be a sign of activation as well as exhaustion, we evaluated the co-expression of a second marker Lag3. Co-expression of these molecules is indicative of exhausted $CD8^+$ T cells, whereas the absence of Lag3 on PD-1^+ $CD8^+$ T cells is indicative of activated T cells (62,63). Our results only showed a significant increase in PD-1^+Lag$3^-$$CD8^+$ T cells infiltrating tumors from both models (Fig. 5e, 5f). We noted a pattern of non-significant increases of exhausted PD-1^+Lag$3^+$$CD8^+$ T cells (Supplementary Fig. S11c, S11d). These data support that most $CD8^+$ T cells infiltrating tumors in response to ENT+ICIs were activated and not exhausted. We also checked the co-expression of Tim3 and CTLA-4 with PD-1 as additional markers of exhaustion (62,63) and found similar trends. Analysis of transcription factor expression revealed a 50% increase in terminally exhausted $CD8^+$ T cells in mice treated with ENT+anti-PD-1+anti+CTLA-4 in both neu-N tumors and PDAC metastases (Supplementary Fig. S11e, S11f). These are also the treatment groups with the highest proliferative capacity. This analysis showed no significant change in progenitor exhausted $CD8^+$ T cells in the neu-N model and a 35-60% increase in the PDAC model (Supplementary Fig. 11g, 11h). Taken together, these data support that treatment generally induces an activated T-cell state. Previous studies revealed that ENT+interleukin-2 induces a decrease in tumor burden, which correlates with an increase in effector T cells and a reduction in tumor-infiltrating regulatory T cells (T_{regs}) (33). Because T_{regs} have also been described as a major immunosuppressive component of the TME (64), we used flow cytometry to determine if ENT altered T_{reg} infiltration. However, we only observed a trending decrease in T_{regs} in both models (Fig. 6a, 6b), which was not statistically significant.

Supplementary Figure 11: The effect of ENT+ICIs on the exhaustion state of $CD8^+$ T cells. Change in infiltration of $CD8^+$ T cells expressing PD-1 in both neu-N (**a**) and PDAC (**b**) models. Co-expression of PD-1 and Lag3 on infiltrating $CD8^+$ T cells in the neu-N (**c**) or the PDAC (**d**) models. Changes in infiltration of terminally exhausted $CD8^+$ T cells ($PD\text{-}1^{hi}$ $EOMES^{hi}$) in tumors of neu-N mice (**e**) and in the PDAC model (**f**). Changes in infiltration of progenitor exhausted $CD8^+$ T cells ($PD\text{-}1^{hi}$ $Tbet^{int}$) is observed in neu-N tumors (**g**) and in PDAC metastases (**h**). For all flow data, mice were sacrificed during the third week of treatment. Each dot represents one mouse and each bar represents mean±SEM. (n = 3-5 mice/group). Significance was determined by a one-way ANOVA with Tukey's multiple comparisons test. All experiments were repeated at least 3 times. Statistically significant p values are abbreviated as follows: *$p<0.05$, **$p<0.01$, ***$p<0.001$, ****$p<0.0001$.

Supplementary Figure 11

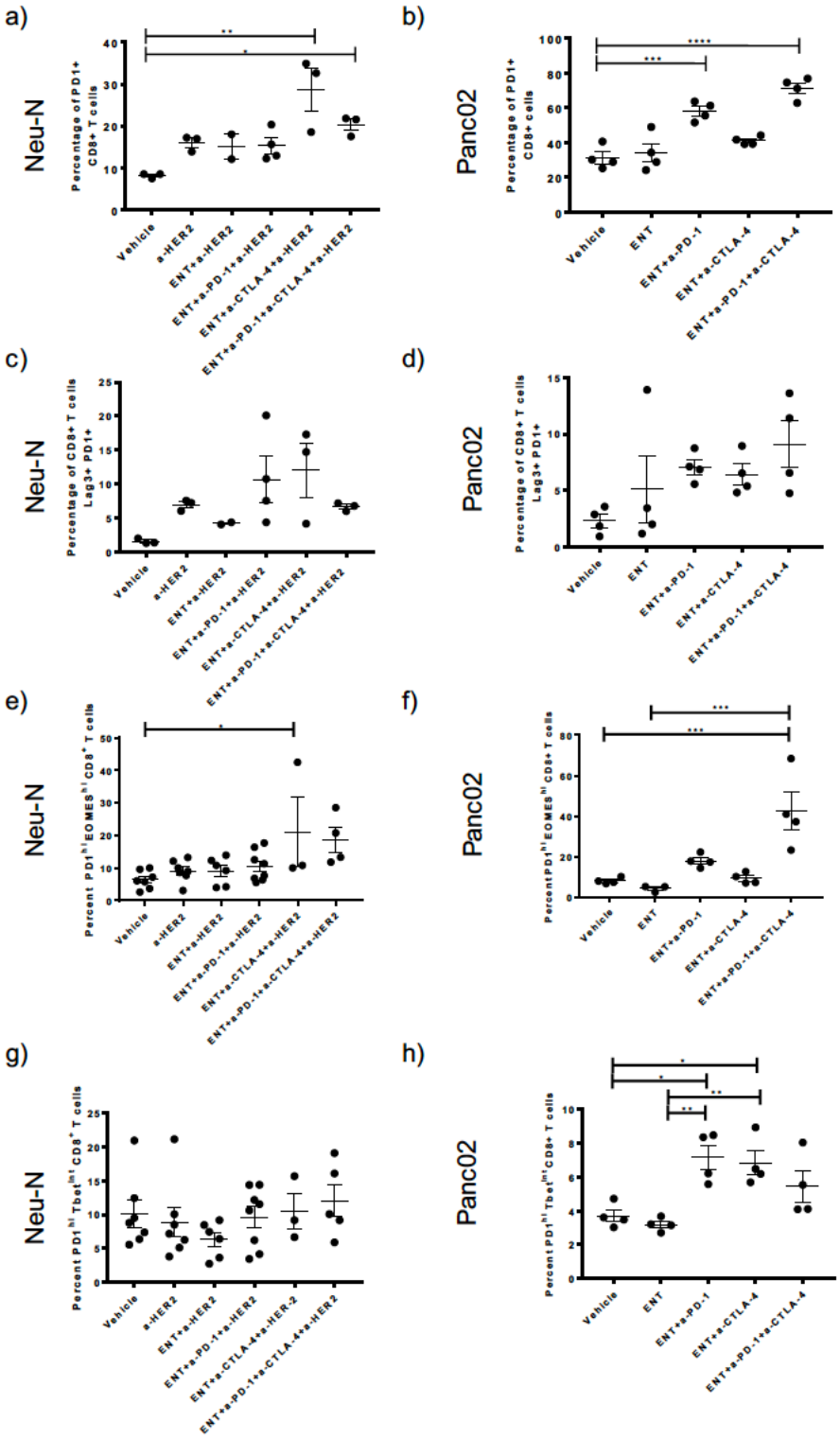

Figure 6

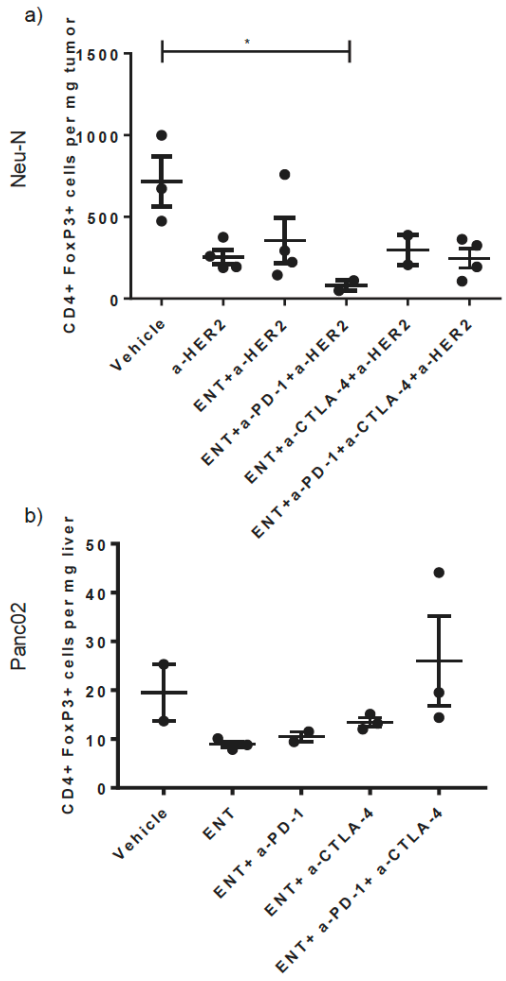

Figure 6: HDACi+ICI combination therapy does not cause reduction in T_{reg} infiltration. Changes in T_{reg} infiltration in breast tumors of **(a)** neu-N mice and **(b)** hepatic metastases of PDAC mice receiving therapy. Cells were isolated from breast tumors and livers containing PDAC metastases, respectively. For all flow data, mice were sacrificed during the third week of treatment. Each dot represents one mouse and each bar represents mean ± SEM. (n = 3-5 mice/group). Significance was determined by a one-way ANOVA with Tukey's multiple comparisons test. All experiments were repeated at least 3 times. Statistically significant p values are abbreviated as follows: *p<0.05, **p<0.01, ***p<0.001, ****p<0.0001.

ENT + ICIs significantly alters gene expression profiles in immune signaling pathways

Our data showed that ENT broadly impacted multiple populations of immune cells within the TME. Thus, we performed general immune transcriptome profiling on whole tumors isolated from the neu-N model using a PanCancer immune-profiling gene panel for the NanoString platform. Numerous significant changes were found in multiple genes and pathways (Fig. 7a). Specifically, two pathways were found to be significantly altered (listed in the table in Fig. 7b). We only report treatment combinations that showed significant changes. One of these pathways, leukocyte trans-endothelial migration, was upregulated, suggesting a mechanism by which leukocytes may be able to traffic into the TME and contribute to an antitumor response in mice treated with ENT+anti–CTLA-4 (Fig. 7b). The osteoclast differentiation pathway was significantly upregulated in tumors from mice treated with ENT+anti–CTLA-4 vs. ENT alone (Fig. 7b). Many of the genes involved in this pathway were also involved in pathways that contribute to the regulation of adaptive immunity. Our experiments also identified 20 individual genes significantly altered in cells from whole tumors treated with ENT+anti–CTLA-4 and ENT+anti–CTLA-4+anti–PD-1 (Supplementary Table 2). Detailed investigation of these genes is necessary to determine how other immune compartments are being affected. Use of NanoString enables evaluation of immune cell subsets and related pathways. However, none of the immune cell subsets were significantly altered in this evaluation. Fig. 7c demonstrates an increase in gene expression profiles that suggest both “T cells” (determined by expression of *Cd3g* and *Cd3d*) and “exhausted CD8” (determined by expression of *Lag3*) showed a trending increase in treated groups, corroborating findings from flow cytometry (Fig. 5). QC plots depicting the correlations of the genes used to call these cell types are included in Supplementary Fig. S2b, S2c. Platforms for more directed

approaches to investigation of gene expression profiling are still evolving and can be limited in feasibility by large cohort animal studies, as seen with our findings using the NanoString platform. Future studies will evaluate gene expression at the single-cell level in an effort to work around the inherent biological variability associated with animal studies.

Figure 7: HDACi+ICI combination therapy significantly alters the leukocyte transendothelial migration pathway. (a) Heatmap of gene expression changes comparing all treatment groups using the PanCancer Immune profiling gene set. Red indicates upregulation and blue indicates downregulation. **(b)** Table of significantly altered KEGG pathways. 5 most differentially expressed genes listed in last column. **(c)** Graphs depicting an increase in genes indicative of bulk T cells and exhausted T cells in combination treated groups. Genes upregulated listed in red, and genes downregulated are in blue. Expression of genes listed in white boxes were measured but did not show any fold change. Expression of genes in gray boxes were not measured by the assay. **(d)** Diagram showing proposed mechanism regulating decreased suppressive function of myeloid cells and increased infiltration of T cells as a result of treatment with ENT, anti–PD-1, and anti–CTLA-4. NanoString gene expression profiling was performed once with at least 4 mice per group. Statistically significant p values are abbreviated as follows: *$p<0.05$, **$p<0.01$, ***$p<0.001$, ****$p<0.0001$.

Figure 7

a) PanCancer Immune Panel of whole tumor

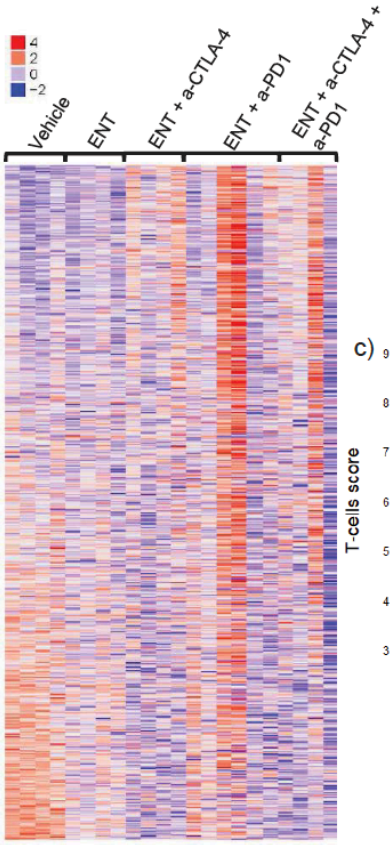

b) Pathways Upregulated

Treatment	KEGG Pathway	P-value	Most differentially expressed genes
ENT_vs_ENT + CTLA4	Leukocyte transendothelial migration	0.0383	Cdh5 ,Cxcr4, Nox2, Icam1, Itga4
	Osteoclast differentiation	0.0443	Btk, Chuk, Socs3, Socs1, Creb1

c)

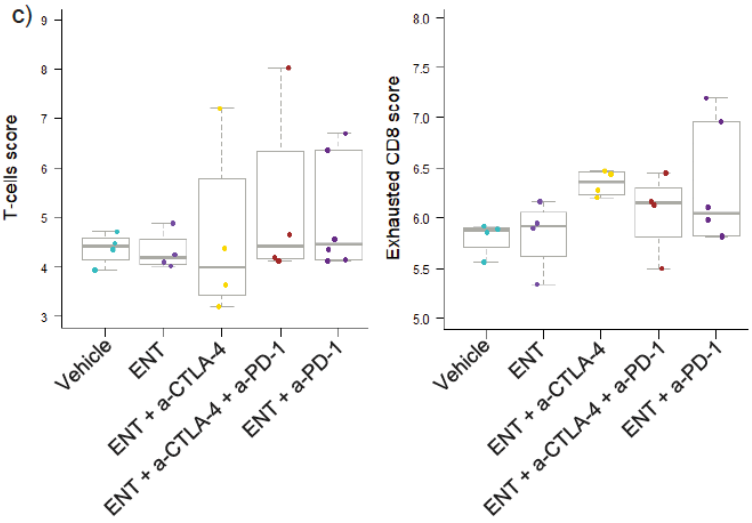

d)

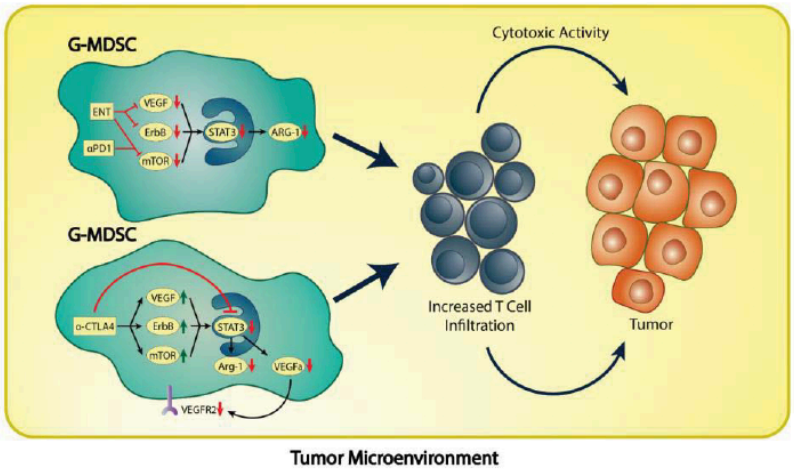

Supplementary Table 2

Treatment	Gene differentially regulated	Up or down regulated	P-value	Function
Vehicle vs. ENT+a-CTLA-4	Lamp3	down	0.0492	On mature DCs aids in identification and processing of Ag.
	C8a	down	0.0492	Part of membrane attack complex aids in forming pores in the plasma membrane of target cells
	Klra6	down	0.0367	On NK cells and inhibits their activation
	Klrb1	down	0.0367	On NK cells and regulates function
	CD160	down	0.0367	On NK cells and CD8+ T cells, potentially targetable checkpoint
Vehicle vs. ENT+a-CTLA-4+a-PD-1	Ctsw	down	0.0164	Mainly restricted to CD8+ T cells and NK cell compartments, affects but is not required for cytotoxic lymphocyte induced target cell death.
	Itgb3	down	0.0186	Integrin found on thrombocytes involved in cell adhesion and cell surface mediated signaling.
	St6gal1	down	0.0222	Found on endothelial cells of mesenteric lymph node & Peyer's patches could be involved in B cell homing to patches. Protein involved in the generation of the cell-surface carbohydrate determinants & differentiation antigens HB-6, CDw75, and CD76
	Mpped1	down	0.0222	Regulation of inflammatory processes
	Mavs	down	0.0476	Found in Tregs and required for activation of transcription factors which regulate expression of beta interferon and contributes to antiviral immunity
	IL34	down	0.0415	Ligand for CSF1 and known to play a role in growth and development of myeloid cells
	Ambp	up	0.0222	Induces neutrophil chemotaxis and adhesion
	S100a8	up	0.0363	Stimulates metastasis in neoplastic mammary epithelial cells
	Tnfrsf11a	up	0.0415	Induction in innate immune response against DNA and RNA viruses
	Kit	up	0.0508	Inhibits inflammatory cytokines; bind and inactivates MMP9
	A2m	up	0.0508	Activates IL-1 beta and IL-18
	Casp1	up	0.0363	Plays a central role in cell immunity as an inflammatory response initiator through activation of IL-1 beta and IL-18
	Klra2	up	0.0415	NK cell differentiation; inhibitory signal on NK cells that binds MHCI
	CCL3/MIP-1a	up	0.0508	Recruits PMNs
	Csf3r/ G-CSF-R	up	0.0508	Initiates cell proliferation and differentiation into mature neutrophilic granulocytes and macrophages

Supplementary Table 2: HDACi + ICI combined therapy significantly alter gene expression of genes involved in innate and adaptive immunity. Table of all genes significantly altered in whole tumors isolated from neu-N mice following listed treatment.

Discussion

We demonstrated in the neu-N and PDAC models that mice treated with the combination of ENT+ICIs exhibited significantly improved survival compared to mice treated with either ENT or ICIs alone. We also showed that the efficacy of ENT+anti–CTLA-4 treatment was associated with a significant increase in tumor-infiltrating G-MDSCs that exhibited impaired immunosuppressive function. We also identified changes in important signaling pathways that converged to control and regulate myeloid immunosuppressive activities, which suggest novel mechanisms responsible for the observed MDSC dysfunction in tumors. ENT was primarily responsible for significantly affecting genes controlling myeloid function, such as those within the VEGF and ErbB pathways, and may have also acted to prime $CD8^+$ T cells by increasing their expression of PD-1. The addition of anti–PD-1 further augmented these changes, resulting in altered signaling in the mTOR pathway. The combination of ENT+anti–CTLA-4 induced changes in expression of downstream signaling molecules, at which the three pathways converged, leading to a similar outcome on myeloid suppression. These data showed that it was the addition of ICIs to ENT that led to improved infiltration of activated $CD8^+$ T effector cells and increased cytotoxic characteristics. Examination of gene expression changes in whole tumors revealed that addition of anti–PD-1 and/or anti–CTLA-4 affected T-cell trafficking. Taken together, these data elucidate a suggested mechanism by which ENT alters the function of myeloid cells and the addition of ICIs to ENT further alters the myeloid compartment and improves T-cell responses. This mechanistic understanding delineates the important effects of each individual drug on specific immune compartments within the TME. These data could be used for developing scientifically driven combinations of epigenetic- and immune-based therapies.

Various studies have shown that ENT can reduce tumor burden and alter MDSC infiltration, facilitating increased efficacy of single agent ICIs in other murine models of cancer (29–31,51,52). These data support the therapeutic strategy of using agents that target multiple immune compartments within the TME, where ENT inhibits the immunosuppressive myeloid populations and ICIs allow for the activation and recruitment of T cells in order to induce a robust antitumor response. We showed that whereas ENT+anti–PD-1+anti–CTLA-4 was efficacious, it did not significantly improve survival over ENT+anti–PD-1 or ENT+anti–CTLA-4. A previously proposed mechanism for improved survival is that addition of ENT to anti–PD-1 leads to decreased immunosuppressive capacity of tumor-infiltrating MDSCs and allows for increased infiltration of cytotoxic T cells (30). We not only confirmed these findings in breast and PDAC models but also expanded upon them by showing a decrease in Arg-1 protein activity and production (30). Given that our data were generated entirely *ex vivo*, it supports changes in Arg-1 protein production as a significant mechanism underlying the MDSC impairment reported. In further support of this proposed mechanism, our gene expression profiling of isolated G-MDSCs allowed us to identify changes specific to the G-MDSC transcriptome in key signaling pathways such as VEGF, mTOR, and ErbB. Changes in Arg-1 and PD-L1 protein expression have not been analyzed in human MDSCs treated with ENT. However, a clinical trial has analyzed changes in MDSC populations as well as changes in CD40. CD40 has previously been described to be necessary in human MDSC-mediated T-cell suppression (65). Tomita et al. show that treatment of breast cancer patients with ENT significantly decreases CD40 expression (32), suggesting ENT may also induce immunosuppressive dysfunction in human MDSCs.

The most impactful finding of our work is the identification of changes in gene expression responsible for the impaired immunosuppressive functions of G-MDSCs that are driven by ENT. First, we observed downregulation of genes within the VEGF signaling pathway in isolated G-MDSCs in ENT or ENT+anti–PD-1–treated versus vehicle-treated mice. Previous studies showed that elimination of VEGF can abrogate Arg-1 protein expression in intratumoral MDSCs and subsequently their ability to suppress T-cell proliferation (66), highlighting the importance of VEGF signaling in immunosuppressive functions of MDSCs. Second, decreased expression of genes in the ErbB signaling pathway were seen in isolated G-MDSCs with ENT or ENT+anti–PD-1 treatment. This may also contribute to the decrease in suppressive nature of these cells because EGFR-deficient macrophages are known to produce less immunosuppressive factors, including Arg-1 (67). Taken together, ENT appears to be the treatment driving these observed changes, indicating that it may be inducing MDSC dysfunction by decreasing signaling within both pathways (Fig. 7d). Third, treatment with ENT+anti–PD-1 significantly decreased expression of genes within the mTOR pathway. It has previously been shown that inhibition of mTORC1 can disrupt the immunosuppressive abilities of myeloid cells, including Arg-1 protein expression (68,69). Therefore, it is possible that PD-1 inhibition also contributes to the observed MDSC dysfunction through decreased mTOR signaling (Fig. 7d). We evaluated protein expression of representative proteins for each pathway in order to attempt to validate the observed changes in gene expression of each pathway. Although some of these observed gene expression changes correlated with similar changes in protein expression, others did not. This was expected given that post-transcriptional modifications often cause discrepancies between levels of mRNA and protein. The reported changes in overall pathways were not determined by

changes in expression of single genes, rather the cumulative change of all genes in the pathway. Thus, expression of individual genes within a pathway were not representative of the overall reported pathway changes. Key genes directly affecting MDSC function will need to be identified before further protein analysis is pursued.

Gene expression within the mTOR, ErbB, and VEGF pathways were upregulated with ENT+anti–CTLA-4 treatment, although this treatment also inhibited MDSC function similar to the combination of ENT+anti–PD-1. We hypothesize that these differential gene expression changes across treatment groups may converge at the transcription factor *Stat3*, which is downstream of all of the pathways we have mentioned (67,70). STAT3 is known to be essential in MDSC immunosuppressive function (27) and has previously been shown to be specifically targeted by ENT in MDSCs in *in vitro* systems (24,30,71,72). G-MDSCs from mice treated with ENT+anti–CTLA-4 showed a significant decrease in *Stat3* expression, whereas significant downregulation in upstream activators were observed in the ENT or ENT+anti–PD-1 treated groups. This suggests that the ultimate change in regulation of *Stat3* occurs either directly or indirectly depending on ICI treatment but leads to the same effect on G-MDSC function. The ENT+anti–CTLA-4 treated mice also exhibited a significant decrease in the expression of *Vegfa*, which has been shown to be a target of STAT3 transcriptional activity (73–75). Despite the increase in signaling intermediates in this pathway, a decrease in *Vegfa* expression, and subsequent VEGFR2 signaling, could be caused by less STAT3 activity. This could help explain the observed MDSC dysfunction with ENT+anti–CTLA-4, as inhibition of VEGFA signaling can prevent Arg-1 production (Fig. 7d) (66). G-MDSCs from ENT+anti–CTLA-4 treated mice did show lower expression of *Arg1* compared to the mice receiving ENT+anti–PD-1, further indicating that inhibition of STAT3 signaling

may be one of the driving mechanisms in the observed MDSC dysfunction. Taken together, we hypothesize that the mTOR, ErbB, and VEGF signaling pathways converge at *Stat3* to drive immunosuppressive functions of MDSCs. This hypothesis requires significantly more investigation but given previous studies linking treatment with ENT to STAT3 activity (30) and linking STAT3 to the suppressive function of Arg-1 (27), this seems like a plausible explanation for our observations. Analysis of protein expression of STAT3 from neu-N mouse model did not follow the same trends as those observed at the mRNA level. However, investigation of phospho-STAT3 in isolated G-MDSCs showed a decrease in STAT3 phosphorylation in all treatment groups compared to vehicle, indicating decreased STAT3 activity may play a role in the observed MDSC dysfunction in treated animals. It has been shown that HDAC2 is important in the regulation of inflammatory genes in myeloid cells (54), suggesting class I HDACs may play a role in the regulation of Arg-1 (53). Lastly, it should be noted that preliminary work using the HDAC6 inhibitor ACY-1215 did not improve survival when combined with immunotherapy, suggesting class II HDACs may not play a pivotal role in the functional capabilities of MDSCs. This is an area where future studies can aim to delineate the roles of class I and II HDACs in MDSC function as well as *Stat3* regulation.

Whereas modulation of MDSC function seemed primarily responsible for the improved survival observed with ENT+ICIs in these models, the addition of ICIs also significantly improved the infiltration and cytotoxic ability of $CD8^+$ T effector cells within the TME. We identified significant upregulation of the leukocyte trans-endothelial migration pathway, which likely aids in the infiltration of TILs, and the addition of anti–CTLA-4 to ENT droves this observed change. The 20 genes that were found to be significantly affected by treatment with ENT+anti–CTLA-4 seemed to be expressed in a

wide range of immune cell types. This suggests cell types, such as dendritic cells and natural killer cells, may also be secondarily affected by ICIs but are not primarily responsible for improved survival in response to treatments in these tumor models. The observed increase in infiltration of activated T cells may also be explained by the induction of expression of immunogenic non-coding long terminal repeats (LTRs) in tumor cells. A study by Brocks et al. shows that treatment with both a DMNTi and an HDACi leads to activation of these LTR elements (76). In the future, we will examine whether treatment with ENT without DNMTi can induce a biologically relevant amount of LTR expression *in vivo*.

In summary, these data support the use of ENT as a method of sensitizing non-immunogenic tumors to ICI therapy. ENT primed the MDSC compartment of the TME to permit T-cell infiltration into tumors thereby making them available for activation by ICI therapy. ICI therapy may also contribute to reprogramming MDSCs in favor of T-cell activity. These data have provided a deeper understanding of how to improve response to ICIs in patients with breast and pancreatic cancers. Specifically, they are informing the laboratory correlates for our clinical trials evaluating ENT+combined ICIs in advanced solid tumors with a dose expansion in advanced breast cancer (NCT02453620), as well as ENT+nivolumab in patients with unresectable PDAC (NCT03250273). The preclinical work presented here will provide the necessary scientific evidence to create rational combinations of immune therapies in future clinical trials in order to maximize efficacy of these promising treatments.

CHAPTER 2: Validating the J774M cell line to determine the role of STAT3 in entinostat-induced MDSC reprogramming

Summary

In order to further investigate the role of STAT3 in MDSC immunosuppressive dysfunction, we validated the previously described MDSC-like qualities of the J774M cell line. Identification and validation of an *in vitro* model for MDSC suppression is essential for downstream molecular analysis of MDSC function, as isolated intratumoral MDSCs are often fragile and difficult to culture. We found ENT inhibits immunosuppressive function and STAT3 phosphorylation in a manner that is similar to our previous observations in our *in vivo* studies. Specifically, we showed that the J774M cell line expresses surface markers similar to intratumoral MDSCs. Additionally, we demonstrated J774M cells were capable of producing functional Arg-1 and could suppress T cell proliferation in a dose-dependent manner. Similar to intratumoral MDSCs, both of these immunosuppressive functions could be inhibited with ENT treatment. We also found that ENT treatment inhibits STAT3 phosphorylation in J774M cells, which we have observed in isolated intratumoral G-MDSCs treated with ENT and ICI combinations in models of pancreatic and breast cancer. Taken together, these data suggest that the J774M cell line is an appropriate model to use for further evaluation of the role of STAT3 in MDSC biology as well as in the context of ENT-induced MDSC immunosuppressive dysfunction.

Introduction

We and others have shown that inhibition of class I HDACs can impair the immunosuppressive functions of MDSCs in the TME and improve efficacy of ICIs in murine models. These studies have shown that use of the HDACi ENT can result in the inhibition of MDSC suppression of T cell proliferation *ex vivo* (30,77). These data show that ENT treatment of MDSCs decreases the expression of key immunosuppressive factors, such as Arg-1, PD-L1, iNOS, and COX2 (78). While the exact mechanism driving these functional changes still remain elusive, our work has identified STAT3 as a potential target of ENT, where ENT treatment causes a decrease in signaling pathways regulated by STAT3 and a decrease in phospho-STAT3 expression (77). Additionally, Orillion et. al has shown that ENT treatment of MDSCs increases acetylation of lysine on immunoprecipitated STAT3 (30), which has previously shown to inhibit STAT3 phosphorylation and activity (31). Indeed, it has previously been shown that STAT3 is an important driver of MDSC proliferation and function (24,79). Various works have shown that STAT3 activity is essential for the induction of MDSCs (25,26) and inhibiting STAT3 ablates the immunosuppressive function of MDSCs (27,28) . Specifically, it has been shown that STAT3 phosphorylation is directly associated with Arg-1 activity in MDSCs and inhibition of STAT3 can prevent MDSC suppression of T cell proliferation (27).

Given the effects of ENT treatment on post-translational modifications of STAT3 as well as the similar functional impact of ENT treatment and STAT3 inhibition on MDSCs, we reasoned that ENT may be altering the ability of STAT3 to bind the promoters of key immunosuppressive genes. In order to investigate this, we developed an *ex vivo* intratumoral MDSC system and validated the MDSC-like cell line J774M to

perform chromatin-immunoprecipitation-sequencing (ChIP-Seq) and evaluate changes in localization of phospho-STAT3 to the promoters of immunosuppressive genes in ENT-treated MDSCs. We confirm a decrease in phospho-STAT3 with ENT treatment in both the neuN and Panc02 murine models of breast and pancreatic cancer, respectively. Additionally, we show that ENT can inhibit the ability of J774M cells to produce Arg-1 and suppress T cell proliferation, which is correlated with a decrease in phospho-STAT3 levels. Taken together, these data validate the J774M cell line as a model of MDSC suppression and further supports the role of STAT3 in ENT-mediated MDSC reprogramming. This is an essential step in determining the molecular mechanisms behind altered MDSC function, as the fragility and short *ex vivo* life span of intratumoral MDSCs make robust molecular studies very difficult.

Materials and Methods

Mice and cell lines

All animal studies were approved by Institutional Review Board of Johns Hopkins University. Animals were kept in pathogen-free conditions and were treated in accordance with institutional and American Association of Laboratory Animal Committee policies. The neu-N mice were originally from W. Muller McMaster University, Hamilton, Ontario, Canada. Colonies were renewed yearly from Jackson labs and bred in house by brother/sister mating. For studies of metastatic pancreatic cancer, we used male C57BL/6J (The Jackson Laboratories, stock #000664) mice. For co-culture experiments with J774M cells, female Balb/c mice (The Jackson Laboratories, stock #000651) were used.

All cell lines were regularly tested for Mycoplasma every three months in accordance to laboratory policy. NT2.5 cells were derived from spontaneous mammary tumors growing in female neu-N mice. *In vitro* cell lines were established and authenticated as previously described (39,40). Culture conditions for NT2.5 cells were as follows: 37°C, 5% CO_2 in RPMI 1640 (Gibco, cat. 11875-093) supplemented with 20% fetal bovine serum (Gemini, cat. 100-106), 1.2% HEPES buffer (Gibco, cat. 15630-080), 1% L-glutamine (Gibco, cat. 25030-081), 1% MEM non-essential amino acids (Gibco, cat. 11140-050), 0.5% penicillin streptomycin (Gibco, cat. 15140-122), 1% sodium pyruvate (Sigma, cat. S8636), 0.2% insulin (NovoLog, cat. U-100), 0.02% gentamicin (Sigma, cat. G1397). Panc02 is a murine pancreatic tumor cell line with ductal morphology derived from a methylcholanthrene-treated C57B1/6 mouse and authenticated as previously described (41,42). Culture conditions for Panc02 cells were as follows: 37°C, 10% CO_2 in DMEM (Gibco, cat. 11965-084) supplemented with 10% fetal bovine serum (Gemini, cat. 100-

106), 1% L-glutamine (Gibco, cat. 25030-081), 0.5% penicillin streptomycin (Gibco, cat. 15140-122).

J774M is an MDSC-like cell line was developed by FACS sorting $CD11b^+$ $Gr1^+$ cells from the ATCC macrophage line J774A.1 and have previously been shown to exhibit immunosuppressive functions similar to MDSCs (30,80,81). Culture conditions for J774M cells were as follows: 37°C, 5% CO_2 in RPMI 1640 (Gibco, cat. 11875-093) supplemented with 10% fetal bovine serum (Gemini, cat. 100-106), 1.5% HEPES buffer (Gibco, cat. 15630-080), 1% L-glutamine (Gibco, cat. 25030-081), 1% MEM non-essential amino acids (Gibco, cat. 11140-050), 1% penicillin streptomycin (Gibco, cat. 15140-122), 1% sodium pyruvate (Sigma, cat. S8636), 0.0004% beta-mercaptoethanol (Sigma, cat. M3148).

Neu-N ex vivo studies

The neu-N model is a syngeneic model whereby NT2.5 cells that were derived from a spontaneous mammary tumor are implanted via injection of 5 x 10^4 cells into the mammary fat pad of 7-8 week old female neu-N mice (39).

Tumor dissociation

To obtain single-cell suspensions from breast tumors, tumors were harvested, weighed, diced, and then dissociated using a tumor dissociation kit (Miltenyi Biotec, cat. 130-096-730) and the OctoDissociator (Miltenyi Biotec) per the manufacturer's instructions. The 37C_m_TDK_2 program was used to dissociate tumors per the manufacturer's instructions. Samples were filtered using a 40 μm cell strainer and red blood cells were lysed using ACK lysis buffer (Quality Biological, cat. 118-156-721). The resulting

single-cell suspensions were used for subsequent isolation of specific immune cell types or flow cytometry as described below. Blood from neu-N mice was obtained via retro-orbital bleeds as per protocol. Red blood cells were lysed using ACK lysis buffer (Quality Biological, cat. 118-156-721). Isolated cells were analyzed via flow cytometry. To obtain single-cell suspensions of livers containing metastases in the PDAC model, livers were harvested and processed by mashing the liver through 100 μm and 40 μm cell strainers as previously described (50). Red blood cells were lysed using ACK lysis buffer (Quality Biological, cat. 118-156-721) and liver pellets were resuspended in 40% Percoll (GE Healthcare Life Sciences, cat. 17-0891-01) and underlayed with 80% Percoll. The immune cell layer was then removed and analyzed via flow cytometry.

Immune cell isolation

G-MDSCs were isolated from single-cell suspensions from tumors following tumor dissociation using Miltenyi Biotec's Myeloid-Derived Suppressor Cell Isolation Kit (cat. 130-094-538) according to the manufacturer's protocol. $Ly6G^+$ cells were positively selected to isolate G-MDSCs from $Ly6G^-$ M-MDSCs and were passed through LS columns (Miltenyi Biotec, cat. 130-042-401) twice to increase purity. Eluted G-MDSCs were then used for downstream assays described below. $CD8^+$ T cells were negatively isolated from spleens of Balb/c mice above by mashing spleens through 100 μm cell strainers. Red blood cells were lysed using ACK lysis buffer (Quality Biological, cat. 118-156-721), and $CD8^+$ T cells were isolated from spleen pellets using the EasySep Mouse $CD8^+$ Isolation Kit (StemCell, cat. 19853) per the manufacturer's instructions. $CD8^+$ T cells were then used for the *in vitro* suppression assay described below.

Flow cytometry

Isolated single-cell suspensions were washed and then incubated for 30 minutes with Live/Dead Near-IR (ThermoFisher, cat. L10119) according to the manufacturer's protocol, followed by a 30-minute incubation with the appropriate flow cytometry antibodies. Samples were run on a CytoFLEX (Beckman Coulter) cytometer and analyzed using FlowJo (FlowJo LLC).

Ex vivo G-MDSC culturing

For *ex vivo* experiments using intratumoral G-MDSCs, G-MDSCs were plated in tumor conditioned media after being isolated as described above. Tumor conditioned media is derived by culturing NT2.5 for 48 hours in the NT2.5 media described above and subsequent filtering to remove tumor cells.

Arginase assay

Arginase activity was measured colorimetrically using Abcam's Arginase Activity Assay Kit (cat. ab180877). For *ex vivo* studies, G-MDSCs were isolated from tumors, plated in tumor conditioned media with ENT or DMSO vehicle for 16 hours, and subsequently harvested. For *in vitro* studies, J774M were cultured with ENT or DMSO vehicle for 16 hours and subsequently harvested. In short, cells were lysed with the kit's lysis buffer at $1x10^6$/1mL, and plated (500k cells per well) in duplicate in a flat-bottom, low-retention plate carefully to avoid bubble formation. Target samples were incubated for 20 minutes at 37°C with H_2O_2 substrate solution, while background wells were incubated with additional buffer. Standards were prepared per kit instructions, and the enzymatic reaction mixture was prepared and added to all wells. Raw absorbance values were

immediately obtained over a 30-minute period using a plate reader (Molecular Devices SpectraMax M3) at OD=570nm at 37°C. Arginase Activity Units were then calculated from raw absorbance values. ΔOD (ΔOD= (OD2-ODbg2)-(OD1-ODbg1)) was used to obtain the nmol of H_2O_2 generated by arginase, collected from a standard curve of known H_2O_2 concentrations. Arginase activity is calculated as (B/ΔT*V)*D in units/mL, where B is amount of H_2O_2 from standard curve (nmol), V is the sample volume added into reaction well (μL), D is sample dilution factor. One unit of Arginase activity refers to the amount of arginase that will generate 1.0 nmol of H_2O_2 per minute at pH 8 at 37°C.

In vitro suppression assay

J774M cells treated with ENT or DMSO vehicle for 16 hours were co-cultured with stimulated T cells. T cell proliferation was measured via CFSE dilution. T cells were isolated from spleens of Balb/c mice as described above and subsequently labeled with CFSE (ThermoFisher, cat. C34554) per the manufacturer's insstructions. 2.5 x10^5 CSFE-labeled $CD8^+$ T cells were cultured with J774M cells at varying ratios (1:1 – 1:8 J774M:T cells) and anti-CD3/CD28 beads (ThermoFisher, cat. 11453D) at a bead-to-T cell ratio of 1:1 per the manufacturer's instructions for T cell activation. T cells were allowed to proliferate for 52 hours. Subsequently, the cultures were harvested, stained with Live/Dead NIR (ThermoFisher, cat. L10119) as well as CD8 and analyzed via flow cytometric analysis as described above. Dilutions of initial CFSE were indications of T cell divisions, where fewer divisions indicated greater suppressive activity. All antibodies used are listed in Supplementary Table 1.

PDAC hemi-splenectomy in vivo studies

To study metastatic PDAC, we used a hemi-splenectomy model using 7-8 week old syngeneic male C57BL/6J. This involved giving an intrasplenic injection of $2x10^6$ of the pancreatic adenocarcinoma cell line (Panc02), as previously described (44–46). Panc02 cells were cultured from frozen stocks and passaged twice before injection. Metastases were allowed to establish for 7 days prior to starting treatment with various drug combinations as described in Chapter 1.

Western blots

For analysis of *in vivo* samples, G-MDSCs were isolated from whole tumor of treated animals using Miltenyi Biotec's MDSC Isolation Kit and pooled by treatment group. For *ex vivo* samples, G-MDSCs were isolated from untreated animals, cultured with ENT or DMSO vehicle in tumor conditioned media for 16 hours as described above, and subsequently harvested. For *in vitro* analysis, J774M cells were cultured with ENT or DMSO vehicle for 16 hours and subsequently harvested. Samples being used for phospho-STAT3 analysis were subsequently stimulated with IL-6 at 20 ng/µl for 25 minutes. Samples were lysed in RIPA buffer with added 1µM DTT, 1µM PMSF, and 1:100 protease/phosphatase inhibitor cocktail (Cell Signaling #5872S) and quantified by BCA (Pierce, #23225). Protein amounts were normalized between samples and run on a 4-12% Bis-Tris gels under denaturing conditions. The LiCor Odyssey developing and imaging system was used, and the following primary antibodies were diluted in Odyssey Blocking Buffer (TBS) + 0.2% Tween® 20 at specified concentrations: Cell Signaling Phospho-Stat3 (Tyr705) Rabbit mAb (1:2000), β-actin (13E5) Rabbit mAb (1:2000). Membranes were blocked with Odyssey blocking buffer TBS for 1hr and then incubated

with primary antibody solution overnight at 4°C with gentle shaking. Membranes were washed with 1X TBS-T and subsequently incubated with the following secondary antibodies: 800CW Donkey anti-Rabbit IgG (1:10,000) in Odyssey Blocking Buffer (TBS) + 0.2% Tween® 20. Membranes were protected from light during incubation with secondary mixture for one hour at room temperature with gentle shaking. Membranes were subsequently washed with 1X TBS-T and imaged with the Odyssey® imaging system. Images were analyzed using ImageJ.

Statistical analyses

For bar graphs, each dot represents a biological replicates and each bar represents mean ± SEM. (n = 2-3 replicates/group). For Western blot and arginase activity data, significance was determined by a one-way ANOVA with Tukey's multiple comparisons test. All experiments were repeated at least 3 times. For immunosuppression data, significance was determined by a two-way ANOVA with Dunnett's multiple comparison's test. All statistical analysis listed here were performed using GraphPad Prism v7.00. Statistically significant p values are abbreviated as follows: *$p<0.05$, **$p<0.01$, ***$p<0.001$, ****$p<0.0001$.

Results

J774M cells phenotypically resemble intratumoral MDSCs

We hypothesized that ENT could be reprogramming MDSCs by altering STAT3 activity and subsequent expression of key immunosuppressive genes regulated by STAT3. In order to perform the ChIP-Seq experiment to evaluate this hypothesis, we aimed to validate the J774M cell line (kindly provided by Dr. Kebin Liu) as a model for MDSC immunosuppression. The J774M cell line has previously been described as an MDSC-like cell line, expressing similar surface markers to those expressed by tumor-induced MDSCs in mice. These cells also express various immunosuppressive molecules, allowing them to suppress T cell proliferation in a manner similar to intratumoral MDSCs (30,80,81). We performed flow cytometric analysis and found the J774M cells to be almost exclusively CD11b+ Gr1+, as previously described (80). Additionally, we found the cells to express both of the classic murine MDSC markers Ly6C and Ly6G (Fig. 1a), showing that the surface marker expression of the J774M line resembles that of intratumoral MDSCs.

ENT inhibits Arg-1 production in both J774M cells and ex vivo G-MDSCs

Next we wanted to determine if J774M cells were capable of producing functional Arg-1, a key protein in MDSC-mediated T cell suppression, and if treatment with ENT could disrupt Arg-1 production as we observed *in vivo*. To determine this, we utilized a colorimetric assay to determine Arg-1 activity, which is defined by the conversion rate of Arg-1 substrate. These data show that J774M cells are not only capable of producing active Arg-1 protein, but treatment with ENT decreases the levels of Arg-1 production, similar to our *in vivo* observations (Fig. 2a). This in part supports the use of the J774M

line as a model of MDSC immunosuppression, as Arg-1 has previously been described as playing a key role in MDSC-mediated T cell suppression (24,30,82). Additionally, we confirm these findings in intratumoral G-MDSCs isolated from tumors of untreated neuN mice and cultured with ENT *ex vivo* (Fig. 2b). This decrease in Arg-1 production in *ex vivo* G-MDSCs treated with ENT supports the findings of our *in vivo* studies, where ENT drives MDSC dysfunction while ICIs drive T cell infiltration in combination treated animals (Ch. 1: Fig. 3a-c, Supplementary Fig. 6a-f).

Figure 1

a).

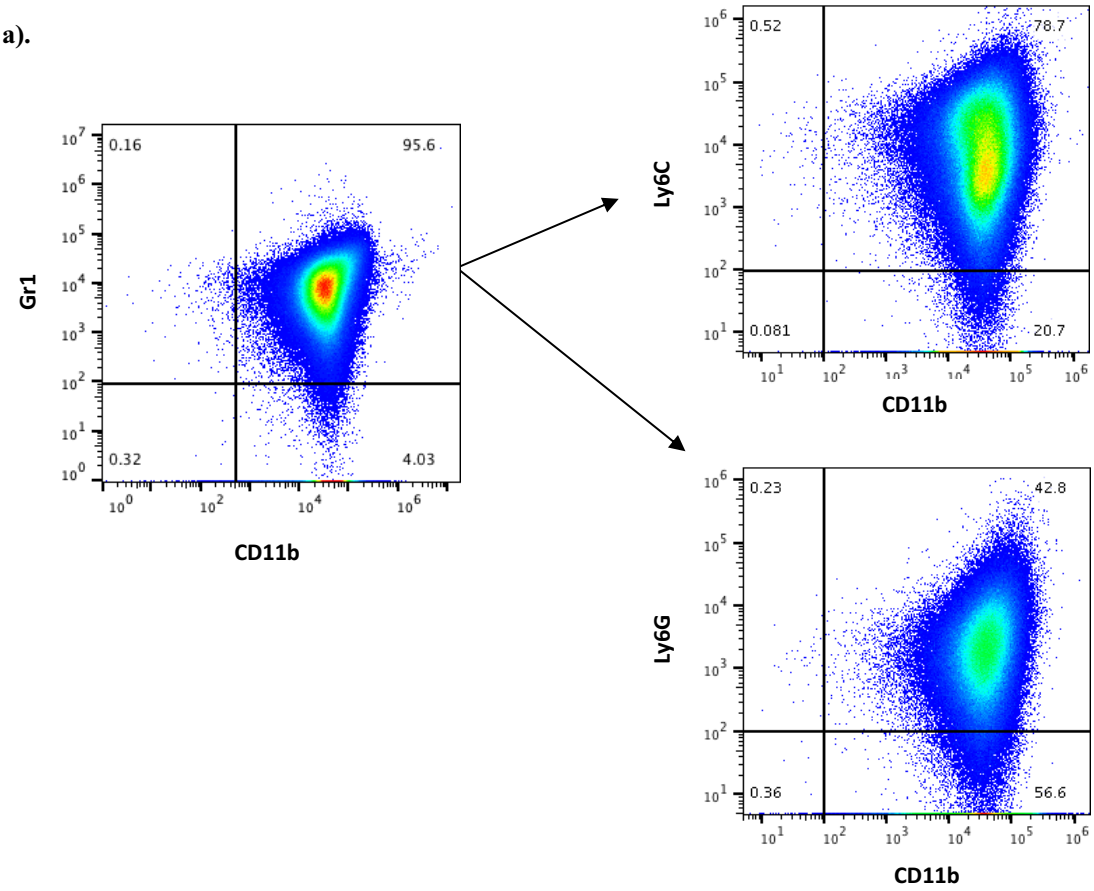

Figure 1: Flow cytometry characterization of the J774M cell line. (a) Flow staining of J774M cells for typical intratumoral MDSC markers.

Figure 2

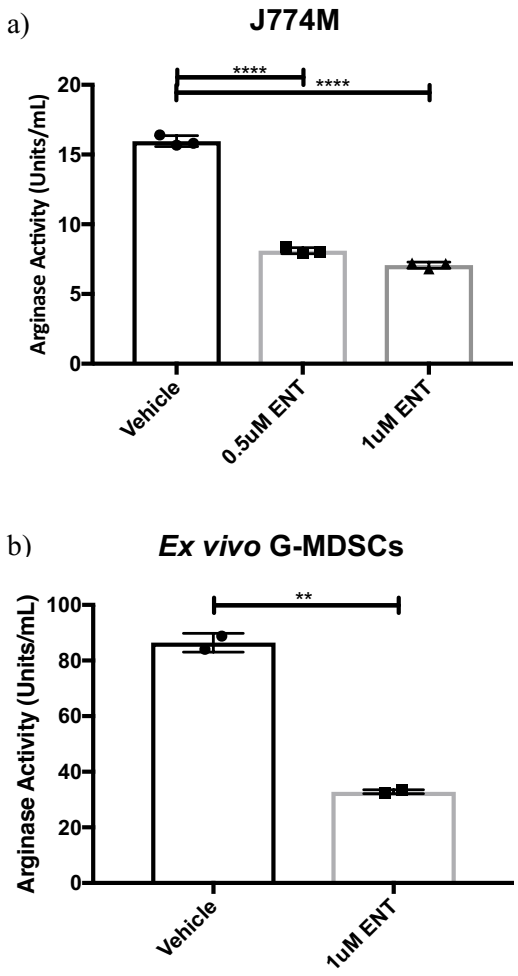

Figure 2: ENT inhibits arginase production in both J774M cells and *ex vivo* G-MDSCs. (a) J774M cells were harvested after 16 hours of treatment with ENT and arginase activity was measured. Each dot represents one biological replicate and each bar represents mean±SEM. **(b)** $Ly6G^+$ G-MDSCs were isolated from tumors of untreated neuN mice. G-MDSCs were treated with ENT *ex vivo* for 16 hours in tumor conditioned media, harvested, and arginase activity was measured. Each dot represents G-MDSCs pooled from two tumors and each bar represents mean±SEM. All experiments were repeated at least 3 times. Statistically significant p values are abbreviated as follows: **p<0.01, ****p<0.0001.

J774M immunosuppressive functions can be inhibited by ENT

Our previous *ex vivo* immunosuppression studies in neuN mice showed a significant decrease in the immunosuppressive functions of intratumoral G-MDSCs isolated from ENT-treated animals compared to G-MDSCs isolated from vehicle treated animals. Therefore, we wanted to validate that the J774M line was capable of suppressing T cell proliferation. We also wanted to determine if any observed T cell suppression could be inhibited by ENT treatment. J774M cells were pre-treated with DMSO vehicle and subsequently co-cultured with CFSE-labeled $CD8^+$ T cells isolated from Balb/c splenocytes at varying dilutions. T cells were then activated via stimulation with anti-CD3/CD28 beads. T cells were allowed to proliferate for 52 hours, harvested, and analyzed via flow cytometry. We found that J774M cells were able to suppress T cell proliferation in a dose-dependent fashion (Fig. 3a, 3b). When J774M were pre-treated with either 0.5 μM or 1 μM ENT, their ability to suppress T cell proliferation was significantly impaired compared to the DMSO vehicle control (Fig. 3a, 3b), which aligns with what we observed in intratumoral G-MDSCs isolated from ENT-treated animals. These results further support the use of the J774M line as a model for MDSC immunosuppression, as these cells not only inhibit T cell proliferation but also respond to ENT treatment in a manner similar to intratumoral MDSCs.

Figure 3

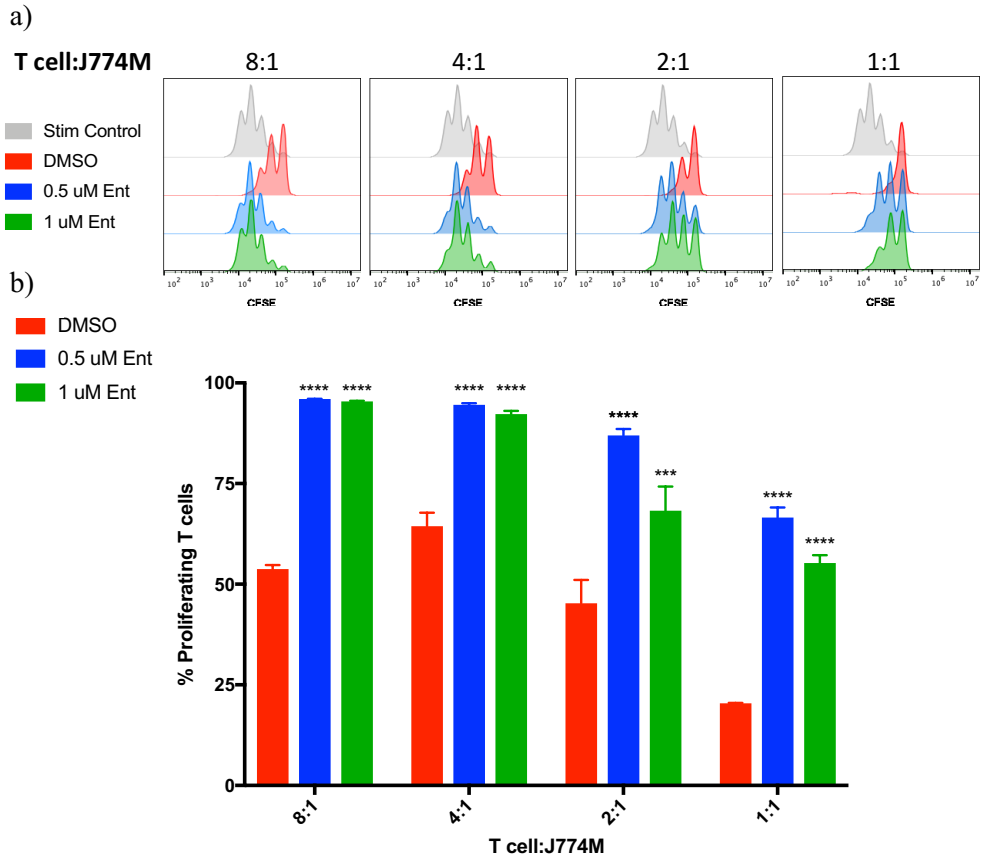

Figure 3: ENT inhibits J774M-mediated suppression of CD8$^+$ T cell proliferation. J774M cells were treated with treated with ENT for 16 hours and co-cultured with CFSE-labeled CD8$^+$ T cells isolated from spleens of Balb/c mice. Anti-CD3/CD28 beads were added to the cultures to induce T cell stimulation and T cells were allowed to proliferate for 52 hours. The "stim control" culture contained only CFSE-labeled CD8+ T cells and anti-CD3/CD28 beads. Cultures were harvested and analyzed via flow cytometry. **(a)** CFSE peaks of live CD8$^+$ T cells. Each peak represents a cell division as determined by CFSE dilution **(b)** Quantification of percentages of proliferating CD8$^+$ T cells with each treatment group compared to the DMSO control. n = 2 replicates per group. Each bar represents mean±SEM. Each experiment was repeated at least 3 times. Statistically significant p values are abbreviated as follows: ***p<0.001, ****p<0.0001.

ENT inhibits IL6-induced STAT3 phosphorylation

In our neuN *in vivo* studies, we observed a decrease in signaling of various pathways that converge at STAT3 and confirmed that IL6-induced phosphorylation of STAT3 was decreased in intratumoral G-MDSCs isolated from treated animals. This decrease in IL6-induced phosphorylation of STAT3 in ENT-treated intratumoral G-MDSCs was further confirmed in our Panc02 hemisplenectomy model (Fig. 4c). Once we determined that the ENT treatment prevented J774M cells from producing Arg-1 and suppressing T cell proliferation, we next wanted to evaluate how ENT altered IL6-induced phosphorylation of STAT3 in the J774M line. We treated J774M cells with ENT, stimulated STAT3 phosphorylation with IL6, and lysed cells. When probing the lysate for phospho-STAT3, we found a significant decrease in phospho-STAT3 in cells treated with ENT (Fig. 4a, 4b), which is comparable to what we observed in both our *in vivo* neuN and Panc02 studies (Ch. 1: Fig. 1b-d, Supplementary Fig. 4b, 4c). These data indicate that ENT alters STAT3 activity similarly in J774M cells and intratumoral G-MDSCs.

Figure 4

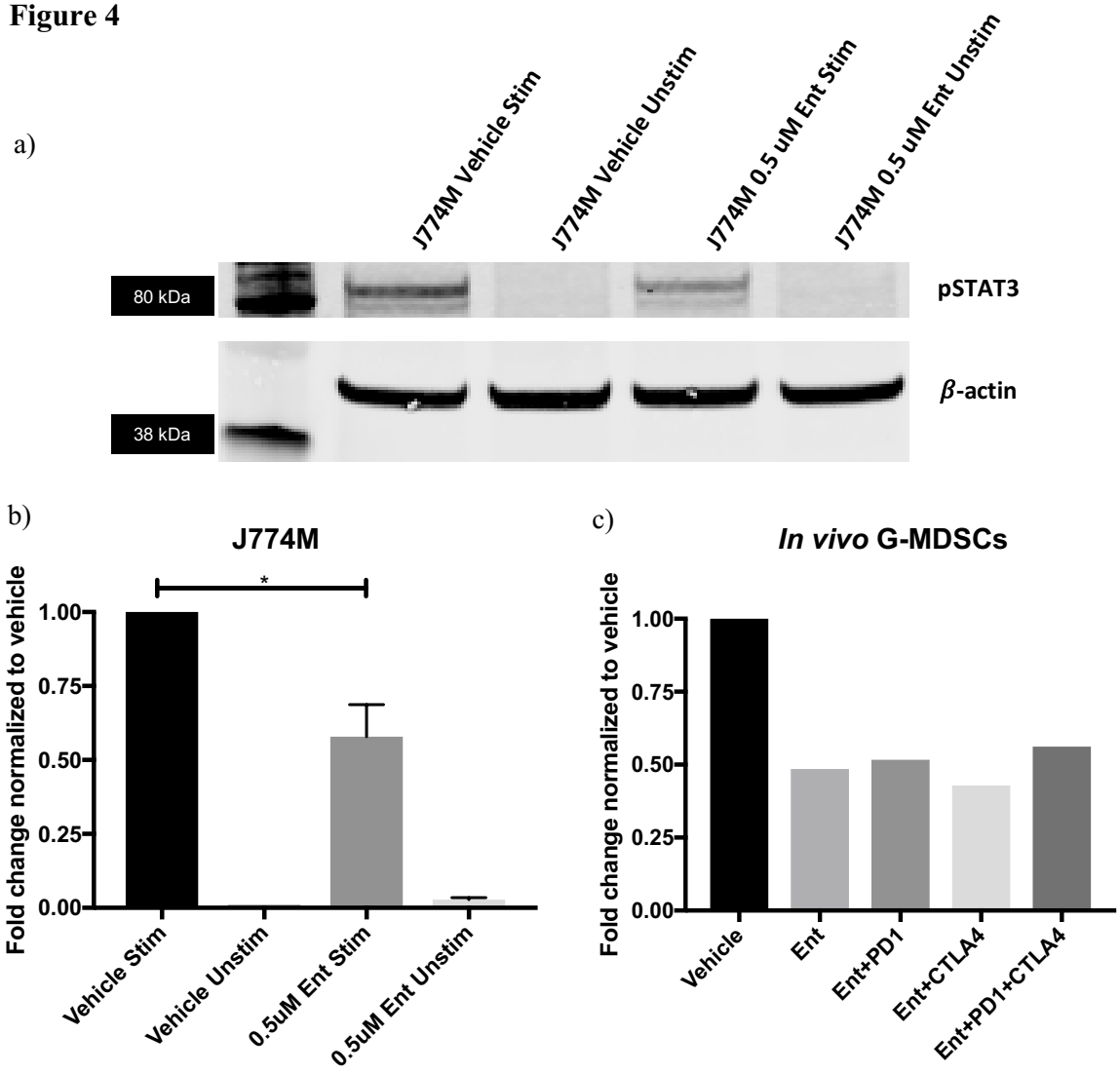

Figure 4: ENT inhibits IL6-induced phosphorylation of both J774M cells and isolated intratumoral G-MDSCs from treated Panc02 mice. J774M cells were stimulated with IL6 and lysed. **(a)** Western blot of lysates probed for phospho-STAT3 and beta-actin. **(b)** Quantification of pSTAT3 bands normalized to vehicle (n = 2 biological replicates/group). Intratumoral G-MDSCs isolated from livers of treated animals, stimulated with IL6 and lysed. **(c)** Representative quantification of pSTAT3 bands normalized to vehicle. All experiments were repeated at least twice. Statistically significant p values are abbreviated as follows: *$p<0.05$.

Discussion

We demonstrated that the surface marker expression and function of the J774M line resembles that of intraturmoral MDSCs, where J774M cells express CD11b, Gr1, Ly6G, and Ly6C as well as produce functional Arg-1 and inhibit T cell proliferation in a dose-dependent fashion. Additionally, we evaluated ENT's effect on these immunosuppressive functions and found that ENT treatment significantly impairs the ability of J774M cells to produce Arg-1 and suppress T cell proliferation. These data resemble what we have observed in both intratumoral MDSCs isolated from treated animals as well as isolated intratumoral G-MDSCs cultured and treated *ex vivo* with ENT. In our *in vivo* work, ENT-induced MDSC dysfunction was associated with a decrease in STAT3 phosphorylation. We also evaluated the effect of ENT treatment on STAT3 activity in the J774M line and found that ENT treated cells had a significant decrease in IL6-induced STAT3 phosphorylation. Taken together, these data suggest that the J774M line is a good model for studying the role STAT3 in ENT-mediated MDSC reprogramming.

Our data not only validate use of the J774M line for our future mechanistic studies, but they also confirm the work of others using this cell line to model MDSC biology. Specifically, these data support previous observations that the J774M line is capable of suppressing T cell proliferation (30,80,81). Additionally, our data are in line with the findings of Orillion et. al, which show that treatment of J774M cells with entinotat can decrease Arg-1 expression and inhibit T cell immunosuppression (30). This work also shows an increase in STAT3 acetylation when J774M cells are treated with ENT. We add to this work by showing ENT treatment of J774M cells results in a direct decrease in STAT3 phosphorylation.

These data lay the foundation for future studies to further investigate the role of STAT3 in MDSC biology and in MDSC immunosuppressive dysfunction induced by ENT. Our studies with the J774M line will focus on validating the role of STAT3 in J774M immunosuppression in addition to mechanistically understanding the effect of ENT on STAT3 promoter binding and subsequent transcriptional events. We hypothesize that ENT treatment prevents phosphorylation of STAT3 and subsequently prevents STAT3 binding to the promoters of genes essential to MDSC immunosuppressive function. We are currently working to further validate the role of STAT3 in MDSC immunosuppression using the antisense oligonucleotide STAT3 inhibitor AZD9150. By performing the same arginase production and immunosuppression assays described above with the J774M line and intratumoral MDSCs cultured *ex vivo.* We will determine if specific STAT3 inhibition results in the same immunosuppressive dysfunction that is observed with ENT treatment.

Our current work is also focused on optimizing and performing ChIP-Seq for phospho-STAT3. Our goal is to compare differences in phospho-STAT3 promoter binding between J774M cells untreated and treated with ENT. With the data obtained from this experiment, we hope to identify a number of genes that ENT treatment alters the binding of STAT3 to their promoters. Once affected genes have been identified, we will determine if knockout or knockdown of these genes in the J774M cells is sufficient to cause immunosuppressive dysfunction. Additionally, we aim to determine if ENT treatment is directly impeding transcription by performing ChIP-Seq on RNA polymerase II and evaluating changes in binding of transcriptional machinery at genes of interest. These data will not only further elucidate the role of STAT3 in MDSC biology but also identify new, more specific targets for MDSC reprogramming. Once we have identified

changes in STAT3 promoter binding in the J774M line, we will validate these changes *in vivo* by performing ChIP-PCR on intratumoral MDSCs treated with ENT. Once validated, we will knockout the selected genes in the J774M line via CRISPR and evaluate changes in immunosuppressive function via arginase activity and immunosuppression assays. This will identify the knockout lines with the greatest decrease in immunosuppressive functions. We will then adoptively transfer the most dysfunctional J774M knockout lines as well as wild-type J774M cells into the syngeneic 4T1 breast cancer model with endogenous MDSCs depleted using an anti-Gr1 antibody. We will subsequently evaluate the effect of dysfunctional J774M cells versus wild-type J774M cells on tumor growth and survival. We will further investigate how deletion of immunosuppressive genes of interest in our MDSC-like J774M line impacts immune response by evaluating changes in immune cell infiltration and function via flow cytometry.

OVERALL SUMMARY

In summary, our data demonstrated ENT sensitizes non-immunogenic breast and pancreatic tumors to ICI therapy by reprogramming intratumoral MDSCs, rendering them unable to produce immunosuppressive factors and suppress T cell proliferation. Gene profiling and immunoblot analysis suggested this dysfunction is driven by a decrease in STAT3 activity in MDSCs. We further validated this hypothesis using the MDSC-like cell line J774M, showing that ENT treatment of J774M cells inhibits their ability to generate Arg-1 and suppress T cell proliferation, which correlated with a decrease STAT3 activity.

In our murine models of breast and pancreatic cancer, we show that combining the histone deacetylase inhibitor ENT with the ICIs, anti-PD-1 and anti-CTLA-4, significantly improve survival in murine models of breast and pancreatic cancer. By utilizing flow cytometry and *ex vivo* functional assays, we found this improved survival is correlated with decreased immunosuppressive capabilities of intratumoral G-MDSCs in both models. Additionally, we demonstrated that combination therapy increases the infiltration of effector cytotoxic T cells in the TME in both models. Genetic profiling of both isolated intratumoral G-MDSCs as well as whole TIL found significant changes in immune-related pathways. Specifically, intratumoral G-MDSCs from treated animals showed changes in various signaling pathways that converge at STAT3. We confirmed a decrease in STAT3 phosphorylation in treated G-MDSCs, which suggested changes in STAT3 activity may be driving ENT reprogramming of intratumoral MDSCs.

We next validated the MDSC-like cell line J774M in order to perform mechanistic studies designed to detail how ENT treatment alters STAT3 binding activity. We found J774M cells phenotypically resemble intratumoral MDSCs via flow cytometry.

Using arginase production and T cell proliferation assays, we also found the J774M line produced similar immunosuppressive factors and suppressed T cell proliferation as observed in intratumoral MDSCs. We also show ENT inhibits these immunosuppressive qualities of the J774M line, which is correlated with a decrease in STAT3 phosphorylation. Taken together, these data show that ENT is able to inhibit MDSC immunosuppressive function and sensitize non-immunogenic breast and pancreatic cancers to ICI therapy. Furthermore, data from both intratumoral MDSCs and the MDSC-like J774M line suggest this reprogramming of MDSC function is driven by changes in STAT3 activity. Additionally, our characterization of the J774M line demonstrates it is a good model for MDSC suppression and ENT-induced MDSC dysfunction, validating the use of this cell line for our STAT3-ChIP experiment and subsequent mechanistic studies.

REFERENCES

1. Nanda R, Chow LQM, Dees EC, Berger R, Gupta S, Geva R, et al. Pembrolizumab in Patients With Advanced Triple-Negative Breast Cancer: Phase Ib KEYNOTE-012 Study. J Clin Oncol. 2016 Jul;34(21):2460–7.
2. Dirix LY, Takacs I, Jerusalem G, Nikolinakos P, Arkenau H-T, Forero-Torres A, et al. Avelumab, an anti-PD-L1 antibody, in patients with locally advanced or metastatic breast cancer: a phase 1b JAVELIN Solid Tumor study. Breast Cancer Res Treat. Springer US; 167(3).
3. Schmid P, Cruz C BF. Atezolizumab in metastatic TNBC (mTNBC): Long-term clinical outcomes and biomarker analyses. In 2017 AACR Annual Meeting. Abstract #2986; 2017.
4. Rugo HS, Delord J-P, S-a I et al. Preliminary efficacy and safety of pembrolizumab (MK-3475) in patients with PD-L1-positive, estrogen receptor-positive (ER+)/HER2 negative advanced breast cancer enrolled in KEYNOTE-028. In 2015 San Antonio Breast Cancer Symposium. Abstract S5-07; 2015.
5. Tolaney S, Savulsky C, Aktan G, Xing D, Almonte A, Karantza V, et al. Abstract P5-15-02: Phase 1b/2 study to evaluate eribulin mesylate in combination with pembrolizumab in patients with metastatic triple-negative breast cancer. Cancer Res. American Association for Cancer Research; 2017 Feb;77(4 Supplement):P5-15-02-P5-15-02.
6. Adams S, Schmid P, Rugo HS et al. Phase 2 study of pembrolizumab (pembro) monotherapy for previously treated metastatic triple-negative breast cancer (mTNBC): KEYNOTE-086 cohort A. Journal of Clinical Oncology. 35, no.

15_suppl (May 2017) 1008-1008.; 2017.

7. Adams S, Loi S, Toppmeyer D et al. Phase 2 study of pembrolizumab as first-line therapy for PD-L1–positive metastatic triple-negative breast cancer (mTNBC): Preliminary data from KEYNOTE-086 cohort B. Journal of Clinical Oncology. 35, no. 15_suppl (May 2017) 1088-1088.;
8. Brahmer JR, Tykodi SS, Chow LQM, Hwu W-J, Topalian SL, Hwu P, et al. Safety and Activity of Anti–PD-L1 Antibody in Patients with Advanced Cancer. N Engl J Med. 2012;366(26):2455–65.
9. Royal RE, Levy C, Turner K, Mathur A, Hughes M, Kammula US, et al. Phase 2 trial of single agent Ipilimumab (anti-CTLA-4) for locally advanced or metastatic pancreatic adenocarcinoma. J Immunother. 2010;33(8):828–33.
10. Skelton RA, Javed A, Zheng L, He J. Overcoming the resistance of pancreatic cancer to immune checkpoint inhibitors. J Surg Oncol. 2017;116(1):55–62.
11. Clark CE, Hingorani SR, Mick R, Combs C, Tuveson DA, Vonderheide RH. Dynamics of the immune reaction to pancreatic cancer from inception to invasion. Cancer Res. 2007;67(19):9518–27.
12. Chanmee T, Ontong P, Konno K, Itano N. Tumor-associated macrophages as major players in the tumor microenvironment. Cancers (Basel). 2014;6(3):1670–90.
13. Umansky V, Sevko A. Tumor microenvironment and myeloid-derived suppressor cells. Cancer Microenviron. 2013;6(2):169–77.
14. Bronte V, Serafini P, Mazzoni A, Segal DM, Zanovello P. L-arginine metabolism in myeloid cells controls T-lymphocyte functions. Trends Immunol. 2003;24(6):302–6.

15. Kusmartsev S, Nagaraj S, Gabrilovich DI. Tumor-associated CD8+ T cell tolerance induced by bone marrow-derived immature myeloid cells. J Immunol. 2005;175(7):4583–92.

16. Mazzoni A, Bronte V, Visintin A, Spitzer JH, Apolloni E, Serafini P, et al. Myeloid suppressor lines inhibit T cell responses by an NO-dependent mechanism. J Immunol. 2002;168(2):689–95.

17. Li H, Han Y, Guo Q, Zhang M, Cao X. Cancer-expanded myeloid-derived suppressor cells induce anergy of NK cells through membrane-bound TGF-beta 1. J Immunol. 2009;182(1):240–9.

18. Bogdan C. Regulation of lymphocytes by nitric oxide. Methods Mol Biol. 2011;677:375–93.

19. Kamran N, Kadiyala P, Saxena M, Candolfi M, Li Y, Moreno-Ayala MA, et al. Immunosuppressive Myeloid Cells' Blockade in the Glioma Microenvironment Enhances the Efficacy of Immune-Stimulatory Gene Therapy. Mol Ther. 2017;25(1):232–48.

20. Yang R, Cai Z, Zhang Y, Yutzy WH th, Roby KF, Roden RB. CD80 in immune suppression by mouse ovarian carcinoma-associated Gr-1+CD11b+ myeloid cells. Cancer Res. 2006;66(13):6807–15.

21. Marvel D, Gabrilovich DI. Myeloid-derived suppressor cells in the tumor microenvironment: expect the unexpected. J Clin Invest [Internet]. American Society for Clinical Investigation; 2015 Sep 1 [cited 2019 Feb 8];125(9):3356–64. Available from: https://www.jci.org/articles/view/80005

22. Corzo CA, Condamine T, Lu L, Cotter MJ, Youn JI, Cheng P, et al. HIF-1alpha regulates function and differentiation of myeloid-derived suppressor cells in the

tumor microenvironment. J Exp Med. 2010;207(11):2439–53.

23. Ezernitchi A V, Vaknin I, Cohen-Daniel L, Levy O, Manaster E, Halabi A, et al. TCR zeta down-regulation under chronic inflammation is mediated by myeloid suppressor cells differentially distributed between various lymphatic organs. J Immunol. 2006;177(7):4763–72.

24. Condamine T, Gabrilovich DI. Molecular mechanisms regulating myeloid-derived suppressor cell differentiation and function. Trends in Immunology Jan, 2011 p. 19–25.

25. Yu H, Liu Y, McFarland BC, Deshane JS, Hurst DR, Ponnazhagan S, et al. SOCS3 Deficiency in Myeloid Cells Promotes Tumor Development: Involvement of STAT3 Activation and Myeloid-Derived Suppressor Cells. Cancer Immunol Res [Internet]. American Association for Cancer Research; 2015 Jul 1 [cited 2019 Feb 10];3(7):727–40. Available from: http://www.ncbi.nlm.nih.gov/pubmed/25649351

26. Panni RZ, Sanford DE, Belt BA, Mitchem JB, Worley LA, Goetz BD, et al. Tumor-induced STAT3 activation in monocytic myeloid-derived suppressor cells enhances stemness and mesenchymal properties in human pancreatic cancer. Cancer Immunol Immunother [Internet]. Springer; 2014 May 21 [cited 2019 Feb 10];63(5):513–28. Available from: http://www.ncbi.nlm.nih.gov/pubmed/24652403

27. Vasquez-Dunddel D, Pan F, Zeng Q, Gorbounov M, Albesiano E, Fu J, et al. STAT3 regulates arginase-i in myeloid-derived suppressor cells from cancer patients. J Clin Invest [Internet]. American Society for Clinical Investigation; 2013 Apr [cited 2019 Feb 10];123(4):1580–9. Available from:

http://www.ncbi.nlm.nih.gov/pubmed/23454751

28. Rosborough BR, Mathews LR, Matta BM, Liu Q, Raïch-Regué D, Thomson AW, et al. Cutting edge: Flt3 ligand mediates STAT3-independent expansion but STAT3-dependent activation of myeloid-derived suppressor cells. J Immunol [Internet]. NIH Public Access; 2014 Apr 15 [cited 2019 Feb 10];192(8):3470–3. Available from: http://www.ncbi.nlm.nih.gov/pubmed/24639346

29. Kim K, Skora AD, Li Z, Liu Q, Tam AJ, Blosser RL, et al. Eradication of metastatic mouse cancers resistant to immune checkpoint blockade by suppression of myeloid-derived cells. Proc Natl Acad Sci U S A. 2014;111(32):11774–9.

30. Orillion A, Hashimoto A, Damayanti N, Shen L, Adelaiye-Ogala R, Arisa S, et al. Entinostat Neutralizes Myeloid-Derived Suppressor Cells and Enhances the Antitumor Effect of PD-1 Inhibition in Murine Models of Lung and Renal Cell Carcinoma. Clin Cancer Res [Internet]. American Association for Cancer Research; 2017 Sep 1 [cited 2018 Aug 2];23(17):5187–201. Available from: http://www.ncbi.nlm.nih.gov/pubmed/28698201

31. Shen L, Ciesielski M, Ramakrishnan S, Miles KM, Ellis L, Sotomayor P, et al. Class I histone deacetylase inhibitor entinostat suppresses regulatory T cells and enhances immunotherapies in renal and prostate cancer models. Ling MT, editor. PLoS One [Internet]. Public Library of Science; 2012 Jan [cited 2019 Feb 9];7(1):e30815. Available from: http://www.ncbi.nlm.nih.gov/pubmed/22303460

32. Tomita Y, Lee M-J, Lee S, Tomita S, Chumsri S, Cruickshank S, et al. The interplay of epigenetic therapy and immunity in locally recurrent or metastatic estrogen receptor-positive breast cancer: Correlative analysis of ENCORE 301, a randomized, placebo-controlled phase II trial of exemestane with or without

entinostat. Oncoimmunology. 2016 Nov;5(11):e1219008.

33. Denkert C, von Minckwitz G, Darb-Esfahani S, Lederer B, Heppner BI, Weber KE, et al. Tumour-infiltrating lymphocytes and prognosis in different subtypes of breast cancer: a pooled analysis of 3771 patients treated with neoadjuvant therapy. Lancet Oncol. 2017 Dec;

34. Solinas C, Gombos A, Latifyan S, Piccart-Gebhart M, Kok M, Buisseret L. Targeting immune checkpoints in breast cancer: an update of early results. ESMO Open. 2017 Nov;2(5):e000255.

35. SABCS 2017: Combination of Pembrolizumab and Trastuzumab Shows Early Promise for Patients With Trastuzumab-Resistant Breast Cancer - The ASCO Post.

36. Stagg J, Loi S, Divisekera U, Ngiow SF, Duret H, Yagita H, et al. Anti-ErbB-2 mAb therapy requires type I and II interferons and synergizes with anti-PD-1 or anti-CD137 mAb therapy. Proc Natl Acad Sci U S A. National Academy of Sciences; 2011 Apr;108(17):7142–7.

37. Lutz ER, Wu AA, Bigelow E, Sharma R, Mo G, Soares K, et al. Immunotherapy Converts Nonimmunogenic Pancreatic Tumors into Immunogenic Foci of Immune Regulation. Cancer Immunol Res. 2014 Jul;2(7):616–31.

38. Weiss VL, Lee TH, Song H, Kouo TS, Black CM, Sgouros G, et al. Trafficking of High Avidity HER-2/neu-Specific T Cells into HER-2/neu-Expressing Tumors after Depletion of Effector/Memory-Like Regulatory T Cells. Kassiotis G, editor. PLoS One. Public Library of Science; 2012 Feb;7(2):e31962.

39. Reilly RT, Gottlieb MB, Ercolini AM, Machiels JP, Kane CE, Okoye FI, et al. HER-2/neu is a tumor rejection target in tolerized HER-2/neu transgenic mice. Cancer Res. 2000 Jul;60(13):3569–76.

40. Mace K, Mayhew E, Mihich E, Ehrke MJ, Lei RY, Weintraub D, et al. Alterations in murine host defense functions by adriamycin or liposome-encapsulated adriamycin. Cancer Res. American Association for Cancer Research; 1988 Jan;48(1):130–6.

41. Corbett TH, Roberts BJ, Leopold WR, Peckham JC, Wilkoff LJ, Griswold DP, et al. Induction and chemotherapeutic response of two transplantable ductal adenocarcinomas of the pancreas in C57BL/6 mice. Cancer Res [Internet]. American Association for Cancer Research; 1984 Feb 1 [cited 2018 Aug 2];44(2):717–26. Available from: http://www.ncbi.nlm.nih.gov/pubmed/6692374

42. Leao IC, Ganesan P, Armstrong TD, Jaffee EM. Effective depletion of regulatory T cells allows the recruitment of mesothelin-specific CD8 T cells to the antitumor immune response against a mesothelin-expressing mouse pancreatic adenocarcinoma. Clin Transl Sci [Internet]. Wiley-Blackwell; 2008 Dec [cited 2018 Aug 2];1(3):228–39. Available from: http://www.ncbi.nlm.nih.gov/pubmed/20357913

43. Ercolini AM, Machiels J-PH, Chen YC, Slansky JE, Giedlen M, Reilly RT, et al. Identification and characterization of the immunodominant rat HER-2/neu MHC class I epitope presented by spontaneous mammary tumors from HER-2/neu-transgenic mice. J Immunol. 2003 Apr;170(8):4273–80.

44. Soares KC, Foley K, Olino K, Leubner A, Mayo SC, Jain A, et al. A preclinical murine model of hepatic metastases. J Vis Exp. 2014 Sep;(91):51677.

45. Lee JW, Komar CA, Bengsch F, Graham K, Beatty GL. Genetically Engineered Mouse Models of Pancreatic Cancer: The KPC Model (*LSL-Kras* $^{G12D/+}$ *;LSL-Trp53* $^{R172H/+}$ *;Pdx-1-Cre*), Its Variants, and Their Application in Immuno-

oncology Drug Discovery. In: Current Protocols in Pharmacology. Hoboken, NJ, USA: John Wiley & Sons, Inc.; 2016. p. 14.39.1-14.39.20.

46. Foote JB, Kok M, Leatherman JM, Armstrong TD, Marcinkowski BC, Ojalvo LS, et al. A STING Agonist Given with OX40 Receptor and PD-L1 Modulators Primes Immunity and Reduces Tumor Growth in Tolerized Mice.

47. Mueller S, Engleitner T, Maresch R, Zukowska M, Lange S, Kaltenbacher T, et al. Evolutionary routes and KRAS dosage define pancreatic cancer phenotypes. Nature [Internet]. Nature Publishing Group; 2018 Jan 24 [cited 2018 Jul 19];554(7690):62–8. Available from: http://www.nature.com/doifinder/10.1038/nature25459

48. Hingorani SR, Wang L, Multani AS, Combs C, Deramaudt TB, Hruban RH, et al. Trp53R172H and KrasG12D cooperate to promote chromosomal instability and widely metastatic pancreatic ductal adenocarcinoma in mice. Cancer Cell [Internet]. Cell Press; 2005 May 1 [cited 2018 Jul 19];7(5):469–83. Available from: https://www.sciencedirect.com/science/article/pii/S1535610805001285?via%3Dihub

49. Pardoll DM. The blockade of immune checkpoints in cancer immunotherapy. Nat Rev Cancer. 2012 Mar;12(4):252–64.

50. Soares KC, Rucki AA, Wu AA, Olino K, Xiao Q, Chai Y, et al. PD-1/PD-L1 blockade together with vaccine therapy facilitates effector T-cell infiltration into pancreatic tumors. J Immunother [Internet]. NIH Public Access; 2015 Jan [cited 2018 Aug 2];38(1):1–11. Available from: http://www.ncbi.nlm.nih.gov/pubmed/25415283

51. Shakespear MR, Halili MA, Irvine KM, Fairlie DP, Sweet MJ. Histone deacetylases as regulators of inflammation and immunity. Trends Immunol. 2011 Jul;32(7):335–43.

52. Klampfer L, Huang J, Swaby L-A, Augenlicht L. Requirement of Histone Deacetylase Activity for Signaling by STAT1. J Biol Chem. 2004 Jul;279(29):30358–68.

53. Zhang Q, Zhao K, Shen Q, Han Y, Gu Y, Li X, et al. Tet2 is required to resolve inflammation by recruiting Hdac2 to specifically repress IL-6. Nature. 2015 Sep;525(7569):389–93.

54. Pan W, Zhu S, Qu K, Meeth K, Cheng J, He K, et al. The DNA Methylcytosine Dioxygenase Tet2 Sustains Immunosuppressive Function of Tumor-Infiltrating Myeloid Cells to Promote Melanoma Progression. Immunity. 2017 Aug;47(2):284–297.e5.

55. Ritchie ME, Phipson B, Wu D, Hu Y, Law CW, Shi W, et al. limma powers differential expression analyses for RNA-sequencing and microarray studies. Nucleic Acids Res. 2015 Apr;43(7):e47–e47.

56. Luo W, Friedman MS, Shedden K, Hankenson KD, Woolf PJ. GAGE: generally applicable gene set enrichment for pathway analysis. BMC Bioinformatics. 2009 May;10(1):161.

57. Luo W, Brouwer C. Pathview: an R/Bioconductor package for pathway-based data integration and visualization. Bioinformatics. 2013 Jul;29(14):1830–1.

58. Garon EB, Rizvi NA, Hui R, Leighl N, Balmanoukian AS, Eder JP, et al. Pembrolizumab for the Treatment of Non–Small-Cell Lung Cancer. N Engl J Med. Massachusetts Medical Society; 2015 May;372(21):2018–28.

59. Thompson RH, Kuntz SM, Leibovich BC, Dong H, Lohse CM, Webster WS, et al. Tumor B7-H1 Is Associated with Poor Prognosis in Renal Cell Carcinoma Patients with Long-term Follow-up. Cancer Res. 2006 Apr;66(7):3381–5.

60. Slamon DJ, Leyland-Jones B, Shak S, Fuchs H, Paton V, Bajamonde A, et al. Use of chemotherapy plus a monoclonal antibody against HER2 for metastatic breast cancer that overexpresses HER2. N Engl J Med. 2001 Mar;344(11):783–92.

61. Falkenberg KJ, Johnstone RW. Histone deacetylases and their inhibitors in cancer, neurological diseases and immune disorders. Nat Rev Drug Discov. Nature Publishing Group; 2014 Sep;13(9):673–91.

62. Baitsch L, Legat A, Barba L, Fuertes Marraco SA, Rivals J-P, Baumgaertner P, et al. Extended Co-Expression of Inhibitory Receptors by Human CD8 T-Cells Depending on Differentiation, Antigen-Specificity and Anatomical Localization. Ashour HM, editor. PLoS One. Public Library of Science; 2012 Feb;7(2):e30852.

63. Blackburn SD, Shin H, Haining WN, Zou T, Workman CJ, Polley A, et al. Coregulation of CD8+ T cell exhaustion by multiple inhibitory receptors during chronic viral infection. Nat Immunol. 2009 Jan;10(1):29–37.

64. Shimizu K, Iyoda T, Okada M, Yamasaki S, Fujii S. Immune suppression and reversal of the suppressive tumor microenvironment. Int Immunol. Oxford University Press; 2018 Sep;30(10):445–55.

65. Pan P-Y, Ma G, Weber KJ, Ozao-Choy J, Wang G, Yin B, et al. Immune stimulatory receptor CD40 is required for T-cell suppression and T regulatory cell activation mediated by myeloid-derived suppressor cells in cancer. Cancer Res. 2010 Jan;70(1):99–108.

66. Horikawa N, Abiko K, Matsumura N, Hamanishi J, Baba T, Yamaguchi K, et al.

Expression of Vascular Endothelial Growth Factor in Ovarian Cancer Inhibits Tumor Immunity through the Accumulation of Myeloid-Derived Suppressor Cells. Clin Cancer Res. 2017 Jan;23(2):587–99.

67. Wei J, Besner GE. M1 to M2 macrophage polarization in heparin-binding epidermal growth factor-like growth factor therapy for necrotizing enterocolitis. J Surg Res. 2015 Jul;197(1):126–38.

68. Kaneda MM, Messer KS, Ralainirina N, Li H, Leem CJ, Gorjestani S, et al. Erratum: Corrigendum: PI3Kγ is a molecular switch that controls immune suppression. Nature. 2017 Feb;542(7639):124–124.

69. Wu T, Zhao Y, Wang H, Li Y, Shao L, Wang R, et al. mTOR masters monocytic myeloid-derived suppressor cells in mice with allografts or tumors. Sci Rep. 2016 Feb;6(1):20250.

70. Hardbower DM, Singh K, Asim M, Verriere TG, Olivares-Villagómez D, Barry DP, et al. EGFR regulates macrophage activation and function in bacterial infection. J Clin Invest. 2016 Sep;126(9):3296–312.

71. Kumar V, Donthireddy L, Marvel D, Condamine T, Wang F, Lavilla-Alonso S, et al. Cancer-Associated Fibroblasts Neutralize the Anti-tumor Effect of CSF1 Receptor Blockade by Inducing PMN-MDSC Infiltration of Tumors. Cancer Cell. Elsevier; 2017 Nov;32(5):654–668.e5.

72. Dodd KM, Yang J, Shen MH, Sampson JR, Tee AR. mTORC1 drives HIF-1α and VEGF-A signalling via multiple mechanisms involving 4E-BP1, S6K1 and STAT3. Oncogene. 2015 Apr;34(17):2239–50.

73. Wei D, Le X, Zheng L, Wang L, Frey JA, Gao AC, et al. Stat3 activation regulates the expression of vascular endothelial growth factor and human pancreatic cancer

angiogenesis and metastasis. Oncogene. Nature Publishing Group; 2003 Jan;22(3):319–29.

74. Niu G, Wright KL, Huang M, Song L, Haura E, Turkson J, et al. Constitutive Stat3 activity up-regulates VEGF expression and tumor angiogenesis. Oncogene. 2002 Mar;21(13):2000–8.

75. Wei L-H, Kuo M-L, Chen C-A, Chou C-H, Lai K-B, Lee C-N, et al. Interleukin-6 promotes cervical tumor growth by VEGF-dependent angiogenesis via a STAT3 pathway. Oncogene. 2003 Mar;22(10):1517–27.

76. Brocks D, Schmidt CR, Daskalakis M, Jang HS, Shah NM, Li D, et al. DNMT and HDAC inhibitors induce cryptic transcription start sites encoded in long terminal repeats. Nat Genet. 2017 Jun;49(7):1052–60.

77. Christmas BJ, Rafie CI, Hopkins AC, Scott BA, Ma HS, Cruz KA, et al. Entinostat converts immune-resistant breast and pancreatic cancers into checkpoint-responsive tumors by reprogramming tumor-infiltrating MDSCs. Cancer Immunol Res. 2018;6(12).

78. Gabrilovich DI. Myeloid-Derived Suppressor Cells. Cancer Immunol Res [Internet]. NIH Public Access; 2017 [cited 2019 Feb 17];5(1):3–8. Available from: http://www.ncbi.nlm.nih.gov/pubmed/28052991

79. Ko H-J, Kim Y-J. Signal transducer and activator of transcription proteins: regulators of myeloid-derived suppressor cell-mediated immunosuppression in cancer. Arch Pharm Res [Internet]. Pharmaceutical Society of Korea; 2016 Nov 29 [cited 2019 Feb 10];39(11):1597–608. Available from: http://link.springer.com/10.1007/s12272-016-0822-9

80. Liu F, Li X, Lu C, Bai A, Bielawski J, Bielawska A, et al. Ceramide activates

lysosomal cathepsin B and cathepsin D to attenuate autophagy and induces ER stress to suppress myeloid-derived suppressor cells. Oncotarget [Internet]. Impact Journals, LLC; 2016 Dec 20 [cited 2019 Feb 12];7(51):83907–25. Available from: http://www.ncbi.nlm.nih.gov/pubmed/27880732

81. Lu C, Redd PS, Lee JR, Savage N, Liu K. The expression profiles and regulation of PD-L1 in tumor-induced myeloid-derived suppressor cells. Oncoimmunology [Internet]. Taylor & Francis; 2016 [cited 2019 Feb 12];5(12):e1247135. Available from: http://www.ncbi.nlm.nih.gov/pubmed/28123883

82. Qu P, Wang L-Z, Lin PC. Mini-review Expansion and functions of myeloid-derived suppressor cells in the tumor microenvironment. Cancer Lett [Internet]. 2016 [cited 2019 Feb 14];380:253–6. Available from: http://dx.doi.org/10.1016/j.canlet.2015.10.022

C U R R I C U L U M V I T A E

Brian J. Christmas
Department of Oncology, Sidney Kimmel Comprehensive Cancer Center
The Johns Hopkins University School of Medicine
1650 Orleans Street, Cancer Research Building 1, Room 422
Baltimore, MD 21287
Home: 815-474-9697 | Work: 410-614-4772
Email: bchris18@jhmi.edu

Education

Ph.D. **2019** **Immunology**
Johns Hopkins School of Medicine Baltimore, MD
Dissertation: *Epigenetic reprogramming of myeloid-derived suppressor cells sensitizes breast and pancreatic cancers to immune checkpoint inhibition*
Advisor: Elizabeth M. Jaffee, M.D.

B.S. **2014** **Majors: Chemistry; Molecular Biology**
Southeast Missouri State University Cape Girardeau, MO

Research Experience

Johns Hopkins School of Medicine Baltimore, MD **August 2015 – Present**
Department of Oncology
Advisor: Elizabeth M. Jaffee, M.D.
Developing a treatment scheme using the histone deacetylase inhibitor entinostat to render intratumoral myeloid-derived suppressor cells dysfunctional and subsequently sensitize non-immunogenic tumors to immune checkpoint inhibition therapy

- Performed hemisplenectomy surgeries to model hepatic metastasis of pancreatic cancer
- Modeled and maintained combinatorial drug studies for mouse cohorts of 150+ animals, identifying the most effective treatment combinations and scheduling
- Evaluated changes in populations and function of tumor-infiltrating myeloid and T cells of treated animals using flow cytometry
- Performed *ex vivo* functional assays using isolated MDSCs, such as colorometric arginase activity assays and immunosuppression assays
- Optimized and performed ChIP analysis of drug-induced changes in transcription factor binding in *in vitro* cell lines
- ***Selected Technical Skills:*** mouse modeling, mouse dosing (i.p., s.c., i.v., gavage), mouse surgery, flow cytometry, immune cell isolations and co-cultures, Western blot, ChIP, and qPCR

Southeast Missouri State University Cape Girardeau, MO **August 2011 – May 2014**
Department of Biology
Advisor: Dr. James Champine, Ph.D.

- Cultured E. coli, extracted DNA from E. coli, performed DNA replication, and gel electrophoresis analysis in the process of microbial source tracking
- Participated in independent research on the enzyme dihydrofolate reductase purified from *E. coli* to test the effects of various chemicals as enzyme inhibitors with applications in the field of chemotherapeutics
- ***Selected Technical Skills:*** aseptic technique to grow isolated *E. coli* colonies, IMViC tests to identify pure *E. coli* colonies, and performing enzyme kinetics assays using spectrophotometry

University of Nebraska-Lincoln Lincoln, NE **Summer 2013**
Nebraska Center for Virology
Advisor: Dr. Qingsheng Li, Ph.D.

- Completed an independent research project on the quantification of virus target cells in the rectal, foreskin, and cervicovaginal mucosa of SIV uninfected and early-infected macaques
- ***Selected Technical Skills*:** tissue processing, embedding, and cutting, tissue staining via immunohistochemistry, and tissue quantification techniques via the Aperio ImageScope software

Indian Association for the Cultivation of Science Kolkata, India **Summer 2012**
Department of Organic Chemistry
Advisor/Supervisor: Dr. Bjorn Olesen, Ph.D. / Dr. Brindaban Ranu, Ph.D.

- Participated in green chemistry research, focusing on the use of a ruthenium catalyst to oxidize various alcohols to aldehydes and carboxylic acids
- ***Selected Technical Skills*:** extraction, washing, thin-layer chromatography, and column chromatography

Publications and Presentations

Christmas BJ, Rafie CI, Jaffee EM, Roussos Torres ET. STAT3 mediates epigenetic regulation of MDSCs in tumors. To be presented at: *American Association for Cancer Research: Annual Meeting 2019*. Abstract #1529 (2019).

Ma HS, Poudel B, Roussos Torres ET, Sidhom JW, Robinson TM, **Christmas BJ**, Scott BA, Cruz KA, Woolman S, Wall VZ, Armstrong TD, Jaffee EM. A CD40 agonist and PD-1 antagonist antibody reprogram the microenvironment of non-immunogenic tumors to allow T cell-mediated anticancer activity. *Cancer Immunolo. Res.* doi: 10.1158/2326-6066.CIR-18-0061 (2019).

Christmas BJ, Rafie CI, Hopkins AC, Scott BA, Ma HS, Cruz KA, Woolman S, Armstrong TD, Connolly RM, Azad NA, Jaffee EM, Roussos Torres ET. Entinostat converts immune-resistant breast and pancreatic cancers into checkpoint-responsive tumors by reprogramming tumor-infiltrating MDSCs. *Cancer Immunol. Res.* 6(12):1561-1577 (2018).

Christmas BJ, Scott BS, Armstrong TD, Azad NA, Jaffee EM. Epigenetic Modulation of the Tumor Microenvironment Enhances Immune Checkpoint Efficacy in a Murine Model of Pancreatic Cancer. Presented at: *American Association for Cancer Research: Annual Meeting 2018*. Abstract #1746 (2018).

Christmas BJ, Scott BS, Armstrong TD, Azad NA, Jaffee EM. Epigenetic Modulation of the Tumor Microenvironment Enhances Vaccine Induced T cell Responses in a Murine Model of Pancreatic Cancer. Presented at: *American Association for Cancer Research: Annual Meeting 2017*. Abstract #1686 (2017).

Society Memberships

- American Association for Cancer Research, 2017-2019

Additional Skills

- Reviewed manuscript submitted for publication to Journal of Clinical Immunology
- Assisted writing and preparing the successfully funded grant proposals "Combinatorial Therapy using Epigenetic Modulatory Drugs and Immunotherapy in Murine Models of Pancreatic Ductal Adenocarcinoma" (Commonwealth Foundation for Cancer Research, an internal grant from the Kimmel Cancer Center) and "A phase II study of HDAC inhibition to sensitize to immunotherapy in advanced pancreatic cancer" (The Lustgarten Foundations's Principal Investigator's Award Program)

References

Elizabeth M. Jaffee, M.D., FAACR
The Dana and Albert "Cubby" Broccoli Professor of Oncology
Deputy Director, Sidney Kimmel Comprehensive Cancer Center at Johns Hopkins
Co-Director of the Gastrointestinal Cancers Program
1650 Orleans Street, CRB1 Room 4M07
Baltimore, MD 21287
Email: ejaffee@jhmi.edu
Phone: 410-955-2957

Evanthia Roussos Torres, MD/PhD
Assistant Professor
Breast and Ovarian Cancer Program & Cancer Immunology
Sidney Kimmel Comprehensive Cancer Center at Johns Hopkins
1650 Orleans Street, CRB1 Room 487
Baltimore, MD 21287
Email: ertorres@jhu.edu
Phone: (410) 614-1058